Department of Precision and Microsystems Engineering

Overactuation for Active Damping in Compliant Positioning Stage using Piezoelectric Transducers

Aditya Manoj Natu

Report no : 2023.064
Coach : M. B. Kaczmarek
Professor : Dr. S.H. HosseinNia Kani
Specialisation : Mechatronic System Design
Type of report : Master Thesis
Date : 21 August 2023

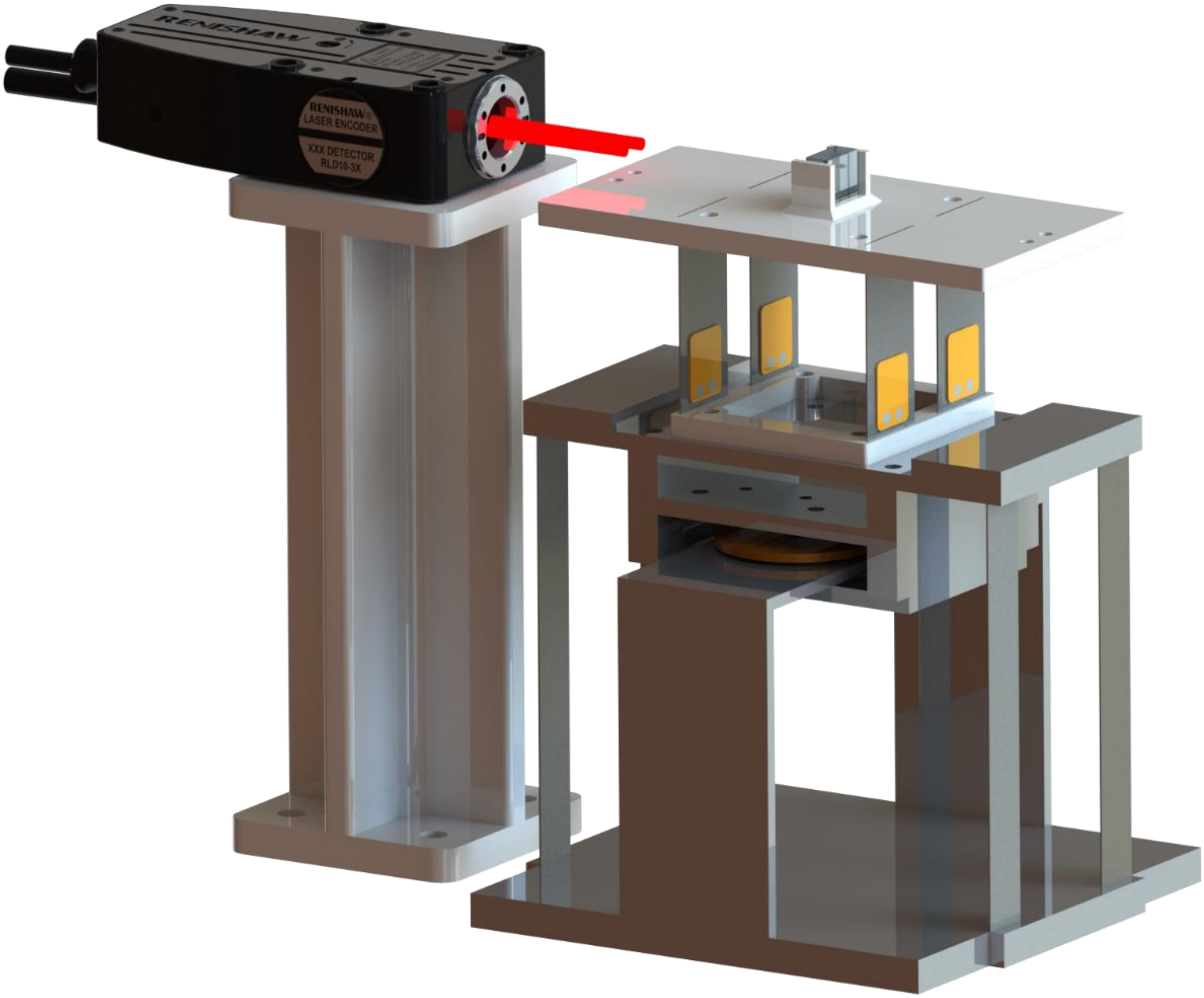

Delft University of Technology

Challenge the future

OVERACTUATION FOR ACTIVE DAMPING IN COMPLIANT POSITIONING STAGE USING PIEZOELECTRIC TRANSDUCERS

Master Thesis

Submitted to the Delft University of Technology in partial
fulfillment of the requirements for the degree of

Master of Science in Mechanical Engineering

By

ADITYA MANOJ NATU
(5482002)

Thesis Committee:	Dr. Hassan Hossein Nia Kani,	Supervisor
	Ir. Marcin Brunon Kaczmarek,	Daily Supervisor
	Dr. Matin Jafarian	
	Dr. Amin Sharifi Kolarijani	

August 2023

Abstract

Integrating compliant mechanisms into high-precision motion systems has facilitated the development of lightweight and frictionless designs. However, these systems often face challenges related to low-frequency parasitic resonance modes and limited structural damping, leading to compromised position accuracy and restricted control bandwidth. While notch filters are conventionally used to suppress these parasitic resonance peaks and enable higher control bandwidths, undesired effects persist in closed-loop disturbance rejection performance. To address this limitation, researchers have explored the concept of overactuation, employing a greater number of actuators than the number of rigid body modes to be controlled. This approach allows for additional closed-loop feedback interconnections, offering increased freedom to enhance performance. This research presents a novel overactuation-based solution where: (1) the use of additional actuators enables the implementation of active damping control to improve closed-loop disturbance rejection performance and (2) the integration of multiple distributed piezoelectric bender actuator-sensor pairs in a collocated configuration enhances damping performance. A mathematical framework is formulated to demonstrate the benefits, and an experimental setup is constructed to validate the numerical findings and serve as a proof of concept. The proposed solution effectively suppresses the parasitic resonance mode, enhances disturbance rejection on the end-effector, and enables higher control bandwidth in the positioning system.

Acknowledgements

With the completion of this thesis, I conclude my tenure as a master's student pursuing an MSc in Mechanical Engineering (High-Tech Engineering) at the esteemed TU Delft. Throughout an entire year dedicated to this project, I am grateful for the invaluable support and guidance provided by the following individuals:

First and foremost, I extend my heartfelt gratitude to my supervisor, Hassan, for introducing me to the fascinating domain of mechatronics, which ignited my passion for research in this field. Throughout the year, his unwavering belief in my capabilities, along with his invaluable expertise and experience in this area, has been instrumental in shaping the trajectory of my research. His guidance on simplifying complex topics and presenting my work with scientific rigor has been pivotal in ensuring the quality and depth of my research. Despite his busy schedule, he consistently made time for personal meetings, where I could openly discuss any aspect of my work. I consider myself incredibly fortunate and honored to have had him as my supervisor, as his mentorship provided me with a sense of calm and confidence during challenging times. Looking ahead, I am excited to continue my academic journey here at TU Delft, where I will have the privilege of continuing to work with him beyond my Masters.

I extend a big and heartfelt thanks to my daily supervisor, Marcin, who was a constant presence at each and every step of my project. His extensive knowledge and deep comprehension of the topics were invaluable in providing me with in-depth clarity on numerous occasions. I always enjoyed engaging in discussions with him, exploring various ideas and challenging aspects of my research. His keen eye for detail always pointed me in the right direction, guiding me through the complexities of my work. He played a crucial role in shaping my research topic and fostering a sense of curiosity, enhancing my critical thinking and analytical skills. During the experimental work in the lab, his consistent presence and assistance were instrumental, and he provided valuable insights whenever obstacles arose. I consider myself truly fortunate to have had Marcin as my daily supervisor, and I am certain that this project would not have been the same without his unwavering support and expertise.

I wish to express my sincere thanks to Bram for offering me access to his software, which significantly facilitated the modeling and simulation of the system for my research. His kind support in addressing any queries related to the codes and implementation proved to be extremely valuable, enabling a seamless workflow throughout the project.

I wholeheartedly express my appreciation to my fellow colleagues in the Mechatronics Lab, Francesco, Castor, and Shiyu. Throughout the year, we collaborated closely, working together to construct our experimental setups, engaging in stimulating discussions on various research

topics, troubleshooting challenges, and sharing much-needed coffee breaks. Their continuous presence in the lab served as a constant source of motivation, and I am truly grateful for the camaraderie and support that enriched our collective journey.

I extend my thanks to the Lab support team for their invaluable assistance in procuring our components and arranging the necessary equipment in the lab. Their help was crucial in enabling the smooth construction and operation of my experimental setup.

Finally, I would like to express my heartfelt gratitude to my family and close friends, both in India and here in the Netherlands, for their unconditional support and love throughout this journey. Their encouragement and presence have been invaluable, providing me with the strength and motivation to pursue my studies and research.

Aditya Natu

Delft, August 2023

Contents

1 | Introduction

1.1 Background

The escalating demands for elevated throughput and precision in positioning, spurred by rapid technological progress in the field of nano-science, have resulted in the widespread adoption of positioning systems featuring flexure-based mechanisms within the high-tech industry. These systems are extensively employed in various applications, including wafer alignments [1], scanning probe microscopes [2, 3], micromanipulators [4–7], nanomanufacturing [8], metrology [9, 10], and MEMS devices [11], among other applications. Figure 1.1 displays a monolithic compliant precision motion stage featuring 3 degrees of freedom (DoF), specifically designed for high-throughput probe-based nanofabrication [12]. In addition, Fig. 1.2 presents a flexure-guided X-stage nanopositioner intended for scanning and metrology processes [13].

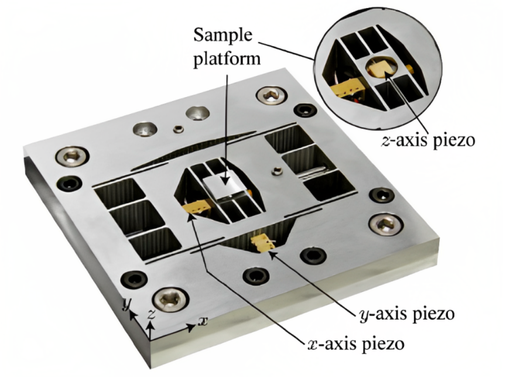

Figure 1.1: 3 DoF Nanopositioner [12]

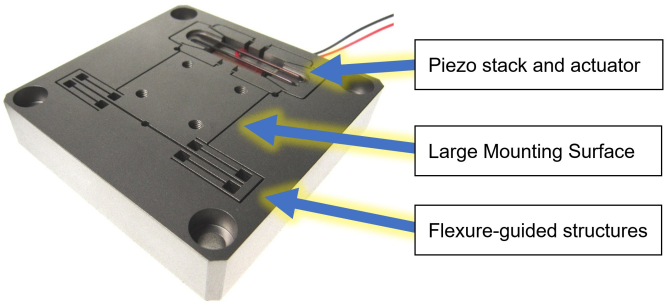

Figure 1.2: 1 DoF Nanopositioner [13]

The integration of compliant flexures facilitates achieving the required range of motion in these systems, and they also provide several advantages [14]. Firstly, they provide high repeatability as they lack friction, hysteresis, or backlash. Secondly, they are generally more cost-effective to manufacture due to their reduced number of components compared to conventional joints, often resulting in monolithic structures. Manufacturing processes like laser cutting, additive manufacturing, and Wire-EDM [15] can be easily employed in their production. This, in turn, leads to minimal friction wear and significantly reduced maintenance requirements compared to traditional joints. Moreover, the absence of lubrication needs makes them less susceptible to issues related to particle contamination, making them well-suited for use in vacuum environments [16].

1.2 Problem Statement and Motivation

The advantages associated with compliant mechanisms, as mentioned earlier, highlight their suitability for utilization in high-precision motion systems. However, it is important to recognize that every engineering solution comes with its own set of costs, which requires a critical perspective to evaluate the trade-offs involved. The constant demand to enhance payload capacity by achieving high support stiffness while minimizing structural weight poses a challenge as it results in a decrease in the inherent structural damping of the system. Consequently, such lightweight and flexible systems exhibit low damping characteristics, leading to lightly damped higher-order parasitic vibration modes at relatively low frequencies [17]. These unwanted vibrations adversely affect motion performance and accuracy [18]. Furthermore, the presence of a small structural damping ratio results in a significant phase drop, yielding a low-gain margin for the vibrational dynamics [19]. Additionally, the complex geometries of these systems often give rise to non-collocated dynamics, displaying non-minimum phase behavior, which restricts the control bandwidth to a small fraction of the parasitic resonance frequency [20, 21]. Consequently, incorporating compliant flexures in motion stages becomes challenging, necessitating the development of cutting-edge engineering solutions to enhance the motion performance of high-precision compliant motion stages.

To illustrate the aforementioned issues, an example of an arbitrary dual-stage positioning system with compliant flexures connecting the two stages is depicted in Fig.1.3. The non-collocated system frequency response, $F_{\text{act}} \mapsto x_2$, is shown in Fig.1.4. The second resonance peak in the frequency response is attributed to the resonance mode of the connecting parallel flexures, which exhibit low damping characteristics. If excited, this peak leads to undesirable vibration of the end-effector, affecting positional accuracy. Additionally, the phase drop beyond $-180°$ results in non-minimum phase behavior, restricting the control bandwidth of the positioning system.

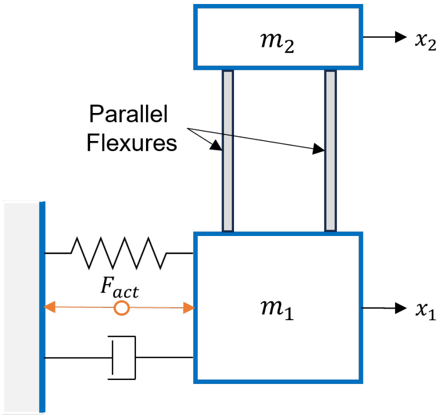

Figure 1.3: Illustration of Dual-Stage Compliant Positioning System

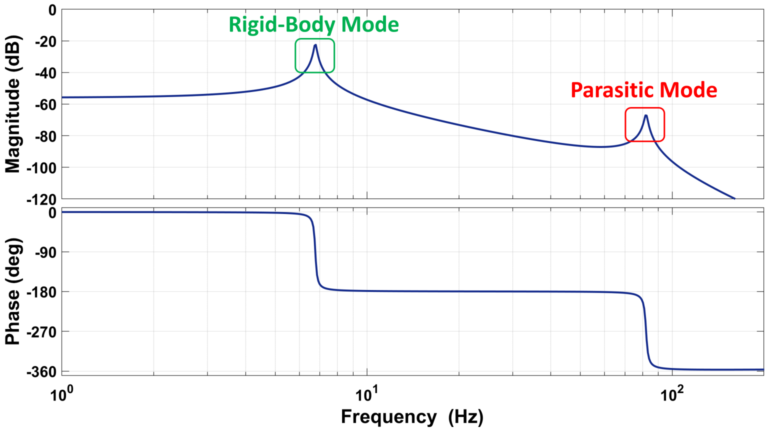

Figure 1.4: Non-Collocated Frequency Response $F_{\text{act}} \mapsto x_2$

1.3 State-of-the-Art Strategies

The preceding section introduced the problems of incorporating compliant flexures in motion stages and the motivation to solve these issues. The problem can be envisioned by the parasitic resonance peaks occurring at relatively low frequencies in the system's frequency response. This section will, thus, present and explore briefly the strategies employed so far in the extensive literature.

1.3.1 Compliant Motion Stage Design

A general engineering approach is to design and optimize the systems with high-frequency flexible modes, such that they appear beyond the excitation band of the known and measurable disturbances, thus rendering a high structural bandwidth. This can essentially be achieved by increasing the structural stiffness and decreasing the moving mass of the flexural structure [8]. However, simply scaling up the flexure dimensions with higher stiffness leads to workspace dimensions and an increase of parasitic motions (see Fig.1.5), respectively, due to undesired stress distribution and nonlinear elastokinematic effects [22]. Thus, for high-bandwidth and high-accuracy nanopositioners, the high-bandwidth structures need to be carefully constructed to reduce parasitic motion.

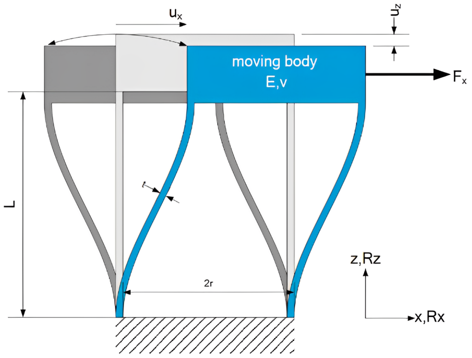

Figure 1.5: Rigid-body Translation with Parasitic Motion in a Parallel Kinematic Mechanism [23]

Micro-/nanopositioning stages have frequently utilized parallel kinematic mechanisms (PKMs) due to their ability to achieve uniform performance within the workspace, unlike serial kinematic systems. Properly designed PKMs offer enhanced positioning accuracy and nearly complete decoupling of the actuation effect, resulting in improved motion range and resolution. These parallel kinematic designs are often optimized for a wide range of motion, decoupling, sensitivity, and position accuracy. However, high bandwidth remains a persistent challenge for such systems [24–30].

1.3.2 Feedback and Feedforward Control of Motion Systems

Under the limitation of expansion in the control bandwidth, a control framework, as presented in Fig.1.6, employing feedback (K) and feedforward (F) compensators is often a practical strategy utilized. A typical feedback controller for a motion system often employs a PID controller, exhibiting robust stability margins due to the phase lead/lag filter within it [2, 32, 33]. If the stability is endangered by resonances, second-order filters, called notches, are

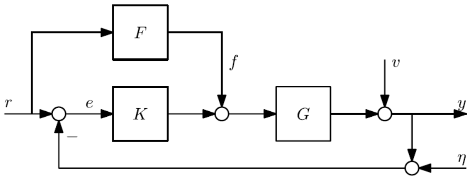

Figure 1.6: General Motion Control Architecture [31]

utilized to suppress the resonance peaks of low-mid frequency range parasitic flexible modes in the system [34–36]. Feedforward compensators often involve inversion-based filters to counter disturbances induced by known reference inputs to the system [2, 37, 38]. Although these techniques can yield favorable outcomes for systems with accurate models and known references, they lack robustness in the face of system parameter uncertainties and external disturbances.

1.3.3 Damping Strategies for Flexure-like Systems

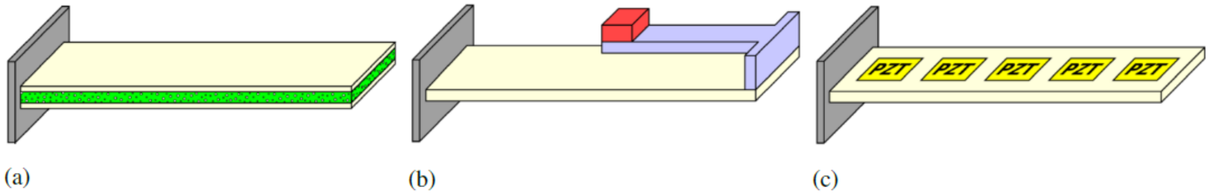

Figure 1.7: Schematic overview of different damping methods (a) Constrained Layer Damping; (b) Tuned Mass Damper; (c) Active Damping [16]

Damping in mechanical systems involves dissipating vibrational energy to reduce resonance peaks in the frequency response function. Passive and active methods are used for damping mechanical vibrations in thin beams/flexures. Passive methods include constrained layer damping (CLD) and tuned mass damper (TMD), as illustrated in Fig.1.7(a) and (b), respectively. CLD uses a viscoelastic material sandwiched between stiff layers to convert kinetic energy into heat, acting as a vibration damper. TMD consists of a mass tuned to match the resonance frequency of the host structure, reducing its maximum vibration amplitude. Passive damping systems require no external energy source or sensors, dissipating energy inside the system proportionally to the weight. They are effective for high-frequency vibration and single resonance frequency damping but unsuitable for broad-range frequency suppression and add considerable weight.

Active damping, shown in Fig.1.7(c), requires sensors, control, and an external energy source. It dissipates energy outside the system and can be switched on as needed. Active damping is effective over a wide frequency range, offering higher performance, lower cost, and less mass constraints. For high-tech systems requiring various vibration mode suppression and large bandwidth, active vibration control (AVC) is promising. AVC utilizes digital control, making tuning simple. By strategically positioning sensor-actuator pairs and adjusting controller gains, it modifies the structure's mode shapes and effectively reduces undesired magnitudes.

1.3.4 Active Damping Control of Motion Systems with Single-Actuator

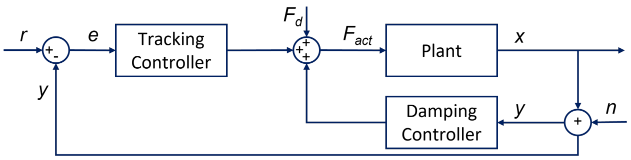

Figure 1.8: Generalized Dual-Loop Control Architecture for Tracking and Damping Control of Motion Systems with Single-Actuator

Damping controllers in feedback loops are explored to address the damping of parasitic resonance modes and enhance robustness to uncertainties within systems. Among these controllers, widely used fixed-structure low-order schemes include integral resonant control (IRC) [39,40], integral force feedback (IFF) [41,42], positive position feedback (PPF) [43,44], positive velocity and position feedback (PVPF) [45], and positive acceleration, velocity, and position feedback (PAVPF) [46–48]. The IFF scheme, while advantageous for its utilization of a low-noise piezoelectric force transducer and high bandwidth capabilities, is limited by its requirement for a force transducer, restricting its widespread use. PVPF and PAVPF controllers have shown effective damping when appropriately tuned, but their sensitivity to noise, especially in systems equipped with position sensors, poses challenges due to numerical differentiation. The PPF controller has gained extensive application due to its ability to strategically position system poles for effective damping and its simplicity, making it suitable for suppressing multiple modes [49, 50]. It exhibits increased robustness with higher controller damping values and second-order high-frequency roll-off characteristics [51]. Besides positioning systems, the PPF controller is applied in vibration control of thin beam and plate-like structures [52, 53]. Frequently, it is combined with collocated piezoelectric bender transducers to provide active damping. The collocated configuration ensures pole-zero interlacing and a phase range between 0-180° [54], contributing to an unconditionally stable system and effective operation of the PPF controller in this setup.

1.3.5 Overactuation in Motion Systems

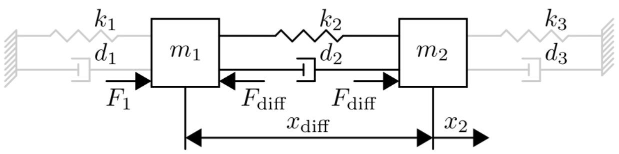

Figure 1.9: Illustration of overactuation with additional actuator force F_{diff} based on senor measurement x_{diff} [55]

In conventional single-axis positioning systems, a Single Input, Single Output (SISO) configuration is typically employed, utilizing a single actuator and sensor to control. Ideally, the actuator is positioned to facilitate rigid body motion while avoiding the excitation of unwanted parasitic resonances. However, when active damping is required, the same actuator is used to suppress undesired resonances and external disturbances through the feedback loop.

This creates a conflict, as positioning the actuator for effective damping of undesired modes may compromise optimal motion-tracking performance, where positioning aims to minimize the excitation of these parasitic modes. Thus, a trade-off is often necessary to achieve satisfactory tracking and damping performance. One method is to increase mechanical stiffness by adding mass to the mobile components, but it is considered undesirable due to drawbacks such as requiring higher actuation forces, leading to greater resistive heating. To address this limitation, researchers have explored the concept of overactuation, involving the use of more actuators than the number of rigid body modes to be controlled [56]. This technique establishes additional closed-loop feedback interconnections, offering increased freedom to enhance performance [55, 57], allowing for improved control over system modes while maintaining a favorable balance between the tracking and damping feedback paths [58–60].

1.4 Research Objectives

The preceding section provided a brief overview of the advantages of incorporating additional actuators in motion systems to achieve individual control of the rigid body and parasitic modes through separate feedback loops. However, integrating multiple conventional actuators requires a thorough system architecture redesign, contributing to increased system weight. Additionally, it was highlighted that active damping of parasitic resonance in flexures can be achieved by integrating distributed piezoelectric actuators and sensors onto their surface. These compact, lightweight actuator-sensor pairs have minimal impact on system dynamics, making them promising for use in high-precision motion systems. This research gap forms the foundation of the scientific contribution made in this thesis. Hence, the general research question is formulated as follows:

How can overactuation using distributed collocated piezoelectric transducers in smart flexures lead to enhanced damping and motion performance in high-precision compliant positioning stages?

To answer this research question, this thesis proposes a novel overactuation-based solution to overcome these limitations through active control of flexible dynamical behavior, with the main contributions as follows:

1. The use of additional actuators enables the implementation of active damping control to improve closed-loop disturbance rejection performance.
2. The integration of multiple distributed piezoelectric bender actuator-sensor pairs in a collocated configuration enhances damping performance.

To demonstrate the contributions of this work, the following objectives are formulated as follows:

1. Develop a numerical model of a dual-stage compliant motion system integrating distributed piezoelectric actuators and sensors.
    - Design system using flexure design calculation guidelines.
    - Numerically model the system in SPACAR and obtain the frequency response characteristics of the system.

  - Numerically implement the closed-loop motion and damping control and simulate system performance in MATLAB.
  - Develop a mathematical framework to demonstrate the work contributions.

2. Build an experimental setup of the modeled motion system with distributed piezoelectric actuators and sensors.
   - Integrate all actuators and sensors in the setup and develop the LabVIEW programs to enable experimental implementation.
   - Identify the system, design, and tune motion and damping controllers.
   - Implement real-time digital closed-loop control and obtain measurements for all test cases.
   - Demonstrate the contributions experimentally and compare them with the numerical findings.

1.5 Thesis Outline

The present chapter provides a concise overview of compliant positioning systems within the high-tech industry. It encompasses their background, associated challenges, and state-of-the-art strategies and identifies a research gap. Furthermore, the chapter clearly outlines the research objectives and the scientific contributions that have been fulfilled in this thesis. The subsequent thesis report is structured as follows:

- Chapter 2 provides a comprehensive literature overview of active vibration control. This review encompasses various aspects, including the dynamics of flexible structures, the operational principles of piezoelectric transducers, distributed and overactuation strategies utilized for active damping, as well as an exploration of different control architectures and controller algorithms conventionally employed in this field. The chapter presents a concise summary of the literature study conducted as an integral part of this thesis.
- Chapter 3 presents the main contribution of this research, thereby addressing the identified research gap. This chapter is formulated in a scientific journal paper format to be self-contained.
- Chapter 4 presents additional insights and in-depth discussions concerning the experimental results obtained throughout this research.
- Chapter 5 succinctly summarizes the outcomes of the research and provides recommendations for future studies related to this work.
- Finally, extensive appendices are included to provide supplementary information explaining the process undertaken to achieve the objectives of the study. Additionally, these appendices serve to offer future students the opportunity to replicate, continue, and expand upon this work.

2 | Literature Preliminaries

This chapter provides a comprehensive overview of the fundamental concepts and preliminary knowledge from the literature essential for comprehending the research presented in this thesis. It commences with a discussion of active vibration control techniques applied to flexible structures and also examines various control architectures and algorithms that have been employed in the existing literature. Additionally, this chapter offers insight into the functioning of piezoelectric transducers and their observed behavior in practical applications. Lastly, it demonstrates the concepts of distributed and overactuation through examples from the literature, elucidating the principles underlying these approaches.

2.1 Active Vibration Control

The primary objective of Active Vibration Control (AVC) is to attenuate (dampen) the magnitude of the resonance peaks observed in the system's frequency resonance (dynamic amplification), as visualized in Fig.2.1. This is effectively carried out by a feedback controller in a closed-loop system by increasing the negative real part of the system poles while maintaining the natural frequencies essentially unchanged, illustrated in Fig.2.2 [54].

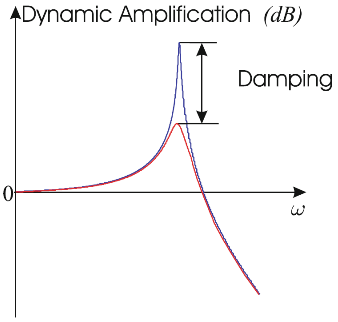

Figure 2.1: Reduction of Peak Height due to Dampening [54]

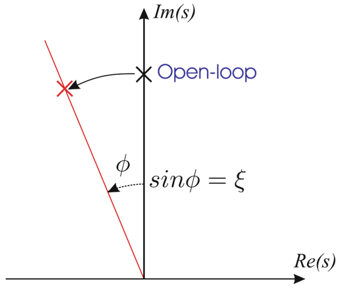

Figure 2.2: Damped System Poles [54]

2.1.1 Dynamics of Flexible Structures

Flexible mechanical structures are essentially distributed parameter systems and therefore possess an infinite number of flexible modes [54]. In order to fully describe their dynamic response, it would require infinite degrees of freedom, which can be practically and computationally challenging. Thus, usually, these flexible structures are modeled as lumped parameter systems with finite degrees of freedom to approximate their vibration characteristics. This can be achieved using several well-formulated methods such as finite-element modeling, modal analysis, or system identification [61]. However, it's imperative to ensure that all pertinent system modes (non-negligible elastic modes with low damping ratios) are taken into account during such an approximation such that the model can be effectively used to visualize system behavior and to design efficient controllers to dampen the system [62]. Typically, modal coordinates are preferred since they simplify the dynamics into a linear combination of the system's vibration modes. These dynamics then can be expressed in the frequency domain by applying the Fourier transform. Mathematically, the generalized transfer function from the force input to the displacement output of the lumped parameter system G can be expressed in the frequency domain as the sum of M modes by:

$$G = \sum_{i=1}^{M} \frac{k_i}{s^2 + 2\zeta_i\omega_i s + \omega_i^2} + R \tag{2.1}$$

where ζ_i and ω_i corresponds to the damping ratio and eigenfrequency, and k_i represents a constant related to the modal displacement of the i^{th} flexible mode, and s is the Laplace variable. Moreover, R is a feedthrough term to account for the truncated flexible modes, also known as the residual modes [54]. This term is essentially a constant static gain for all frequencies and is essential to incorporate to model the system well, especially when using feedback controllers in a collocated sensor-actuator configuration [61, 63].

By effectively treating a continuous flexible structure as a cluster of distinct mass-spring-damper systems, active damping control strategies can be developed to dampen these individual modes. In the time domain, the effects of damping can be visualized as faster decay of the oscillation amplitude, while in the frequency domain, active damping causes the peaks of the system poles to decrease in magnitude, as illustrated in Fig.2.3.

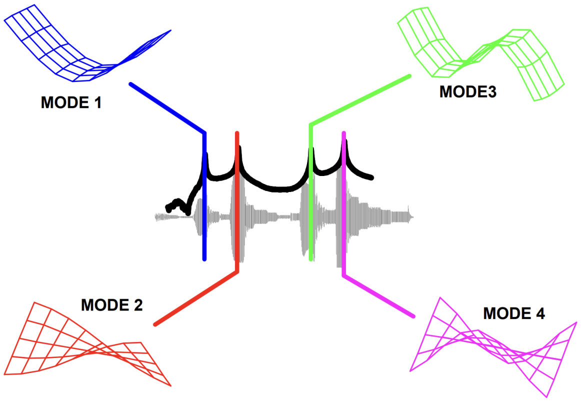

Figure 2.3: Time and frequency domain visualization of structural modes [64]

2.1.2 Collocated System Configuration

A collocated system constitutes a system with the sensor and actuator attached to the the same degree of freedom, and the sensor and actuator are dual [54]. In practice, this is realized by having the sensor-actuator pair at the same location. The term "duality" in this context refers to the energy exchange between the host structure and the control system as represented by the product of the sensor signal and the actuator signal. A force actuator and displacement sensor, or a torque actuator and rotational sensor, are two such examples of dual sensors and actuators. In a collocated system, the open-loop frequency response function (FRF) from the actuator to the sensor attached to the DoF k, the transfer function is represented as,

$$G_{kk}(\omega) = \sum_{i=1}^{m} \frac{\phi_i^2(k)}{\mu_i\left(\omega_i^2 - \omega^2\right)} + R_{kk} \tag{2.2}$$

where, ω_i is the resonance frequency of the i^{th} mode of the structure, ϕ_i is the mode participation factor and is dependent on the position of the actuator and sensor, and R_{kk} is the residue due to modal truncation and is positive (squared term) [54].

An interesting characteristic of a perfectly collocated system is that their phase always lies between 0 and -180 degrees, and their poles and zeros interlace (pole-zero pairing), as illustrated in Fig.2.4. As long as there are no additional controller, actuator, and filter dynamics present, this property makes them unconditionally stable even in the presence of out-of-bandwidth dynamics [54]. For non-collocated systems (systems where sensors and actuators are not attached to the same DoF), the poles and zeros are no longer present in pairs, known as pole-zero flipping. This results in a 360° phase uncertainty, which implies that the system is not robustly stable. Non-collocated plants generally exhibit better high-frequency roll-off characteristics because there are weaker mechanical and electrical feedthrough couplings between non-collocated transducers [65].

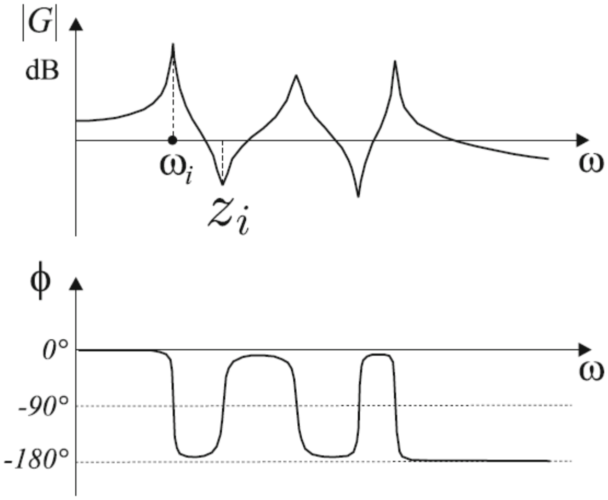

Figure 2.4: Frequency response of a lightly damped collocated system [54]

Practically, perfect collocation is quite difficult to attain until there is a self-sensing actuator employed [66]. Thus, typically, the actuator and sensor are typically positioned very closely together to create configurations that are nearly collocated. Both the actuator and the sensor will exhibit similar stability and robustness characteristics as long as their modal displacements have the same sign and equivalent magnitudes.

2.1.3 Spillover

In general, spillover can be described as the influence of modes outside the controller's bandwidth, as illustrated in Fig.2.5, on the closed-loop system. The spillover can be categorized into two types, namely *observation spillover* and *control spillover*.

- *Observation Spillover* occurs when sensor outputs are contaminated by the measured response of residual modes.
- *Control Spillover* occurs when residual modes are excited by the feedback control.

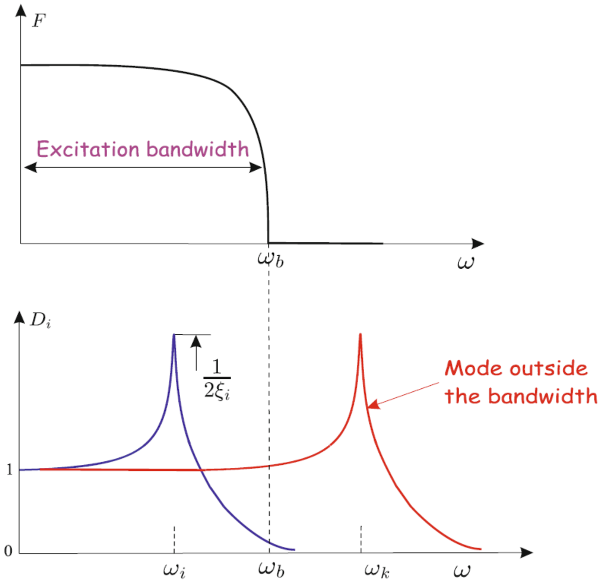

Figure 2.5: In-bandwidth and out-of-bandwidth modes [54]

In the absence of observation spillover, excitation of the residual modes may deteriorate the system response, but it cannot destabilize the system. Instead, even a slight shift in the system's poles can cause instability when both control and observation overflow are present. Assuming that the controller itself is stable, modal controllers have the potential to cause instabilities unless observation spillover can be prevented [67, 68]. Thus, this necessitates the need of incorporating the residual modes in the system's mathematical model via a feedthrough term.

The spillover can be minimized by placing the sensor-actuator pairs at the nodes of the residual modes, which can be realistically challenging due to the large number of residual modes and their corresponding convoluted shapes. An effective way of reducing spillover is to use suitable controllers with desirable frequency responses, like low-pass characteristics, to concentrate the control energy and sensing onto the relevant modes. However, it should be noted that certain damping controller topologies with low-pass or high-pass behavior can cause spillover even for non-residual modes.

2.1.4 Control Architecture

The active vibration control of flexible structures usually employs several actuators and sensors to dampen the resonance peaks of the structure. This increases the complexity of the control algorithms required to control such systems. Thus, employing a suitable control architecture based on the system dynamics is paramount for effective control. The literature's two commonly utilized control architectures are *centralized* and *decentralized* strategies.

Centralized Control Architecture

Centralized control refers to a control scheme in which a single processing unit collects all the sensor data, which utilizes a gain matrix and drives all the actuators, as illustrated in Fig.2.6. Essentially, data from different sensors distributed along the structure are combined, and a resultant output is computed.

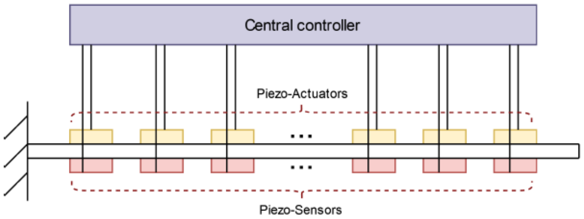

Figure 2.6: Centralized Control Architecture [69]

Centralized control has the potential to achieve optimal performance results with well-designed controllers since it has access to the global system and sensor information and can control all the actuators, taking into account couplings between them. This renders its utilization for highly complex and coupled systems appropriate and has the advantage that the controller can be designed so that individual modes can be influenced to different extents [70]. Techniques like linear–quadratic–Gaussian (LQG) control [71, 72], and modal filters are often employed to implement a centralized architecture [70, 73]. Modal filters are possible in two different configurations: continuous modal filters and discrete modal filters. In continuous modal filters, the electrode profile is shaped according to the strain distribution. Due to the orthogonality of modes, the sensor can sense a specific mode corresponding to the profile. Though, its usage is not practical for multiple modes [16]. In a discrete modal filter, data from the sensor array are combined using a linear combiner with certain weighting factors. Since such a modal filter is sensitive to one specific mode, it is required to accurately know the mode shapes in order to choose the appropriate weighting coefficient for the linear combiner [74].

However, a centralized architecture comes with several downsides. Firstly, due to several sensors and actuators involved, it poses stringent requirements of high communication throughput, fast data processing and transmission, and increased connectivity [75, 76]. These requirements result in added installation time, economic challenges, restricted maintenance, and technical challenges for the implementation of the feedback control system. With the increase in the dimensionality of the system, its required control computation increases exponentially, often rendering such architectures non-scalable. Second, it is not robust to sensor and actuator breakdowns. The entire control system is inoperable in the event that the central controller unit fails [77–79]. The controller's performance may degrade or become unstable as a result of aberrant hardware outputs or failures. There are measures to prevent this, like fault diagnostics and fault-tolerant controllers, but they entail additional design stages [80]. Lastly, a central processing unit-based system lacks modularity. Adding or removing sensors and actuators is not feasible without redesigning the central controller.

Decentralized Control Architecture

Decentralized control uses multiple control loops to control parts of the system independently. Essentially, the control problem is split into a set of smaller subsystems where the data of different sensors are not combined. The system consists of a number of collocated actuator/sensor pairs that each form an individual control loop, as illustrated in Fig.2.7.

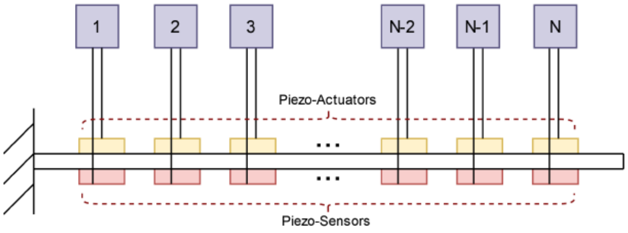

Figure 2.7: Decentralized Control Architecture [69]

In a decentralized control architecture, the control units only act locally; thus, the individual global properties of the system, such as mode amplitudes, cannot be selectively controlled [70]. In terms of vibration control, decentralized control is not capable to account for spillover effects [54]. On the other hand, decentralized control can make the system far more robust and scalable, distributing the computational load among several processing units [70]. In a real-world setting, it has the added benefit of eliminating the need for connections between various control locations and/or a central processing unit and enabling the development of identical modular actuator, sensor, and controller modules [81]. Moreover, such an architecture renders increased modularity. These systems frequently use single-input, single-output (SISO) controllers because they are convenient to compute and tune the parameters and enable the addition or removal of additional control loops without the need to redesign the controller [69]. Decentralized control, if applied in a collocated system, guarantees stability [81, 82].

2.1.5 Control Algorithms

This section explores various control algorithms that are frequently used for active vibration control of flexible structures that employ piezoelectric transducers.

Direct Velocity Feedback

Direct Velocity Feedback (DVF) is a control method in which a velocity measurement of the structure's degree of freedom is taken as an output, multiplied by its gain, and is directly fed back to the actuator, as schematically illustrated in Fig.2.8, where ξ, ω, ζ are modal coordinate, natural frequency and modal damping of the system, respectively; f is the modal control force, and g is the feedback gain.

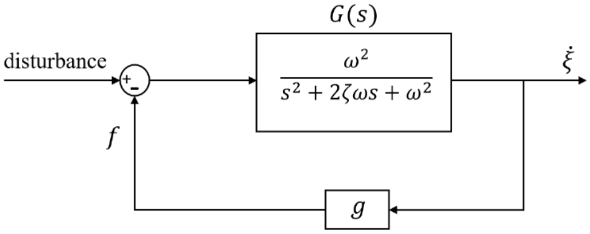

Figure 2.8: Closed-Loop System with Direct Velocity Feedback [83]

DVF does not prevent spillover effect from occurring but ideally can guarantee unconditional closed-loop stability for positive gains (g > 0) [61,82]. However, in a real system incorporating actuators with a finite bandwidth, modes occurring above this bandwidth can become unstable [84]. Moreover, in structures with piezoelectric transducers, the sensors measure strain in the structure which is proportional to the displacements. Thus, to incorporate such a velocity feedback scheme, the sensor output needs to be differentiated using an additional differentiator in the system, which is not preferable, as it can induce signal noise. In order to make sure that the compensator rolls off at high frequencies, some extra dynamics need to be added to it, although this could potentially cause instability [54, 84]. Lastly, DVF has high control effort throughout the actuator's frequency band, thereby leading to actuator saturation and reduced efficiency.

Lead Control

Lead control has a transfer function of the form,

$$H(s) = g\frac{s+z}{s+p} \tag{2.3}$$

It produces a phase lead in the band between z and p, thus providing active damping for modes within the band ($z < \omega_i < p$). The fact that collocated systems have a phase between

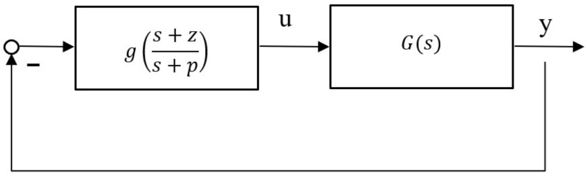

Figure 2.9: Closed-Loop System with Lead Control [85]

0° to 180° facilitates the phase of 90° when the target mode of the structure lies in the band. The controller does not have a roll-off and is limited by the roll-off structure.

The maximum achievable modal damping is given by,

$$\xi_{\max} \simeq \frac{z_i - \omega_i}{2\omega_i} \quad (\omega_i > z_i/3) \tag{2.4}$$

Note that the maximum achievable damping is controlled by the separation between the open-loop pole ω_i and the nearby zero z_i.

Integral Resonance Control

Integral resonant control is a simple and robust control that is generally employed for systems with collocated sensors and actuators (systems with zero-pole interlacing). An integrator is used to add damping to the system.

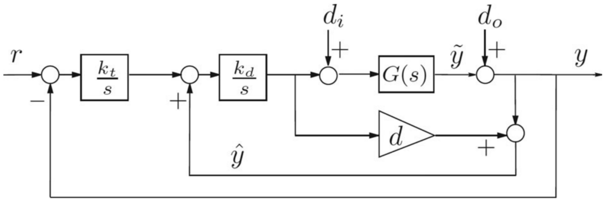

Figure 2.10: Closed-Loop System with IRC damping controller with external integral tracking gain [86]

Nanopositioning systems with piezoelectric elements usually suffer from hysteresis, which is usually compensated by a high gain tracking control, schematically presented in Fig.2.10. The gains of the integral tracking (k_t) and damping controller(k_d) are tuned simultaneously as independent tuning leads to avoid detrimental effects due to instability [86]. By adding a direct feed-through to a collocated system, the transfer function can be modified from containing resonant poles followed by interlaced zeros to zeros followed by interlaced poles. It is shown that this modification permits the direct application of integral feedback and results in good performance and stability margins [39]. The transfer function with the feedthrough term is,

$$G(s) = \frac{\gamma^2}{\left(s^2 + 2\xi\omega_p s + \omega_p^2\right)} + d_f \tag{2.5}$$

where ξ is the damping coefficient, ω_p is the natural frequency, and d_f is a feed-through term introduced to improve the location of zero in a truncated model.

IRC has been used on a range of different systems to demonstrate its robustness and effectiveness, such as in nanopositioning stages [87], cantilever beams with collocated piezoelectric pairs [39, 86], precise tip-positioning of a single-link flexible manipulator [88], precision servomechanism [89]. However, IRC utilizes higher gains in lower frequencies that may lead to actuator saturation, and an appropriate tuning of the controller requires a reasonable model of the plant.

Resonant Control

Resonant Control (RC) is a control technique that consists of the realization of an electrical dynamic vibration absorber. It is a second-order high-pass filter compensator with negative feedback, where the numerator dynamics convert the position feedback (from the piezoelectric sensor) to acceleration feedback, as presented in Fig.2.11.

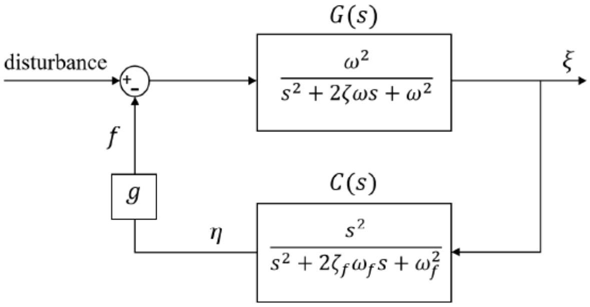

Figure 2.11: Closed-Loop System with Resonant Control [83]

The frequency ω_f is normally tuned to the same natural frequency of the structure of interest, and together with a proper choice for the parameters g and ζ_f vibration reduction can be achieved. Closed-loop stability is guaranteed for g $>$ 0.

Regardless, the high-pass filter characteristics cause a spillover effect due to the presence of uncontrolled dynamics by affecting the response on higher frequency modes while suppressing lower frequency modes [90]. Tuning the various RC compensators with special care is necessary to prevent the spillover effect while controlling numerous modes simultaneously. In practice, the compensator for a low-frequency mode should be tuned before the one for a higher-frequency mode [83]. Additionally, since actuators and sensors typically exhibit high-frequency dynamics that are not taken into account by the RC's high-pass filter and have the ability to destabilize the closed-loop system, RC is not enticing for practical implementation.

Positive Position Feedback

The Positive Position Feedback (PPF), first introduced by Goh and Caughey [91], to overcome the instability associated with finite actuator dynamics, has been thereafter one of the most commonly utilized control methods for active damping in structures integrating piezoelectric transducers. PPF uses position as the sensed signal, which is positively fed back through a second-order low-pass filter, as schematically presented in Fig.2.12, is tuned to the natural frequency of the mode to be suppressed, thus providing effective damping at this frequency.

In the modal domain, the two equations for a 1-DOF system and PPF compensator are:

System:

$$\ddot{\xi} + 2\zeta\omega\dot{\xi} + \omega^2\xi = \omega^2 f \tag{2.6}$$

Compensator:

$$\ddot{\eta} + 2\zeta_f\omega_f\dot{\eta} + \omega_f^2\eta = \omega_f^2\xi \tag{2.7}$$

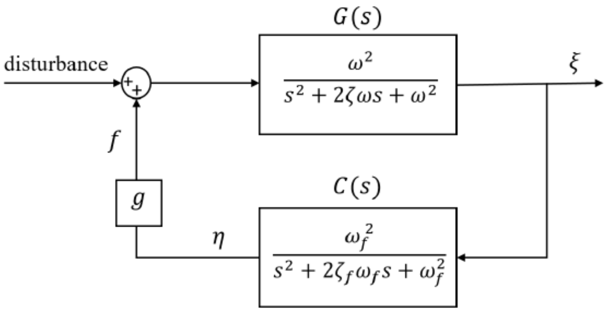

Figure 2.12: Closed-Loop System with Positive Position Feedback [83]

where ξ and η are the position coordinates of system and compensator; ω and ζ and ω_f and ζ_f are natural frequency and damping of system and compensator; $f = g\eta$ is the modal control force and g is the compensator gain. The closed loop system incorporating PPF is stable for [92] [54];

$$gG(0)C(0) < 1 \tag{2.8}$$

The frequency response of a PPF compensator is presented in Fig.2.13.

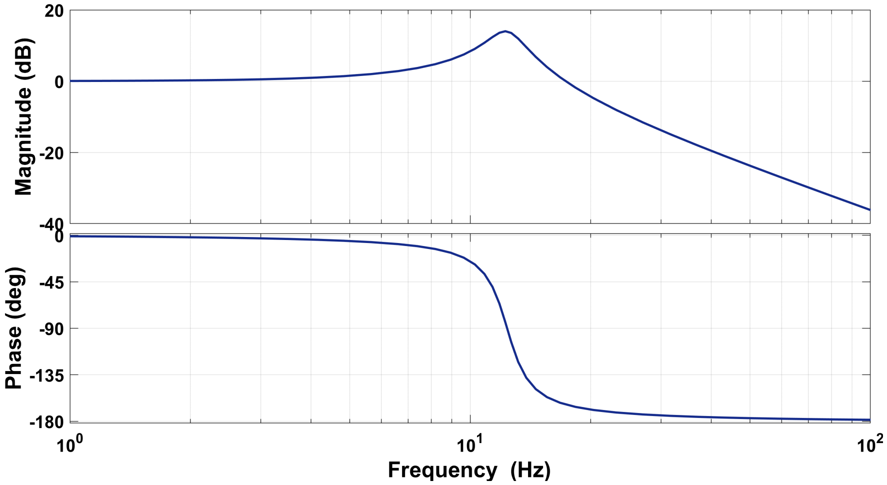

Figure 2.13: Frequency response of a PPF Compensator

PPF can be used in a parallel setup, with each block tuned to a different mode, to control multiple modes, as shown in Fig.2.14, if they are closely spaced. The possible damping is reduced by the narrow spacing between the poles and zeros, while the close spacing between the modes enhances the coupling between them, resulting in instability through spillover [93].

An illustration of a PPF compensator $C(s)$ in a parallel configuration is presented in Fig.2.15, where the compensator is targeted at the first three modes of the structure $G(s)$. The spillover can be observed by the increased flexibility of the closed-loop systems $T(s)$ at the low-frequency region.

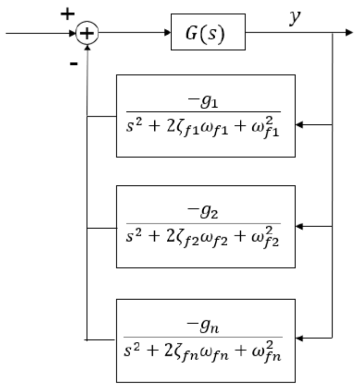

Figure 2.14: Closed-Loop System with Parallel Positive Position Feedback Loops [16]

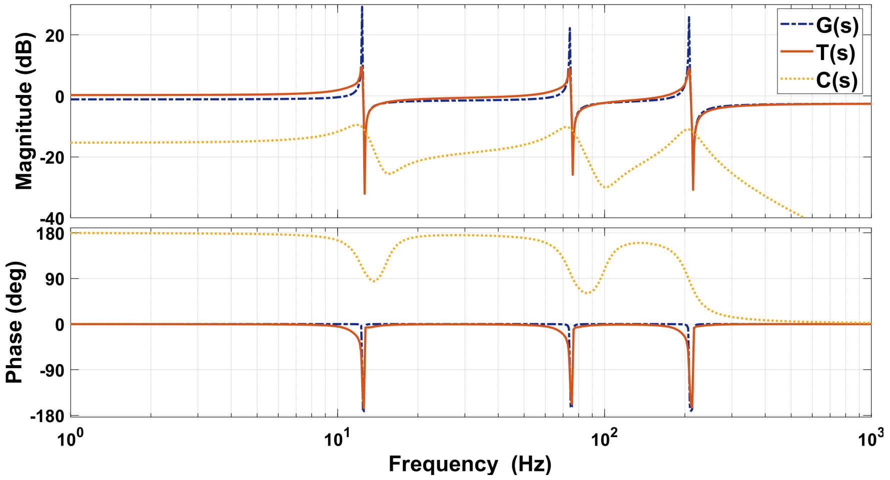

Figure 2.15: Illustration of a Parallel PPF Compensator used to suppress multiple modes

The low-pass filter characteristics cause the PPF to provide so-called active flexibility before the tuning frequency ω_f, active damping around ω_f, and active stiffness for higher frequencies [51]. The robustness of the compensator with respect to uncertain modal frequencies will increase as a result of a larger value of compensator damping, which assures a larger region of active damping. However, as a trade-off, it is expected to lead to slightly less efficient damping and result in increased flexibility at lower modes.

The effect of the tuning parameters, damping, and gain, in the PPF compensator is illustrated in Fig.2.16 and 2.17, respectively. It can be observed that a lower value of damping provides more peak attenuation, while higher values provide more robustness. On the other hand, a higher gain value provides more peak attenuation but also leads to increased active flexibility (spillover).

High-frequency spillover is prevented by PPF, whereas low-frequency spillover results in a change in resonance. Therefore, it has been demonstrated in numerous studies that in order to get optimum performance with multi-mode suppression, the PPF must be tuned from

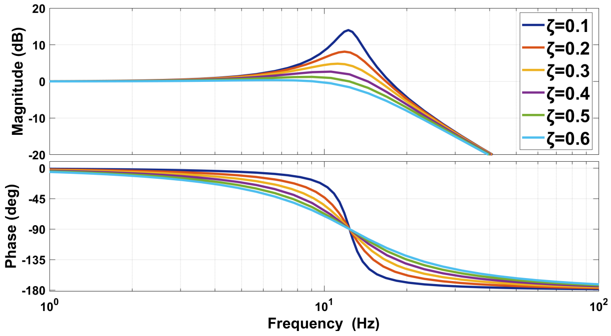

Figure 2.16: Effect of Damping on Frequency Response

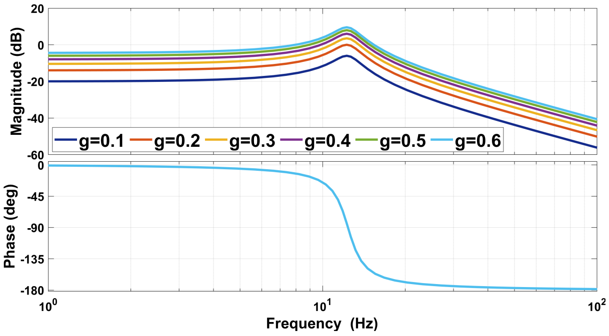

Figure 2.17: Effect of Gain on Frequency Response

higher to lower modes [83, 90]. Moreover, due to increased flexibility in lower frequencies with PPF results in significant steady-state errors and challenging multi-mode suppression control [94].

In addition to the numerous foundational research, the literature on positive position feedback also includes other variations that examine adaptive techniques or controller integration. A Modal Positive Position Feedback with a "time-sharing" strategy to share a small number of actuators between a larger number of modes was implemented in controlling the vibration of a complex flexible structure using a single piezo-electric active structural member [95–97]. An Adaptive Positive Position Feedback (APPF) is proposed for the multi-modal vibration control of frequency-varying structures [98]. PPF controller was applied to the PZT actuators for suppressing multi-mode vibrations while slewing the single-link flexible manipulator, considering both set-point and trajectory tracking control [99]. A Modified Positive Position Feedback (MPPF) was proposed, which employs a first-order compensator that provides damping control and a second-order compensator for vibration suppression in a collocated structure [100, 101]. Experimental research was done on the active vibration control of a free rectangular sandwich plate utilizing the Positive Position Feedback (PPF) algorithm [53, 102]. A fractional-order Positive Position Feedback (PPF) compensator was proposed for active vibration control (AVC) of a rectangular carbon fiber composite plate and exhibits encouraging results in decreasing the spillover effect imposed on by uncontrolled modes [83]. A technique to design the positive position feedback controller with the optimal damping based on the H_2 norm was demonstrated in a single DoF system [103].

2.2 Piezoelectric Transducers

Piezoelectric transducers have been extensively used in structural vibration control applications [54]. Their wide utilization in this specific application can be attributed to their excellent actuation and sensing abilities which stem from their high electro-mechanical coupling coefficient [61]. Piezoelectric transducers are bonded to or embedded in a composite structure for vibration control purposes. Besides the fact that these transducers are lightweight and, thereby, not significantly influence the dynamics of the structure, these transducers offer quite some advantages [104], as mentioned below:

- Fast Response
- Large Force
- Linear Response (for small deflections)
- High Sensitivity
- High Signal to Noise Ratio
- High Power Density

2.2.1 Piezoelectric Phenomenon

Piezoelectricity, a concept discovered by Pierre and Jacques Curie in 1880 [105], means electricity generated by pressure [61]. This implies that electric charges are produced when mechanical stress is applied to a piezoelectric material. This is called the direct piezoelectric effect and can be effectively used as a sensing mode to sense a deformation in the host structure. This can be schematically visualized via Fig.2.18, where a component, initially under no-load conditions, produces an electric charge to appear at the electrodes due to the resulting change in polarization when subjected to an external force (F).

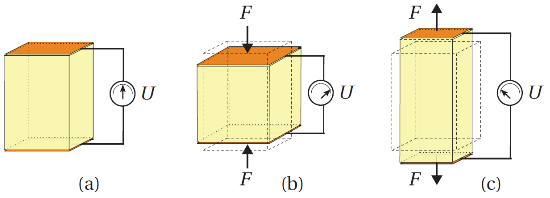

Figure 2.18: Direct piezoelectric effect in a rectangular shaped component [106]

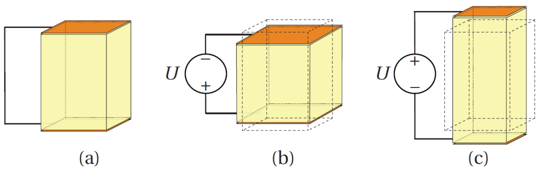

Figure 2.19: Inverse piezoelectric effect in a rectangular shaped component [106]

In addition to the direct piezoelectric effect, it is also possible to provide electric charges to a piezoelectric material which will render mechanical deformations. This is called the inverse piezoelectric effect [106] and can be effectively used as an actuation mode. This is illustrated in Fig.2.19 where an application of an electric field along the length direction causes a dimensional change in the length and the perpendicular directions.

The physical behavior of a general piezoelectric material is best described via the constitutive equations presented in Eq.(2.9), which describes the use of a piezoelectric transducer as an actuator, and Eq.(2.10) describing the use of the transducer as a sensor [54].

$$S_{ij} = s^{E}_{ijkl} T_{kl} + d_{kij} E_k \tag{2.9}$$

$$D_i = d_{ikl} T_l l + e^{T}_{ik} E_k \tag{2.10}$$

where

T_{ij} = Components of the stress tensor
S_{kl} = Components of the strain tensor
s^E_{ijkl} = Compliance tensor under constant electric field
E_k = Applied electric field
D_i = Vector of electric displacements
ϵ^T_{ik} = Dielectric constant under constant stress
d_{ikl} = Piezoelectric constants

Eq.(2.9) and (2.10) assume that the direction of polarisation is along the z-axis.

For the sake of brevity, engineering vector notations are frequently used in place of the stress and strain tensor notations in literature.

$$T = \begin{Bmatrix} T_{11} \\ T_{22} \\ T_{33} \\ T_{23} \\ T_{31} \\ T_{12} \end{Bmatrix} \quad S = \begin{Bmatrix} S_{11} \\ S_{22} \\ S_{33} \\ 2S_{23} \\ 2S_{31} \\ 2S_{12} \end{Bmatrix} \tag{2.11}$$

With these vector notations, Eq. (2.9) and (2.10) can be respectively reformulated in the matrix form as:

$$\{S\} = [s]\{T\} + [d]\{E\} \tag{2.12}$$

$$\{D\} = [d]^T\{T\} + [\epsilon]\{E\} \tag{2.13}$$

2.2.2 Piezoelectric Actuators

Piezoelectric elements can be used in different actuation modes, depending on the topology and the direction of polarization in the piezoelectric material. The piezoelectric coefficient, d_{ij}, signifies that a strain is developed along the i-axis when the electric field is applied along the j-axis (external stresses are held constant). For an isotropic structure, there are three kinds of actuation modes possible.

Piezo Stack Actuator

In order to achieve a higher displacement, several actuators stacked in the reverse polarization direction are utilized in this configuration, as illustrated in Fig.2.20. The d_{33} coefficient governs this kind of actuator. This implies that the structure will extend in the direction of the electric field applied to it.

Piezo Shear Actuator

In this kind of actuator, when an electric field is applied to the structure, it will have a shear deflection, as depicted in Fig.2.21. This type of actuator depends on the d_{15} coefficient.

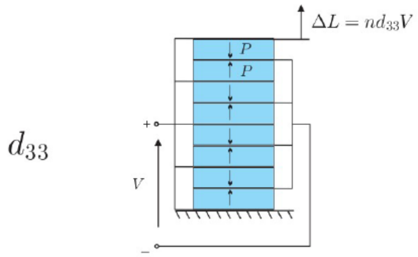

Figure 2.20: Piezo Stack Actuator [54]

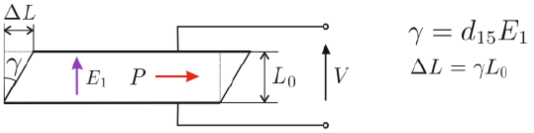

Figure 2.21: Piezo Shear Actuator [54]

Piezo Bending Actuator

These actuators' primary function is to produce bending, which is accomplished by the piezo transducer's d31 effect. Typically, these actuators are directly bonded to a beam using a substrate. An axial strain along the x-axis results from the application of a voltage in the polarization direction (z-axis - E_3). However, the mobility of the piezo is limited since the actuator is connected to the relatively rigid beam. This actuator is illustrated in Fig.2.22.

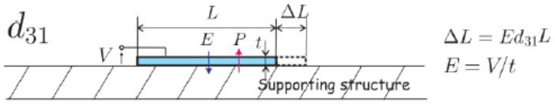

Figure 2.22: Piezo Bending Actuator [54]

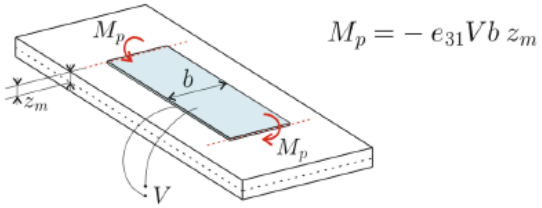

Figure 2.23: Model of Piezo Bending Actuator [54]

The strain (ϵ_p)in the axial direction of the piezoelectric bender when the Voltage (V) is applied in the polarisation direction given by,

$$\epsilon_p = \frac{d_{31}V}{t} \tag{2.14}$$

where t is the thickness of the piezoelectric actuator. The strain distribution is assumed to be linear, considering the perfect attachment of the actuator. The stress is discontinuous, and the axial force acting on the center of mass of the beam creates a moment.

A flexible system's bending modes are frequently of interest in AVC. In these circumstances, applying bending moments at specific locations on the flexible structure is most appropriate to counteract these bending modes, as illustrated in Fig.2.23. Piezoelectric bending actuators are, therefore, best suited for use in damping vibrations in beams.

2.2.3 Piezoelectric Sensor

As explained in subsection 2.2.1, piezoelectric materials can be used both in actuation mode and sensing mode. Thus, the actuators presented above can be utilized as strain sensors, where the sensor would sense the strain parallel to the longitudinal direction of the transducer. A charge is generated by the sensor, which is proportional to the d_{31} mode, which is collected by the electrodes in the polarisation direction. The generated voltage (V_p) is related to the charge as:

$$V_p = \frac{q}{C_p} \tag{2.15}$$

where C_p is the capacitance of the piezoelectric sensor. The sensor voltage (V_s) is found to be [61],

$$V_s = \frac{d_{31} E_p w}{C_p} \int_l \epsilon_1 dx \tag{2.16}$$

where ϵ_1 is the strain in the axial direction averaged over the sensor length, and E_p is Young's modulus of the sensor. The strain (ϵ_1), can be computed using:

$$\epsilon_1 = \frac{C_p V_s}{(1 - v) d_{31} E_p l w} \tag{2.17}$$

where ν is the Poisson's ratio of the material.

2.2.4 Hysteresis

Hysteresis is the major form of nonlinearity present in piezoelectric transducers [61]. On a macroscopic level, hysteresis is caused by internal energy losses (or power dissipation) in piezoelectric materials when expanding or contracting. The hysteresis associated with piezoceramics exhibits nonlocal memory. This indicates that the actuator's present output state depends not only on the voltage input at the moment but also on its previous behavior [107]. In feedback control systems, this can be extremely problematic if it is not taken into consideration because, depending on the "memory" (or previous history) stored in the material, the identical input value might result in a variety of distinct output states. The ceramic's capacitance changes as the voltage rises, and as a result, so does the energy loss, changing the major axis angle. The area bounded by the hysteresis loop is directly proportional to the energy loss for each cycle [108]. To reduce the effect of the nonlinearity present due to hysteresis, it is suggested to utilize charge control instead of voltage control. This can essentially be accomplished by driving the piezoelectric actuator patch by a charge amplifier. It has been reported from several studies that piezoelectric actuators exhibit up to 80% less hysteresis when driven by charge amplifiers [109,110]. In a piezoelectric transducer, hysteresis mainly exists between the voltage and mechanical strain rather than the charge (or current) and strain [111]. This is illustrated in Fig.2.24 and Fig.2.25.

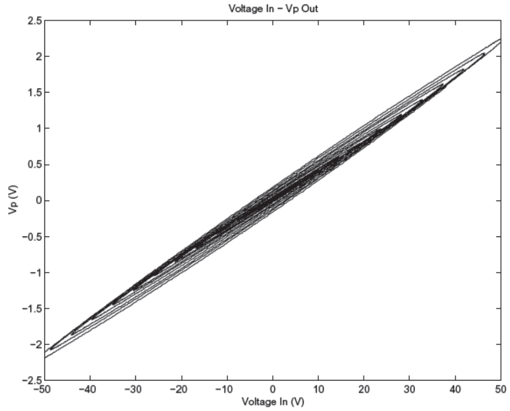

Figure 2.24: Voltage Control [61]

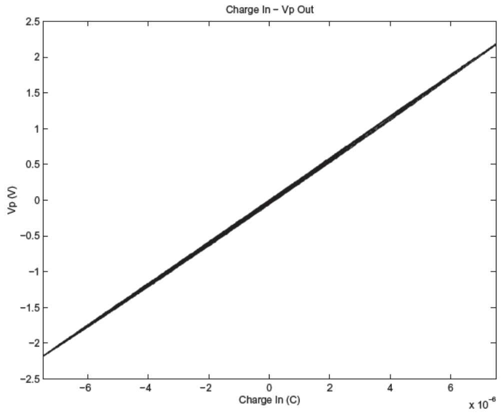

Figure 2.25: Charge Control [61]

2.2.5 Placement of Piezoelectric Transducers

Piezoelectric transducers can operate as sensors and actuators in an AVC system; thus, it is essential to investigate how their placement affects damping performance. Different optimization criteria for optimally locating piezoelectric patch placements have been researched in the state-of-the-art literature. Some of the prevailing criteria are based on maximizing modal forces/moments [112–117], maximizing deflection of the host structure [118], minimizing control effort [119], and maximizing the degree of controllability and observability based on grammians [120–122]. All these optimization methods suggest that the most efficient strategy is to position actuators and sensors where the highest modal strain is generated in respective structural modes. Therefore, collocated sensor-actuator pairs can effectively suppress the relevant mode when positioned in a region with high modal strain. The most commonly utilized strategy is based on maximizing the modal forces/moments described below.

Active Flexures with Collocated Piezoelectric Transducers

The presence of parasitic resonance in the system causes undesired movement and bending of the end-effector platform, resulting in tip deflection of the flexures attached to it. To counteract these deflections, piezoelectric bender sensors and actuator patches are strategically placed in a collocated configuration on the flexure.

When the flexure undergoes transverse displacement w, it induces a uniform strain distribution throughout its structure, including the sensor patch bonded to it. This strain causes a small extension of the patch in the longitudinal direction, which is directly proportional to the tip displacement [61]. The output charge of the sensor is directly proportional to the difference in slopes w', or rotations $\Delta\theta$, at the two extremities of the sensor strip.

$$Q \propto \Delta\theta_i^s \propto [w'(b) - w'(a)] \tag{2.18}$$

As a result, a charge is generated and accumulated across the sensor electrodes, leading to the production of a corresponding voltage signal. This voltage signal is then fed into the damping controller, which processes it to generate an actuation voltage. The actuation voltage is applied to the actuator patch electrodes, causing the patch to undergo an extension. This extension generates a counter-torque (M) that opposes the flexure bending at the resonance frequency. The torque magnitude is determined by the equation.

$$M = -e_{31} z_m b_p V = g_a V \tag{2.19}$$

where V is the voltage applied to the actuator, and g_a is the actuator gain, which can be computed based on the physical characteristics of the actuator, such as its size and material properties. The transfer function between the actuator voltage V and the sensor output v_0 is thus given as

$$\frac{v_0}{V} = G_p(s) = g_a g_s \sum_{i=1}^{n} \frac{\Delta\theta_i^a \Delta\theta_i^s}{\mu_i \left(s^2 + 2\xi_i \omega_i s + \omega_i^2\right)} \tag{2.20}$$

where g_a and g_s are the actuator and sensor gains, ω_i is the natural frequency of mode i, ξ_i the modal damping ratio, and μ_i the modal mass.

The piezoelectric patches are typically positioned at locations on the flexure where the maximum strain is induced by a specific eigenmode that needs to be suppressed. This strategic placement ensures reasonable observability and controllability for the flexure resonance in the collocated channel. By locating the patches at these specific points of maximum strain, they can effectively sense and actuate in response to the undesirable deformation or vibration, allowing for targeted control and mitigation of the eigenmode.

2.3 Distributed Actuation

In the context of mechatronic system design, distributed actuation denotes that the actuators (and sensors) are placed and distributed across the surface of the structure to account for reasonable controllability and observability of a certain finite number of modes. The distribution of sensing and control is extremely useful for the design and realization of intelligent structures [112]. An intelligent structure is one that can recognize the present dynamic state of its own structure and can make intelligent decisions regarding compensations for disturbances and adequately generate actuation forces [37].

Piezoelectric transducers can be directly integrated into structures and distributed throughout them, which renders them quite advantageous for controlling deformable structures. However, one of the main drawbacks of piezoelectrics is that the induced strains are highly constrained, which subsequently limits the amount of force that can be applied. Thus, a number of piezoelectric transducers are distributed along the structure such that they can supply sufficient input to achieve the desired objective. Numerous studies have been performed on deformable structures integrating distributed piezoelectric actuators for active vibration control, such as in flexible cantilever beams [123–127], thin plates [128, 129], and shell structures [126, 130, 131]. An illustration of such distributed actuation is presented in Fig.2.26.

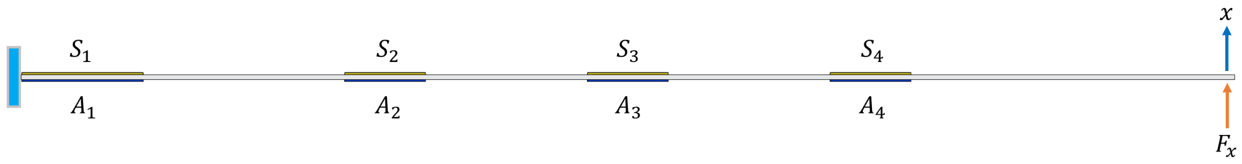

Figure 2.26: Illustration of Distribution Actuation using Piezoelectric Transducers

2.3.1 Over-Actuation in Vibration Control

Distributed actuation can be further classified based on the number of modes to be controlled based on the number of actuators employed in the system. In this case, when the number of actuators is higher than the number of controlled modes, it is termed as *overactuation*.

Traditional motion systems, having a goal of tracking a certain setpoint by the end-effector of the system, often experiences excited resonances in the quest for more accurate and faster systems [59]. Actuators are placed in such systems to actuate the rigid body motion and avoid excitation of residual resonances and other disturbances via the feedback path [31]. However, for optimal damping of resonances, actuators have to be optimally placed to influence the resonance as much as possible, which usually doesn't coincide with the optimal locations for feedforward control (reference tracking). This paved the way for the concept of utilizing additional actuators in motion systems exclusively for disturbance rejection and flexible mode suppression. In contrast, the other actuators are placed to get the desired motion. This enables decoupling the controllability of resonance modes for feedback and feedforward path. In this way, the controllability of the internal dynamics of the structure can be both maximized for feedback and minimized for feedforward [56].

To illustrate the benefits of the overactuation, an analysis performed by Schneiders and Steinbuch on a levitated beam is presented [58, 132]. The beam consists of two rigid body modes to be actuated for motion, while one elastic mode (parasitic mode) is to be suppressed, as illustrated in Fig.2.27. A traditional design approach will require two actuators to be placed to drive the system. The control bandwidth is limited by the presence of the first elastic

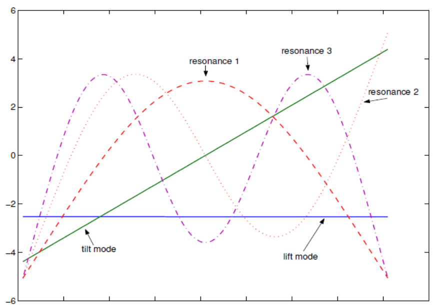

Figure 2.27: The first 5 eigenfunctions of the beam [58]

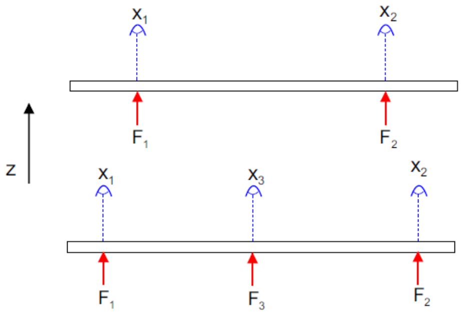

Figure 2.28: Motion system: (top) two actuators, two sensors. (bottom) three actuators, and three sensors. [58]

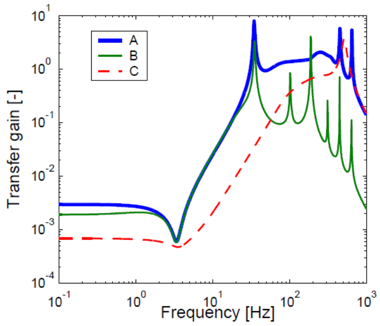

Figure 2.29: Frequency response function from the reference signal r to the performance variable z [58]

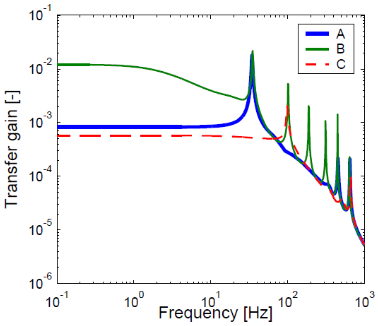

Figure 2.30: Frequency response function from the external disturbance d to the performance variable z [58]

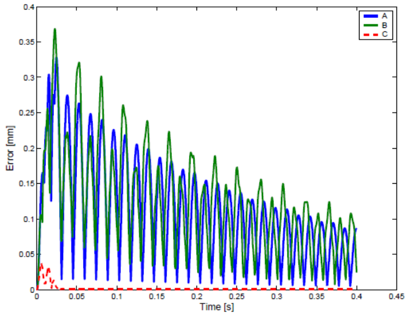

Figure 2.31: Absolute maximum of the tracking error over the complete spatial domain of the beam [58]

mode. The study considers three different cases of actuator configuration for comparison. The system has two sensors and two actuators for cases A and B. This would be a motion control application's typical topology. A weak controller is employed in case A, while a stiff controller is implemented in case B's system. The controllers in both situations use a lead-lag component to increase dampening. To investigate over-actuation usage, scenario C adds an extra sensor and an extra actuator. This is schematically demonstrated in Fig.2.28.

To observe the benefits of overactuation in the system, the tracking performance and disturbance rejection characteristics are examined for the closed-loop system in Fig.2.29 and Fig.2.30, respectively. Another performance measure based on the physical tracking error is also presented in Fig.2.31. All these plots show that the overactuated system outperforms the traditional approach in both the spatial and frequency domains, with significantly reduced tracking errors and reduced transfer gains, respectively.

In another study case, a wafer stage is presented to show the potential performance improvement of overactuation and oversensing [133]. The control design in the vertical direction is considered, which includes the transnational direction (z), and rotations R_x and R_y, as depicted in Fig.2.32. Four actuators are employed, where actuators (a_{1-3}) are placed below the corners of the stage, and the actuator (a_4) is positioned at the middle of the line between the center and a_2. Moreover, apart from the corner sensors (s_{1-3}), the piezo sensor (s_4) is placed at the middle of the line between the center and s_2, which measures the strain of the

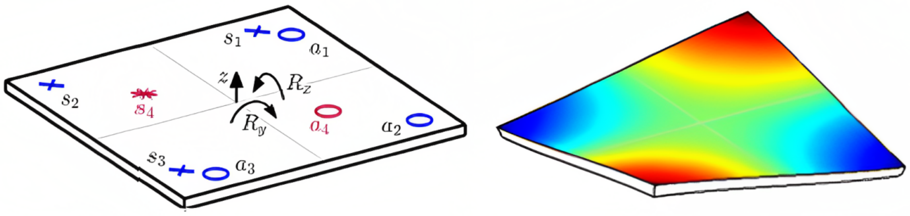

Figure 2.32: Inputs and outputs used to counteract undesired torsion of the wafer stage [133]

wafer stage. Since four actuators and sensors are available to control the three rigid-body DoFs, there is freedom left to actively control the flexible dynamical behavior of the wafer stage.

The main result is an increase of the torsion mode frequency from 143 to 193 Hz as well as increased damping of this loop, as illustrated in Fig.2.33. This enables enhanced performance for the remaining equivalent plant since this torsion mode was performance-limiting due to non-collocated dynamical behavior. In particular, active control of the torsion mode implies that a higher cross-over frequency can be achieved in the original motion DoF [133].

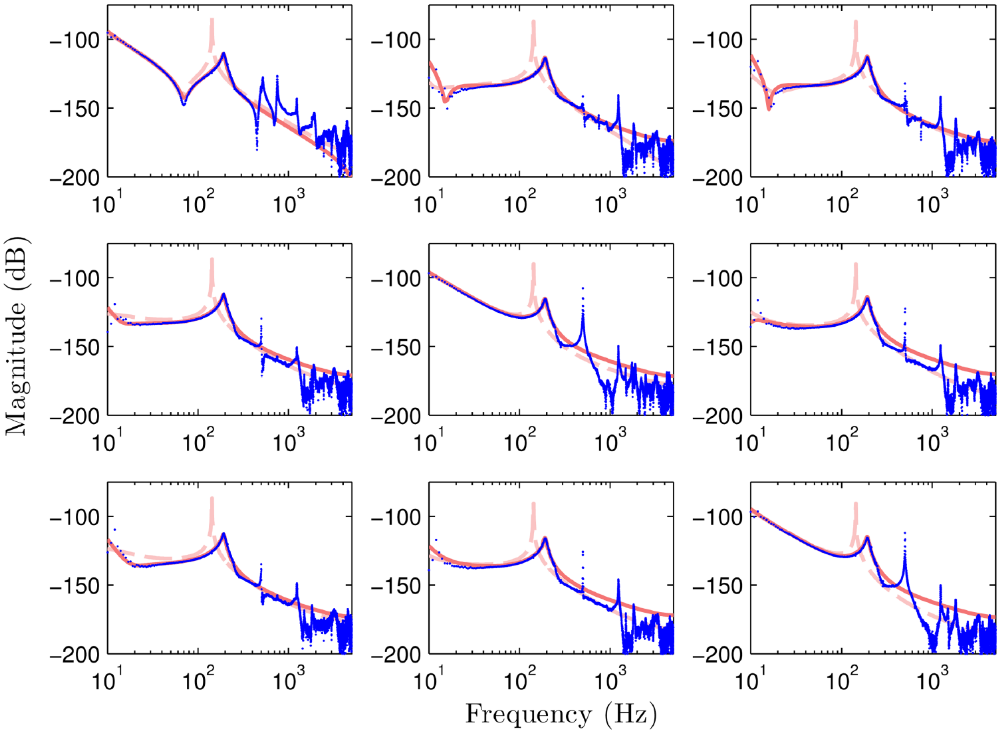

Figure 2.33: Overactuated Plant (blue dotted), parametric fit (red solid) under the active control of the torsion loop in comparison with the initial model (red dashed) of motion with DoF $[z, R_x, R_y]$ [133]

3 | Overactuation for Active Damping in Compliant Positioning Stage using Piezoelectric Transducers

This chapter presents the scientific contributions of this work and is presented in a scientific journal paper format to be self-contained. The paper proposes a novel overactuation-based strategy to improve the damping, disturbance rejection, and reference tracking performance of a compliant positioning stage using piezoelectric transducers.

The work has been accepted to be presented at the 5th **DSPE Conference on Precision Mechatronics**, which will take place on September 26-27 in Sint Michielsgestel, The Netherlands.

Overactuation for Active Damping in Compliant Positioning Stage using Piezoelectric Transducers

Abstract

Integrating compliant mechanisms into high-precision motion systems has facilitated the development of lightweight and frictionless designs. However, these systems often face challenges related to low-frequency parasitic resonance modes and limited structural damping, leading to compromised position accuracy and restricted control bandwidth. While notch filters are conventionally used to suppress these parasitic resonance peaks and enable higher control bandwidths, undesired effects persist in closed-loop disturbance rejection performance. To address this limitation, researchers have explored the concept of overactuation, employing a greater number of actuators than the number of rigid body modes to be controlled. This approach allows for additional closed-loop feedback interconnections, offering increased freedom to enhance performance. This research presents a novel overactuation-based solution where: (1) the use of additional actuators enables the implementation of active damping control to improve closed-loop disturbance rejection performance and (2) the integration of multiple distributed piezoelectric bender actuator-sensor pairs in a collocated configuration enhances damping performance. A mathematical framework is formulated to demonstrate the benefits, and an experimental setup is constructed to validate the numerical findings and serve as a proof of concept. The proposed solution effectively suppresses the parasitic resonance mode, enhances disturbance rejection on the end-effector, and enables higher control bandwidth in the positioning system.

Index Terms

Overactuation, Active Damping Control, Piezoelectric Transducer, Positioning Stage, Distributed Actuators

I. INTRODUCTION

The ever-increasing demands for high throughput and positioning accuracy, driven by accelerating technological advancements in nano-science, have led to extensive utilization of positioning systems with flexure-based mechanisms in the high-tech industry. These systems find applications in various fields, including wafer alignments [1], scanning probe microscopes [2], [3], micromanipulators [4]–[7], nanomanufacturing [8], metrology [9], [10], and MEMS devices [11], among others. Flexures offer the necessary range of motion while eliminating undesirable friction and backlash [12], [13]. However, their inherent low damping characteristics lead to lightly damped higher-order parasitic vibration modes at relatively low frequencies in lightweight and flexible systems [14], introducing unwanted vibrations that compromise motion performance and accuracy [15]. The presence of a small structural damping ratio causes a significant phase drop, resulting in a low-gain margin for the vibrational dynamics [16]. Additionally, the complex geometries of these systems often lead to non-collocated dynamics, which exhibit non-minimum phase behavior, limiting control bandwidth to a small fraction of the parasitic resonance frequency [17], [18].

To address these limitations, numerous techniques, including feedforward [2], [19], inversion [20], and notch filters [21], [22], have been utilized to mitigate parasitic vibration modes. Although these techniques can yield favorable outcomes for systems with accurate models and known references, they lack robustness in the face of system parameter uncertainties and external disturbances.

As an alternative approach, feedback controllers are explored to address the damping of parasitic resonance modes and enhance robustness to uncertainties within systems. Among these controllers, widely used fixed-structure low-order schemes include integral resonant control (IRC) [23], [24], integral force feedback (IFF) [25], [26], positive position feedback (PPF) [27], [28], positive velocity and position feedback (PVPF) [29], and positive acceleration, velocity, and position feedback (PAVPF) [30]–[32]. The IFF scheme, while advantageous for its utilization of a low-noise piezoelectric force transducer and high bandwidth capabilities, is limited by its requirement for a force transducer, restricting its widespread use. PVPF and PAVPF controllers have shown effective damping when appropriately tuned, but their sensitivity to noise, especially in systems equipped with position sensors, poses challenges due to numerical differentiation. The PPF controller has gained extensive application due to its ability to strategically position system poles for effective damping and its simplicity, making it suitable for suppressing multiple modes [33], [34]. It exhibits increased robustness with higher controller damping values and second-order high-frequency roll-off characteristics [35]. Besides positioning systems, the PPF controller is applied in vibration control of thin beam and plate-like structures [36], [37]. Frequently, it is combined with collocated piezoelectric bender transducers to provide active damping. The collocated configuration ensures pole-zero interlacing and a phase range between 0-180° [51], contributing to an unconditionally stable system and effective operation of the PPF controller in this setup.

In conventional single-axis positioning systems, a Single-Input Single-Output (SISO) configuration is typically employed, utilizing a single actuator and sensor to control. Ideally, the actuator is positioned to facilitate rigid body motion while avoiding the excitation of unwanted parasitic resonances. However, when active damping is required, the same actuator is used to suppress undesired resonances and external disturbances through the feedback loop. Furthermore, the attainable maximum damping performance is restricted by both the stability conditions of the damping feedback controller and the saturation limits of the actuator. This creates a conflict, as positioning the actuator for effective damping of undesired modes may compromise optimal motion-tracking performance, where positioning aims to minimize the excitation of these parasitic modes. Thus, a trade-off is often necessary to achieve satisfactory tracking and damping performance. One method is to increase mechanical stiffness by adding mass to the mobile components, but it is considered undesirable due to drawbacks such as requiring higher actuation forces, leading to greater resistive heating. To address this limitation, researchers have explored the concept of overactuation, involving the use of more actuators than the number of rigid body modes to be controlled [39]. This technique establishes additional closed-loop feedback interconnections, offering increased freedom to enhance performance [40], [41], allowing for improved control over system modes while maintaining a favorable balance between the tracking and damping feedback paths [42]–[44].

In non-collocated compliant positioning systems, the second resonance peak induces undesirable vibrations and limits control bandwidth. While conventional notch filters enable higher control bandwidth, the effect of this parasitic resonance is still observed in closed-loop disturbance rejection performance. This paper proposes a novel overactuation-based solution to overcome these limitations through active control of flexible dynamical behavior, with the main contributions as follows:

(C1) The use of additional actuators enables the implementation of active damping control to improve closed-loop disturbance rejection performance.

(C2) The integration of multiple distributed piezoelectric bender actuator-sensor pairs in a collocated configuration enhances damping performance.

The paper is structured as follows: Section II provides an overview of the experimental setup used. Section III presents a mathematical model for evaluating system dynamics, including the extended configuration with additional sensors and actuators. Section IV introduces the control architecture with additional actuators and sensors and mathematically substantiates the contributions of the paper, particularly enhancing disturbance rejection using active damping control in the overactuation configuration (C1), and analyzing the impact of additional distributed actuators on damping performance (C2). Experimental demonstrations and validations of the contributions are presented in Section V. Finally, Section VI summarizes the conclusions drawn from the study.

II. SYSTEM DESCRIPTION

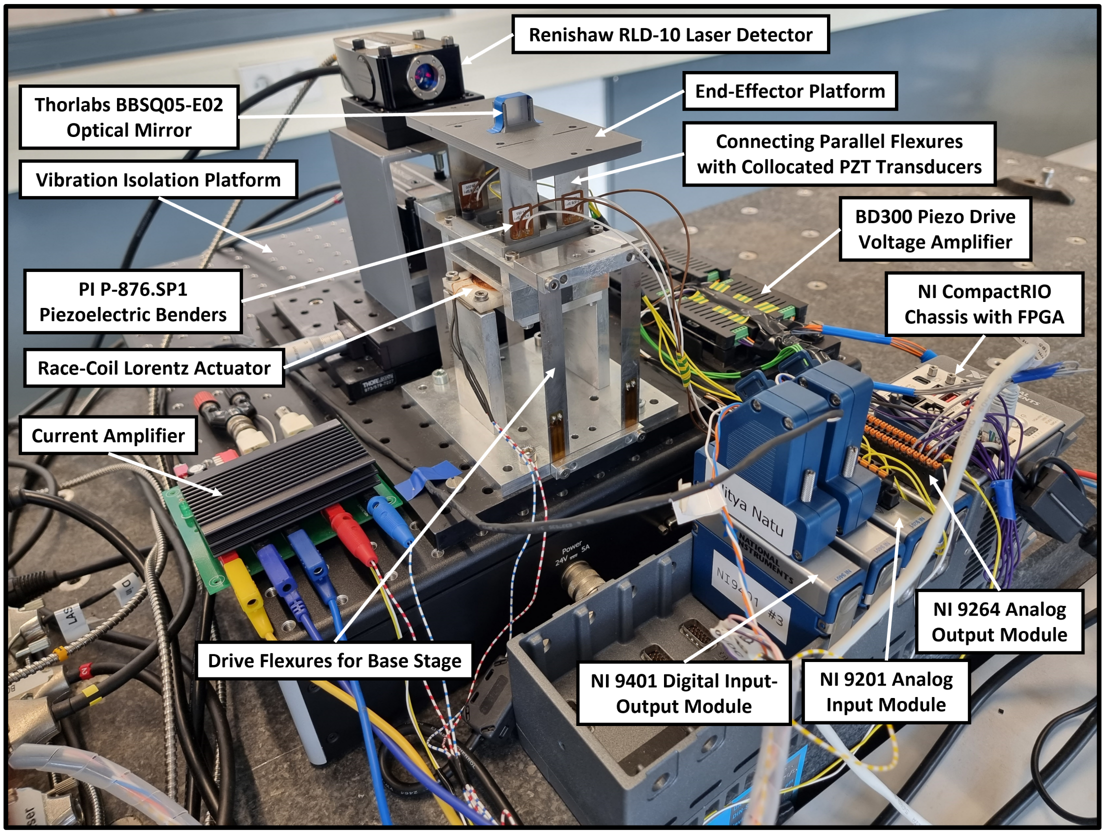

Fig. 1: Experimental Setup

The experimental setup described in this paper is a single-axis dual-stage compliant micro-motion system, as illustrated in Fig.1. The system consists of two stages in a series: a base stage and an end-effector platform. The two stages are connected to each other with a set of four parallel guiding flexures, while another set of parallel flexures connects the base mass to the reference ground. These guiding flexures provide the translation degree of freedom to the stages. The entire setup is placed on a vibration isolation platform.

To actuate the base stage, a race-coil Lorentz actuator is employed. The position of the end-effector platform is measured using a laser interferometer (with a resolution of 39.5 nm) and an optical mirror mounted on the end-effector platform. The Lorentz actuator utilized in the experimental setup generates a bi-directional force that is directly proportional to the input current. A current amplifier is utilized to amplify and convert input voltage signals into the necessary current levels with a constant gain factor during the amplification process. By precisely controlling the input current to the Lorentz actuator, the desired force output can be achieved, enabling precise actuation and control of the system.

For overactuation, additional piezoelectric bender actuator and sensor pairs are bonded to the flexures connecting the base stage and end-effector at locations of maximum strain. This ensures reasonable observability and controllability of the flexure resonance in the collocated channel. The piezoelectric actuators are driven by voltage signals amplified by a voltage amplifier. The actuation signals and control are facilitated by an NI CompactRio system with an embedded FPGA. The system includes various analog and digital input-output modules that enable the transmission and reception of signals for implementing the control approach. The control scheme is implemented using NI LabView software, which serves as the interface between the host computer and the micro-motion system.

III. SYSTEM MODELLING OF COMPLIANT MOTION SYSTEM

This section presents the mathematical modeling of the double-degree-of-freedom positioning system, providing a comprehensive understanding of its behavior, facilitating system performance evaluation, critical parameter identification, and the design of control strategies.

A. Numerical Model

In this subsection, a numerical model is formulated for the double-degree-of-freedom single-axis dual-stage positioning system depicted in Fig.2. The numerical model is created using an extension of the SPACAR software, which is a multi-body dynamics simulation tool widely used for modeling mechanical systems [45]. The model incorporates the active areas of the piezoelectric transducers to accurately capture the system's frequency response. By including the characteristics of the piezoelectric transducers in the model, a more realistic representation of the system's behavior is achieved.

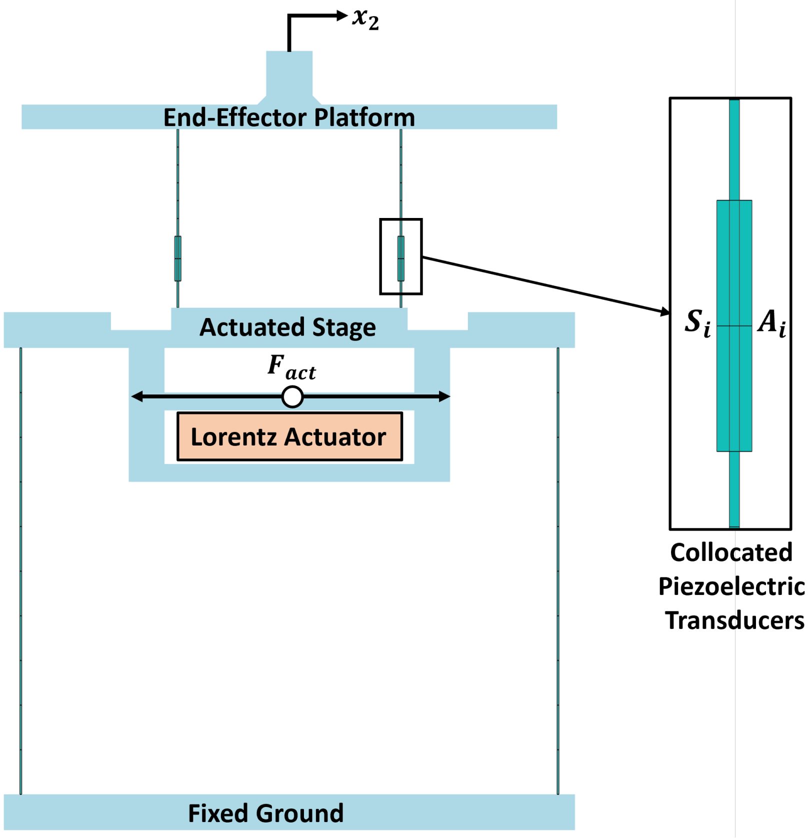

Fig. 2: Numerical Model designed in SPACAR

The modal behavior of the system is examined to understand its vibration characteristics, as shown in Fig.3. The analysis displays two prominent modes: the desired rigid-body motion mode and the undesired parasitic vibration mode. The desired rigid-body motion mode occurs at a frequency of approximately 6.5 Hz. This mode corresponds to the primary resonance of the base flexures, which allows the system to move as a rigid body without inducing significant vibrations in other modes. This mode is crucial for achieving accurate and controlled positioning of the system. On the other hand, the undesired parasitic vibration mode occurs at a frequency of 82 Hz. This mode is associated with the primary resonance of the connecting parallel flexures. These vibrations are unwanted and can compromise the performance and accuracy of the system.

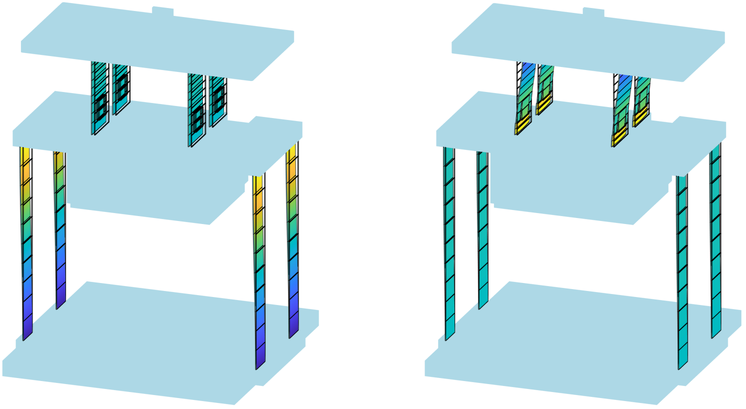

(a) Rigid Body Mode at 6.5 Hz (b) Parasitic Resonance Mode at 82 Hz

Fig. 3: System Modal Behaviour

B. Simplified Analytical Model

The analytical model complements the numerical approach and provides a mathematical framework to analyze and understand the system's dynamics [46]. The analytical model is developed by simplifying the system to a double-mass-spring-damper configuration, as depicted in Fig.4. This approximation effectively represents the behavior of the system's first two primary modes of interest. The system is assumed to exhibit linear behavior when subjected to small displacements of the end-effector platform.

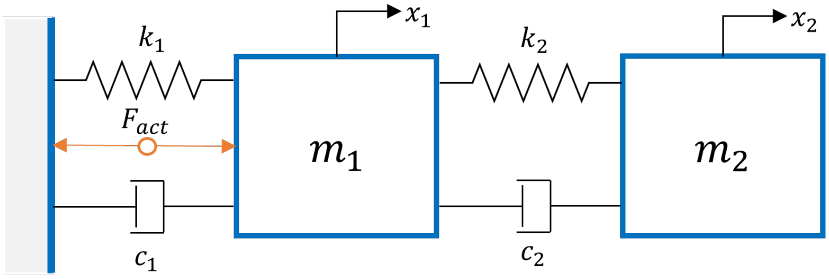

Fig. 4: Equivalent Analytical Model

Here, m_1 and m_2 represent the mass of the base stage and end-effector platform, while k_1, c_1, and k_2, c_2 represent the total stiffness and damping for the base flexures and connecting flexures respectively. The combined guiding drive stiffness for parallel flexures in the x-direction corresponding to their primary resonance is given by [47];

$$k_{i_x} = n_f \cdot \frac{12EI}{L^3} - \frac{6F_y}{5L} \quad \text{for i = 1,2} \tag{1}$$

In the given equation, the term EI represents the bending moment, where $I = wt^2/12$ is the moment of inertia. The parameter E denotes Young's modulus of the flexure material, and n_f represents the number of parallel flexures. The second term in the equations represents the negative stiffness induced by the normal load of the plate springs. The normal load can be expressed as $F_y = mg$, where m is the mass of the mover as perceived by the parallel flexures and g is the acceleration due to gravity.

Similarly, the combined damping for parallel flexures in the x-direction, c_x, can be expressed as:

$$c_{i_x} = 2 \cdot (n_f \cdot \zeta_i) \cdot \sqrt{k_f \cdot m_f} \tag{2}$$

where ζ_i denotes the modal damping of the flexure, and $k_f = k_x/n_f$ and $m_f = m/n_f$ are the stiffness of single flexure and the effective mass perceived by single flexure, respectively.

The non-collocated system dynamics, $G(s) : F_{\text{act}} \mapsto x_2$; is given by the fourth-order transfer function as follows;

$$G(s) = \frac{c_2 s + k_2}{\left(m_2 s^2 + c_2 s + k_2\right)\left[m_1 s^2 + \left(c_1 + c_2\right)s + \left(k_1 + k_2\right)\right] - \left(c_2 s + k_2\right)^2} \tag{3}$$

The transfer functions obtained from both the analytical and numerical models are depicted in Fig.5. The comparison reveals that the analytical model provides a reasonable approximation of the system's behavior. Minor discrepancies can be observed, particularly in the first resonance peak frequency. These deviations can be attributed to the omission of the added mass resulting from the presence of the piezoelectric patches in the analytical model. The results indicate that the inclusion of lightweight piezoelectric patches has minimal impact on the system dynamics. On the other hand, the numerical model effectively captures the higher-order modes that emerge at relatively higher frequencies.

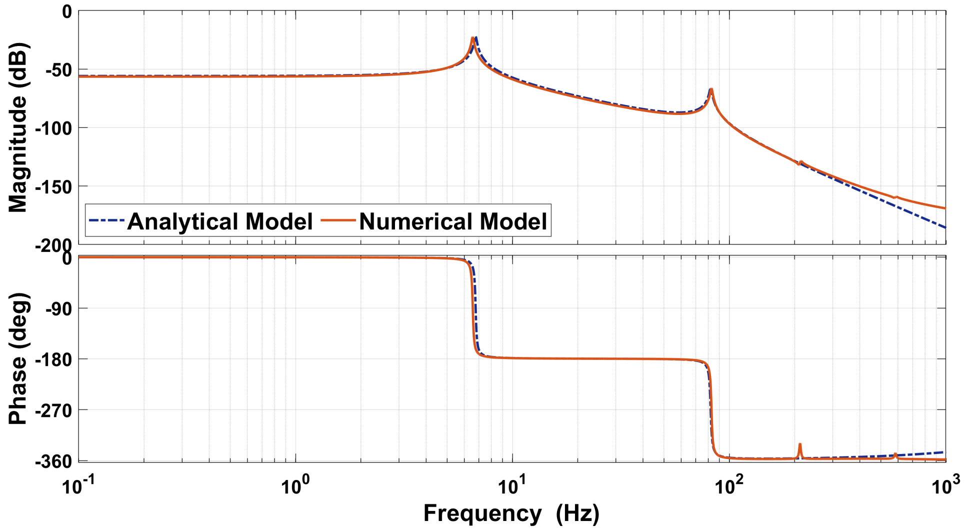

Fig. 5: Comparison of Frequency Response obtained from Analytical and Numerical Model

The results depicted in Fig.5 demonstrate that the system, characterized by a non-collocated actuator and sensor configuration and the presence of undesired resonance modes, exhibits non-minimum phase behavior. This non-minimum phase behavior imposes limitations on the operational bandwidth of the system.

Additionally, the non-collocated plant, denoted as $G(s) = f(c_2)$, is influenced by the parasitic resonance peak height, which is approximately equal to $1/(2\zeta_2)$. According to Eq.(3), an increase in the modal damping coefficient of the connecting flexures (ζ_2) corresponds to a decrease in the peak height in the frequency domain. To address this issue and mitigate the undesired effects of the non-minimum phase behavior, active damping control techniques are introduced and discussed in the subsequent subsection. By implementing active damping control, it becomes possible to enhance the system's damping characteristics and effectively reduce the peak height associated with the undesired resonance mode.

C. Active Flexures with Collocated Piezoelectric Transducers

Piezoelectric bender sensors and actuator patches are strategically placed in a collocated configuration on the flexure to counteract the undesired movement of the end-effector platform caused by the presence of parasitic resonance in the system. When the flexure undergoes transverse displacement $w(x)$ due to the relative displacement $x_d(:= x_2 - x_1)$ of the end-effector platform and base stage, it induces strain distribution in the flexure, including the sensor patch bonded to it. This strain causes a small extension of the patch in the longitudinal direction, which is directly proportional to x_d [48]. The output charge of the sensor is directly proportional to the difference in slopes w' or rotations $\Delta\theta$ at the two extremities (a and b) of the sensor patch.

$$Q \propto \Delta\theta_i^s \propto [w'(b) - w'(a)] \tag{4}$$

As a result, a charge is generated and accumulated across the sensor electrodes, leading to the production of a corresponding sensor voltage signal, V_s. This voltage signal is then fed into the damping controller, which processes it to generate an actuation voltage, V_a. The actuation voltage is applied to the actuator patch electrodes, causing the patch to undergo an extension. This extension generates a counter-torque (M) that opposes the flexure bending at the resonance frequency. The torque magnitude is determined by the equation.

$$M = g_a V_a \tag{5}$$

where g_a is the actuator gain, which can be computed based on the physical characteristics of the actuator. The transfer function between the actuator voltage V_a and the sensor output V_s is thus given as

$$\frac{V_s}{V_a} = g_a g_s \sum_{i=1}^{n} \frac{\Delta\theta_i^a \Delta\theta_i^s}{\mu_i\left(s^2 + 2\xi_i\omega_i s + \omega_i^2\right)} \tag{6}$$

where g_a and g_s are the actuator and sensor gains, ω_i is the natural frequency of mode i, ξ_i the modal damping ratio, and μ_i the modal mass.

The piezoelectric patches are typically positioned at locations on the flexure where the maximum strain is induced by a specific eigenmode that needs to be suppressed [49]. This strategic placement ensures reasonable observability and controllability for the flexure resonance in the collocated channel. By locating the patches at these specific points of maximum strain, they can effectively sense and actuate in response to the undesirable deformation or vibration, allowing for targeted control and mitigation of the eigenmode.

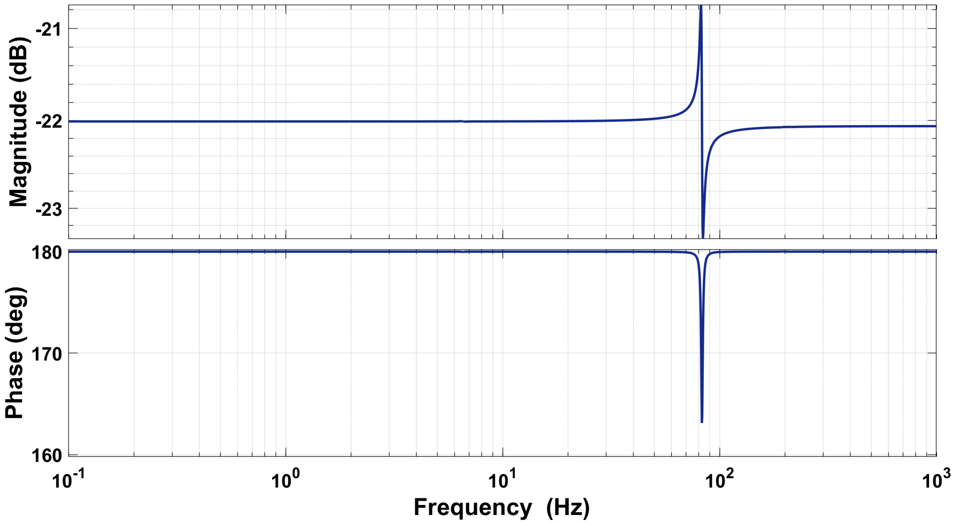

Fig. 6: Frequency Response of Collocated Channel from Piezoelectric Actuator to Sensor ($V_a \mapsto V_s$)

Fig.6 illustrates the typical frequency response of a collocated channel from the piezoelectric actuator to the sensor patch. The collocated configuration results in a frequency response with a pole-zero interlacing pattern.

D. Dynamics of Extended System with Additional Actuators and Sensors

In this subsection, the integration of piezoelectric actuators and sensors is modeled by extending the analytical system presented in subsection III-B. As previously established, the signals from the collocated piezoelectric sensor and actuator are directly proportional to the relative displacement of the end-effector platform. Consequently, the piezoelectric actuator generates a force based on the difference in displacement between the masses m_1 and m_2, exerting equal and opposite forces on both masses. To simplify the analysis, we only consider the flexible dynamics of the system, disregarding the base stiffness (k_1) and damping (c_1). The parallel flexures are modeled as a single equivalent spring (k_2) and damper (c_2). When the piezoelectric transducers are bonded at the same location in all equivalent flexures, they can be considered as a single equivalent sensor-actuator pair. In this configuration, the output force is amplified as the number of collocated patches used for active damping increases. Considering that each flexure integrates one pair, the maximum number of active pair patches for active control (n) can be 4.

The extended system configuration is designed by incorporating additional inputs and outputs to accommodate the operation of the piezoelectric transducers. The extended configuration, denoted as G_{ext}, satisfies the following relationship:

$$\begin{bmatrix} I & 0 \end{bmatrix} G_{\text{ext}}(s) \begin{bmatrix} I \\ 0 \end{bmatrix} = G(s) \tag{7}$$

where $G(s)$ represents the non-collocated dynamics, while $G_{\text{ext}} : \begin{bmatrix} F_{\text{act}} & V_a \end{bmatrix}^T \mapsto \begin{bmatrix} x_2 & V_s \end{bmatrix}^T$. Here, V_a and V_s are the actuation and sensing signal voltage of the piezoelectric transducers placed in a collocated configuration on each of the flexure.

Accordingly, the state-space equations for this extended equivalent system can be expressed as follows:

$$\left\{ \begin{matrix} \ddot{x}_1 \\ \ddot{x}_2 \\ \dot{x}_1 \\ \dot{x}_2 \end{matrix} \right\} = \begin{bmatrix} -\frac{-c_2}{m_1} & \frac{c_2}{m_1} & \frac{-k_2}{m_1} & \frac{k_2}{m_1} \\ \frac{c_2}{m_2} & \frac{-c_2}{m_2} & \frac{k_2}{m_2} & \frac{-k_2}{m_2} \\ 1 & 0 & 0 & 0 \\ 0 & 1 & 0 & 0 \end{bmatrix} \left\{ \begin{matrix} \dot{x}_1 \\ \dot{x}_2 \\ x_1 \\ x_2 \end{matrix} \right\} + \begin{bmatrix} \frac{1}{m_1} & \frac{-n}{m_1} \\ 0 & \frac{n}{m_2} \\ 0 & 0 \\ 0 & 0 \end{bmatrix} \left\{ \begin{matrix} F_{act} \\ V_a \end{matrix} \right\} \tag{8}$$

$$\left\{ \begin{matrix} x_2 \\ V_s \end{matrix} \right\} = \begin{bmatrix} 0 & 0 & 0 & 1 \\ 0 & 0 & p & -p \end{bmatrix} \left\{ \begin{matrix} \dot{x}_1 \\ \dot{x}_2 \\ x_1 \\ x_2 \end{matrix} \right\} + \begin{bmatrix} 0 & 0 \\ 0 & f_d \end{bmatrix} \left\{ \begin{matrix} F_{act} \\ V_a \end{matrix} \right\} \tag{9}$$

Consequently, the input-output relations can be represented as:

$$\left\{ \begin{matrix} x_2 \\ V_s \end{matrix} \right\} = \underbrace{\begin{bmatrix} G_{11} & G_{12} \\ G_{21} & G_{22} \end{bmatrix}}_{G_{\text{ext}}(s)} \left\{ \begin{matrix} F_{act} \\ V_a \end{matrix} \right\} \tag{10}$$

The simplified Multiple-Input Multiple-Output (MIMO) transfer function matrix $G_{\text{ext}}(s)$ is obtained as follows:

$$G_{\text{ext}}(s) = \begin{bmatrix} \frac{c_2 s + k_2}{m_1 m_2 s^2 (s^2 + 2\zeta_n \omega_n s + \omega_n^2)} & \frac{n}{m_2 (s^2 + 2\zeta_n \omega_n s + \omega_n^2)} \\ \frac{p}{m_1 (s^2 + 2\zeta_n \omega_n s + \omega_n^2)} & \frac{-n \cdot p}{m_c (s^2 + 2\zeta_n \omega_n s + \omega_n^2)} + f_d \end{bmatrix} \tag{11}$$

It should be noted that these equations are simplified by neglecting rigid body dynamics. This simplification allows for the presentation of the system dynamics primarily in the interested frequency range ($\omega > \omega_r$, where ω_r is the rigid body mode frequency), which mainly includes the parasitic resonance mode.

IV. OVERACTUATION FOR FLEXIBLE MODE CONTROL

A. *Control Architecture with Additional Actuators and Sensors*

An extended non-collocated system is synthesized by incorporating additional piezoelectric actuator and sensor pairs for the purpose of active damping control. In order to illustrate the interactions between motion tracking control and active damping control, a combined control architecture is presented in Fig.7.

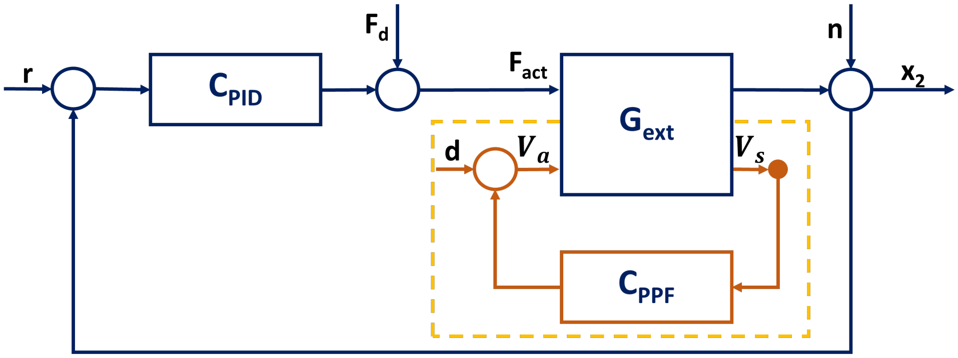

Fig. 7: Control Architecture implementing Active Damping Control

The control architecture consists of two distinct loops: (1) the outer-feedback loop utilizing a standard PID controller C_{PID} to achieve accurate motion tracking, and (2) the inner-feedback loop employing a PPF controller C_{PPF} to address the damping requirements of the system.

1) Tamed PID Controller: A conventional tamed Proportional-Integral-Derivative (PID) controller is employed as the motion-tracking controller in the system. The PID controller operates based on the error signal, which is calculated as the difference between the desired reference set point and the measured position output. The transfer function of linear PID in series form is given by:

$$C_{\text{PID}}(s) = k_p \underbrace{\left(1 + \frac{\omega_i}{s}\right)}_{\text{Integrator}} \underbrace{\left(\frac{s}{\omega_d} + 1\right)}_{\text{Lead}} \underbrace{\left(\frac{s}{\omega_t} + 1\right)^{-1}}_{\text{Lag}} \underbrace{\left(\frac{\omega_l}{s + \omega_l}\right)}_{\text{Low-Pass}} \tag{12}$$

where ω_i is the frequency at which integral action is disabled, ω_l is the cutoff frequency of the low-pass filter (LPF), k_p represents the proportional gain, ω_d indicates the frequency at which differentiating action is initiated, and ω_t represents the frequency at which differentiating action is tamed. The taming is done to prevent amplification of high-frequency noises, while the LPF ensures attenuation of high-frequency noise and unmodelled higher-order system dynamics.

To tune the PID controller, with bandwidth frequency ω_c, the following rules of thumb are used [50]:

$$\begin{aligned} \omega_d &= \omega_c/3; \\ \omega_t &= 3\omega_c; \\ \omega_i &= \omega_c/10; \\ \omega_l &\geq 10\omega_c; \\ k_p &= \frac{1}{3}\left|\frac{1}{G_{11}(i\omega)}\right|_{\omega_c} \end{aligned} \tag{13}$$

These tuning rules are employed to ensure sufficient robustness against instability in the closed-loop feedback control of the motion system. The controller design requirements aim to maintain stability and robustness against phase lag. To achieve this, the gain margin (GM) and phase margin (PM) are evaluated to meet specific conditions:

$$\begin{aligned} \text{GM} &\geq 6\text{dB}; \\ \text{PM} &\geq 30^\circ; \end{aligned} \tag{14}$$

2) PPF Controller: The controller operates on the collocated channel, utilizing the voltage signal obtained from the piezoelectric sensor. This voltage signal is directly proportional to the strain induced in the flexures. The controller processes this input and generates an output voltage signal that is fed to the piezoelectric actuator. The actuator then generates counter-bending moments to actively suppress the undesired vibrations at the specific target frequency. The controller is represented as a second-order low-pass filter [51], given as:

$$C_{\text{PPF}} = g_0^{-1} \frac{g\omega_c^2}{s^2 + 2\zeta_c\omega_c s + \omega_c^2} \tag{15}$$

where ω_c is the corner frequency of the controller, ζ_c is the controller damping, g is the controller gain, and g_0^{-1} is the inverse of the steady state gain of the respective collocated channel frequency response.

B. Exploiting Overactuation: Enhancing Disturbance Rejection with Active Damping Control

To demonstrate the advantages of implementing active damping control with additional actuators on the closed-loop disturbance rejection performance, a comparison is made with a standard control architecture using a conventional notch filter (N), as depicted in Fig.8. The evaluation of this performance involves comparing the closed-loop process sensitivity function ($F_d \mapsto x_2$).

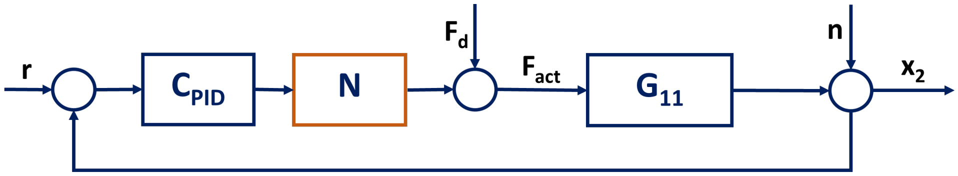

Fig. 8: Control Architecture implementing Notch Filter

1) Case I: Closed-Loop Process Sensitivity implementing Active Damping Control: In the inner closed-loop for active damping control with the damping controller C_{PPF}, depicted in Fig.7, the damped system G_d from actuator force F_{act} to position output x_2 is given as:

$$\begin{aligned} \frac{x_2}{F_{act}} &= G_{11} - G_{12} \cdot \frac{C_{\text{PPF}}}{1 + G_{22} \cdot C_{\text{PPF}}} \cdot G_{21} \\ G_d &= G_{11} \underbrace{\left(1 - \frac{1}{G_{11}} \cdot G_{12} \cdot \frac{C_{\text{PPF}}}{1 + G_{22} \cdot C_{\text{PPF}}} \cdot G_{21}\right)}_{T} \end{aligned} \tag{16}$$

The closed-loop process sensitivity implementing active damping control, PS_{ADC} can be computed as:

$$PS_{\text{ADC}} = \frac{G_d}{1 + G_d \cdot C_{\text{PID}}} \tag{17}$$

where G_d represents the non-collocated performance channel dynamics in the inner closed-loop system.

2) Case 2: Closed-Loop Process Sensitivity implementing Notch Filter: In this case, the closed-loop process sensitivity implementing notch filter (N), PS_{N} is computed as:

$$PS_{\text{N}} = \frac{G_{11}}{1 + G_{11} \cdot C_{\text{PID}} \cdot N} \tag{18}$$

In practice, the damping controller and the notch filter can be independently tuned to achieve a comparable suppression of the parasitic resonance mode in the open loop (i.e., $G_d = G_{11} \cdot N$). Consequently, the denominators of closed-loop Eq.(17) and Eq.(18) at the parasitic resonance mode frequency will be equal.

Therefore, the ratio of the closed-loop process sensitivity in both cases can be expressed as follows:

$$\frac{PS_{\text{ADC}}}{PS_{\text{N}}} = \frac{G_d}{G_{11}} = T < 1 \tag{19}$$

Thus, Eq.(19) demonstrates that when active damping control is employed using overactuation, the magnitude of the closed-loop process sensitivity is reduced, indicating better disturbance rejection performance in the presence of external disturbances, which is not achieved when using a notch filter. This is illustrated in the frequency response of the closed-loop process sensitivity when both control architectures are compared, as shown in Fig.9.

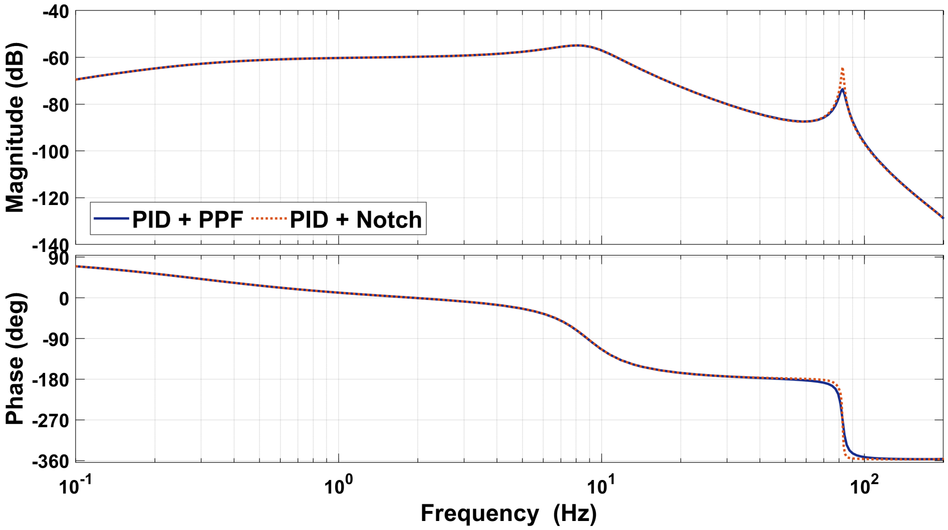

Fig. 9: Comparison of Closed-Loop Process Sensitivity Frequency Response

C. Amplifying Damping Performance: The Impact of Additional Distributed Actuators

In this subsection, a mathematical analysis is performed to demonstrate the advantages of the number of additional actuators employed to suppress the parasitic resonance peak. The analysis initially focuses on a SISO damping control loop, where a collocated channel is utilized with a single PPF controller. A generalized set of equations is employed to establish this mathematically [53].

Each connecting flexure in the setup is modeled as a single-degree-of-freedom system. This simplification is sufficient for analyzing the primary resonance of the flexures, which is the main focus of the analysis. The steady-state response is of particular interest, as the analysis aims to understand the system's response to external disturbances that persist in the steady state. In the modal domain, the equations of motion for the collocated system and the PPF compensator can be expressed as follows:

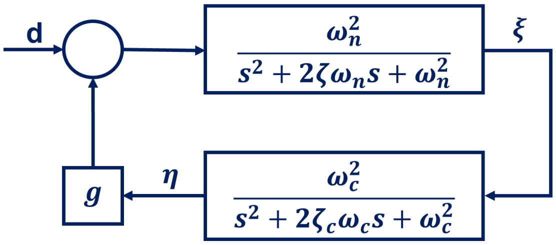

Fig. 10: Closed-Loop Collocated Channel $V_a \mapsto V_s$ with PPF Controller C_{PPF}

$$\ddot{\xi} + 2\zeta\omega_n\dot{\xi} + \omega_n^2\xi = g\omega_n^2\eta + \omega_n^2 d \tag{20}$$

$$\ddot{\eta} + 2\zeta_c\omega_c^2\dot{\eta} + \omega_c^2\eta = \omega_c^2\xi \tag{21}$$

In the given equations, ξ represents the modal coordinate corresponding to the displacement of the structure, ζ represents the damping ratio of the structure, and ω_n represents the natural frequency of the structure. The variable g denotes the feedback gain. On the other hand, η represents the compensator coordinate, ζ_c represents the damping ratio of the compensator, and ω_c represents the frequency of the compensator. The closed-loop disturbance signal is represented as d. It is important to note that for the closed-loop system to be stable, the feedback gain g should be within the range of 0 to 1 [52].

Combining Eq.(20) and Eq.(21) into a matrix form and applying Laplace transformation;

$$\begin{bmatrix} s^2 + 2\zeta\omega_n s + \omega_n^2 & -g\omega_n^2 \\ -g\omega_c^2 & s^2 + 2\zeta_c\omega_c s + \omega_c^2 \end{bmatrix} \begin{Bmatrix} \xi(s) \\ \eta(s) \end{Bmatrix} = \begin{Bmatrix} \omega_n^2 D(s) \\ 0 \end{Bmatrix} \tag{22}$$

Previous studies have shown that the amplitude of the closed-loop transfer function from the disturbance input to the position output, specifically at the resonance frequency, is determined by the following expression when the PPF controller is tuned to the same frequency [53]:

$$\left|\frac{\xi(\omega)}{D(\omega)}\right| = \frac{1}{2\left(\zeta + \frac{g^2}{4\zeta_c}\right)} \tag{23}$$

Expressing the damping factor of the closed-loop system by the PPF controller in terms of the relationship between the amplitude at resonance and the damping factor;

$$\zeta_{i_{CL}} = \zeta_i + \frac{g^2}{4\zeta_c} \tag{24}$$

Therefore, in the case of a SISO feedback loop for active damping, the damping ratio experiences an increase. This increase in the damping ratio corresponds to an increase in the damping ratio of a single flexure ($\zeta_{i_{CL}}$) in the described system when the active damping control loop is activated. The maximum increase is observed when the compensator frequency ω_c matches the structure frequency ω, and the maximum unity gain ($g = 1$) is achieved in a stable closed-loop system. As a result, the limitation on the maximum gain for stability imposes a constraint on the maximum increase in the flexure's damping ratio. This is where overactuation proves advantageous by allowing additional feedback connections to exert a more significant influence on the overall damping ratio of the parallel flexures. When the piezoelectric sensor-actuator pairs are bonded to each flexure, a MIMO system is established, involving n possible active damping feedback loops. Utilizing Eq.(2) and Eq.(24), it can be demonstrated that the total damping coefficient of the parallel flexures in the closed loop is given by:

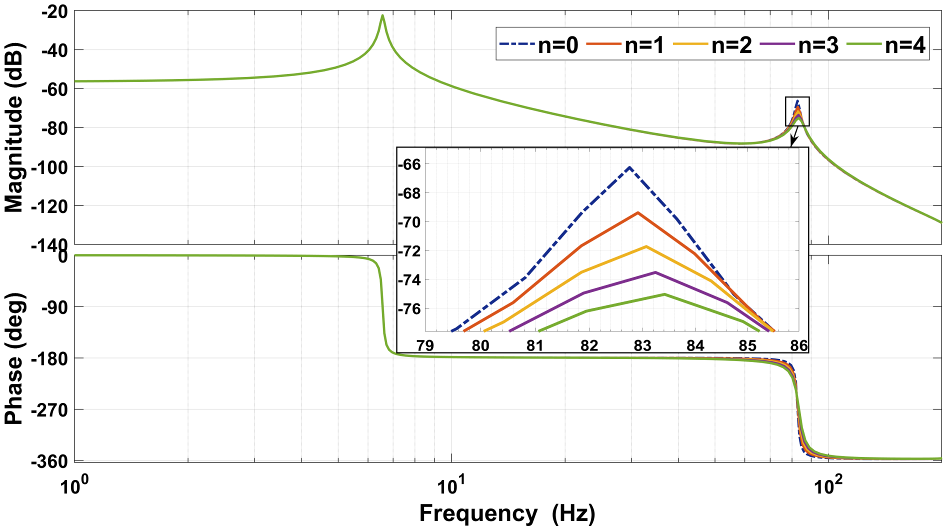

Fig. 11: Impact of Number of Active Piezoelectric Patches on Damping Magnitude in Performance Channel Simulated Numerically in SPACAR

$$\zeta_{CL} = n_f \cdot \zeta_i + \underbrace{n \cdot \frac{g^2}{4\zeta_c}}_{\substack{\text{Increased}\\ \text{Damping Ratio}}} \tag{25}$$

In the context of the system studied in this paper, the parameter n, representing the number of active collocated piezoelectric actuator-sensor pairs, varies within the range of $0 < n < 4$. The impact of increasing the number of active patch pairs on the damping performance in the performance channel is demonstrated through numerical simulations in SPACAR. The system is analyzed in an outer-open-loop configuration, and the results are presented in Fig.11. The plot clearly illustrates that as the number of active patches increases, there is a noticeable enhancement in damping for the parasitic resonance mode.

As observed, it is desired to activate all the piezoelectric transducer patches on all the flexures ($n_f = n$) to maximize the system's performance. Ideally, achieving the maximum performance involves designing the system with a higher number of thinner and narrow parallel flexures, which would provide the desired

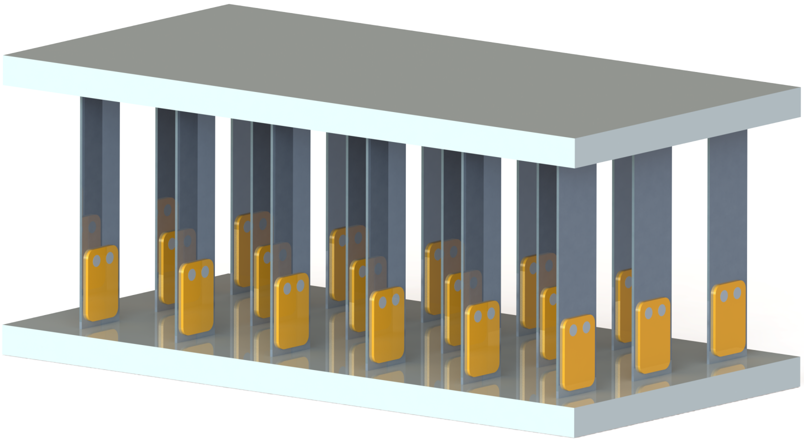

Fig. 12: Illustration of an Ideal Overactuated System to Maximize Damping Performance

stiffness and enable an equivalent number of feedback connections using bonded piezoelectric transducers for active damping, as depicted in Fig.12. However, such an approach would significantly increase the system's complexity and necessitate actuator-sensor patches of much smaller size. The smaller patches might not generate sufficient control force, as the actuator's performance heavily depends on its size parameters. Therefore, there is a trade-off between maximizing the system's performance and managing the practical limitations related to the size and complexity of the components.

Thus, for the practical design implementation of such a system, the number of parallel flexures with bonded collocated piezoelectric transducers that meet the stiffness requirements should be computed based on the desired damping in the closed-loop system. The required number of active piezoelectric patches can be calculated by rearranging Eq.(25) for the desired case ($n_f = n$), resulting in the following expression:

$$n = \frac{\zeta_d}{\zeta_s + \frac{g^2}{4\zeta_c}} \tag{26}$$

where ζ_d is the desired damping in the closed-loop system, ζ_s represents the structure damping, and g and ζ_c are the parameters of the tuned damping controller.

D. Controller Tuning for Active Damping

The PPF controller employed for active damping involves three main parameters that require tuning: the controller gain g, the tuning frequency ω_c, and the controller damping ζ_c. A damping factor of 0.3 is chosen based on literature evidence, as it has been shown to provide a relatively wide frequency range that can be controlled while ensuring satisfactory performance [54]. To tune the remaining two parameters, a cost function is formulated, considering the reduction in the magnitude of the parasitic resonance peak in the inner closed-loop system $G_d(s)$ and the phase lag introduced in the performance channel $F_{act} \mapsto x_2$ around the desired frequency. Additionally, the cost function incorporates stability constraints ($g < 1$) and no-performance constraints ($g > 0$) through the use of the Kreisselmeier-Steinhauser (KS) function to penalize the constraint violation [55]. Different weights are assigned to each objective, resulting in a weighted multi-objective function J, expressed as:

$$J = w_0 \cdot \underbrace{\left|G_d\left(i\omega_n\right)\right|}_{\text{Peak Magnitude}} + \sum_{j=1}^{2} w_j \cdot \underbrace{\left|\angle G_d\left(i\alpha_j\omega_n\right) - \angle G\left(i\alpha_j\omega_n\right)\right|}_{\text{Phase Lag due to Active Damping}} + w_3 \cdot \underbrace{\frac{1}{P}\ln\sum_{k=1}^{2} e^{P\cdot g_k}}_{\text{Penalized Constraints}} \tag{27}$$

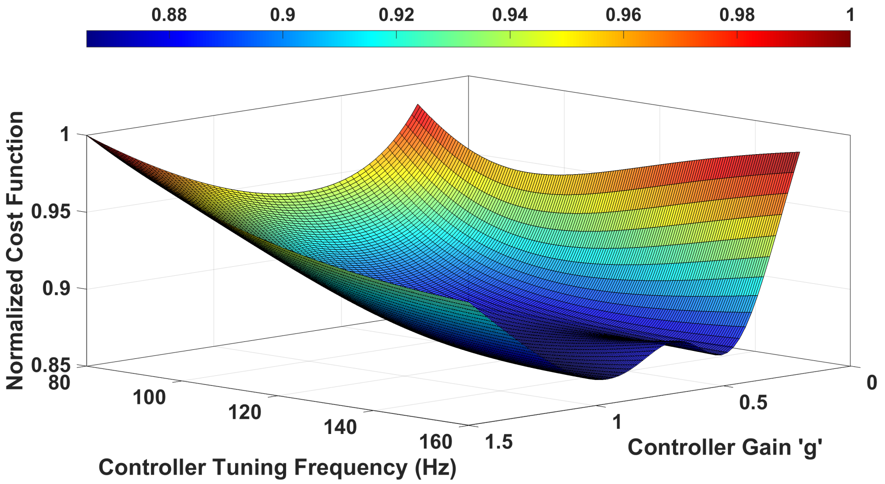

Fig. 13: Parameter Sweep for PPF Controller Tuning

In the provided equation, w_0, w_1, w_2 and w_3 represent the assigned weights, and P denotes the penalty cost. The constraints are denoted by g_k, while $\alpha_1 = 0.97$ and $\alpha_2 = 1.03$ are factors used to calculate the phase around the natural frequency.

Using the formulated cost function, a parameter sweep is conducted to analyze the impact of the controller tuning frequency ω_c, and the controller gains g on the cost function. The normalized cost function is depicted in Fig.13. Based on the results of this parameter sweep, a controller gain of 0.7 and a targeted frequency of 120 Hz were selected.

V. EXPERIMENTAL RESULTS AND DISCUSSION

A. *System Identification*

To identify the system, a variable frequency sinusoidal signal with a small amplitude is generated using LabVIEW and sent to the actuators in the system. The position output from the interferometer is measured, and the time-based input-output signals are then imported into MATLAB for further analysis. The signal processing toolbox in MATLAB is utilized to estimate the transfer functions of the MIMO system.

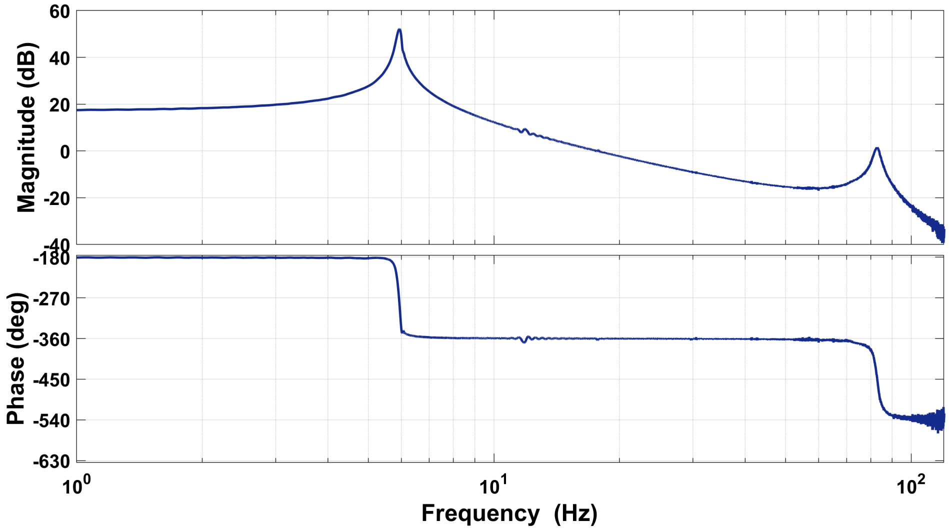

Fig. 14: Experimentally Identified Frequency Response of Performance Channel $F_{\text{act}} \mapsto x_2$

The sampling frequency of the signals is set at 10 kHz to capture sufficient data for accurate identification. The identified model obtained from the signal processing analysis is compared to the numerical model of the system. The resonance frequencies of the identified model closely match those of the numerical model, indicating a good agreement. However, it's important to note that the gains of the identified model differ from the numerical model due to the inclusion of actuator and amplifier dynamics during the identification process.

B. *Dampening System using Overactuation*

To illustrate the effects of overactuation through experimentation, an inner-feedback loop incorporating a feedback controller is utilized to mitigate the inherent characteristics of the open-loop plant. The damping performance is investigated as the number of active piezoelectric actuator-sensor patch pairs (n) varies. The outcomes validate that activating additional feedback connections results in an intensified damping effect on the parasitic resonance mode. Notably, when all loops are active, a substantial reduction of 7.2 dB is observed in the peak magnitude within the frequency domain, as depicted in Fig.15. Tuning the damping controller at a frequency higher than the resonance frequency results in a slight decrease in stiffness, evident by a slightly lower closed-loop resonance frequency.

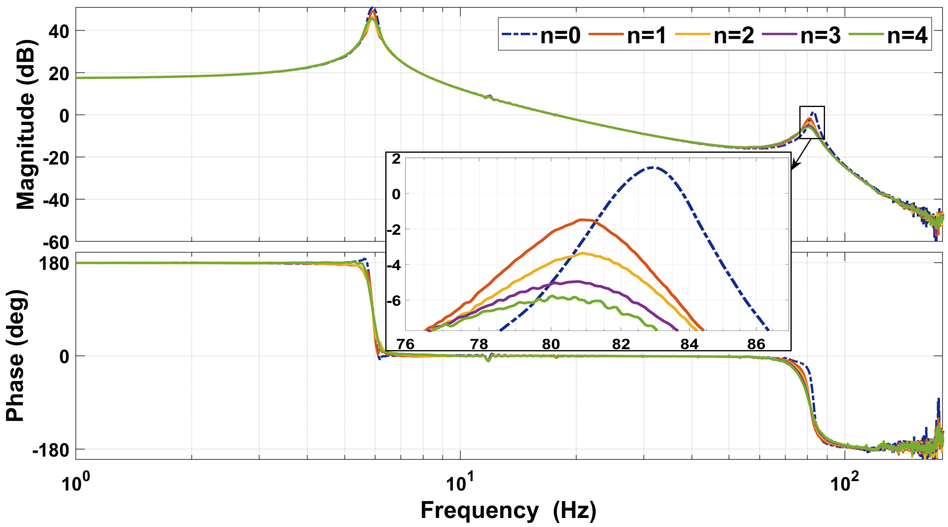

Fig. 15: Impact of Number of Active Piezoelectric Patches on Damping Magnitude in Performance Channel Observed Experimentally

TABLE I: Comparison of Numerical and Experimental Resonance Peak Reduction with Different Numbers of Active Piezoelectric Actuators

Number of Active Piezoelectric Actuators (n)	Reduction in Resonance Peak Magnitude	
	Numerical	Experimental
1	3.1 dB	2.95 dB
2	2.3 dB	1.85 dB
3	1.8 dB	1.6 dB
4	1.5 dB	0.8 dB

Table I provides a comparison of the damping performance achieved numerically and experimentally. The observed difference in absolute magnitude reductions of the resonance mode between the experimental and numerical studies can be attributed to the non-uniform and imperfect bonding layer between the piezoelectric transducer and the flexure in the real setup. This bonding layer, not accounted for in the

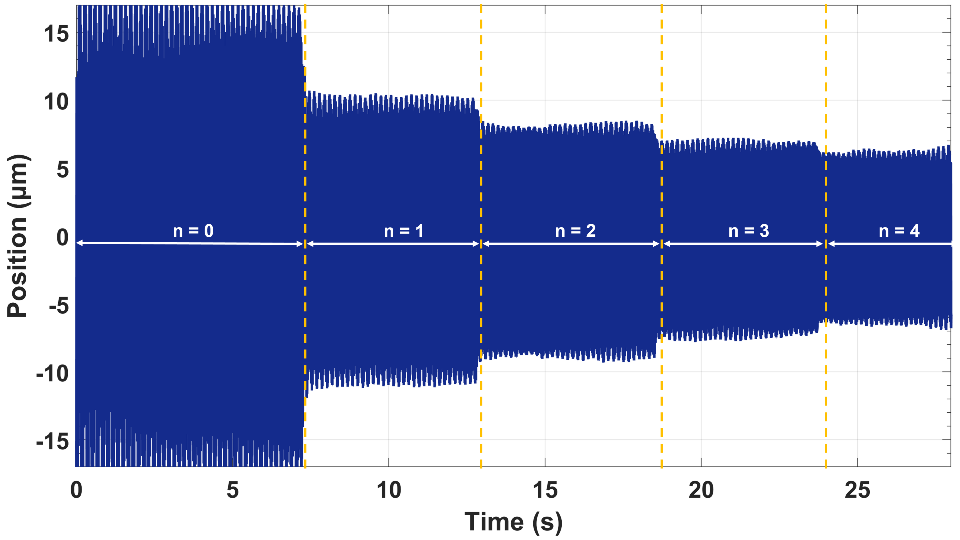

Fig. 16: Experimental Illustration of Impact of Number of Active Piezoelectric Patches on Position Accuracy in Time Domain

numerical model, affects the electromechanical coupling coefficient, which represents the efficiency of mechanical to electrical energy conversion or vice versa, and consequently impacts the dynamics of the system [56]–[58]. As a result, the achieved damping performance shows variations between the numerical simulations and the experimental results.

To gain a more comprehensive understanding of the system's response to disturbances, an analysis in the time domain is conducted by applying a disturbance signal with a frequency of 82 Hz, corresponding to the parasitic resonance frequency, to the outer open-loop system and the resultant position output is measured. Consistent with the earlier findings, it is apparent from Fig.16 that activating more feedback loops leads to a decrease in the magnitude of fluctuations in the output position.

C. Closed-Loop Disturbance Rejection Performance

To assess the performance of the closed-loop system, the outer motion tracking loop is closed by implementing a PID controller based on the tuning rules presented in Eq.(13) to meet the design requirements given in Eq.(14). The controllers are implemented in real-time by discretizing the continuous-time controller using the bilinear transformation-based Tustin method.

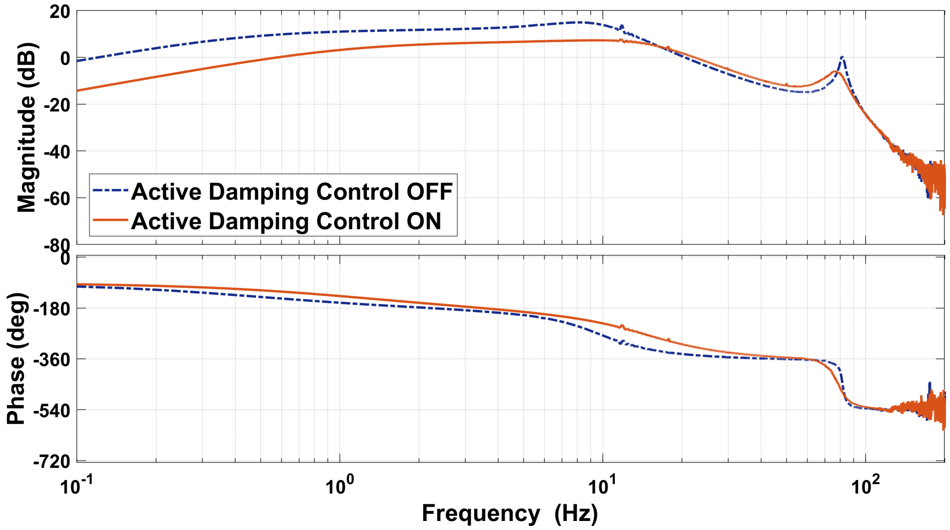

Fig. 17: Closed-Loop Experimental Process Sensitivity Frequency Response

To analyze the main objective of the study, which is to improve disturbance rejection performance through the use of damping control for the parasitic flexible dynamics, the frequency response of the closed-loop process sensitivity is measured in two cases: without active damping control and with damping control, where all inner-feedback loops are active. As depicted in Fig.17, the peak height of the resonance is suppressed by approximately 6.5 dB, indicating a significant improvement in the system's ability to reject disturbances caused by external forces and an enhanced position accuracy of the end-effector platform.

D. Closed-Loop Control Bandwidth

Through overactuation, the parasitic resonance mode is mitigated, enabling the utilization of higher control bandwidths to enhance motion control. The implementation of a controller with higher bandwidth is conducted in closed-loop experiments using AVC. The results validate an increase in control bandwidth, represented by the crossover frequency at -3dB, which improves from 17Hz to 32Hz in the closed-loop complementary sensitivity function as depicted in Fig.18. This enhanced bandwidth, which is approximately 1.5 times wider, along with the reduction in vibrations, contributes to enhanced tracking performance of the end-effector platform.

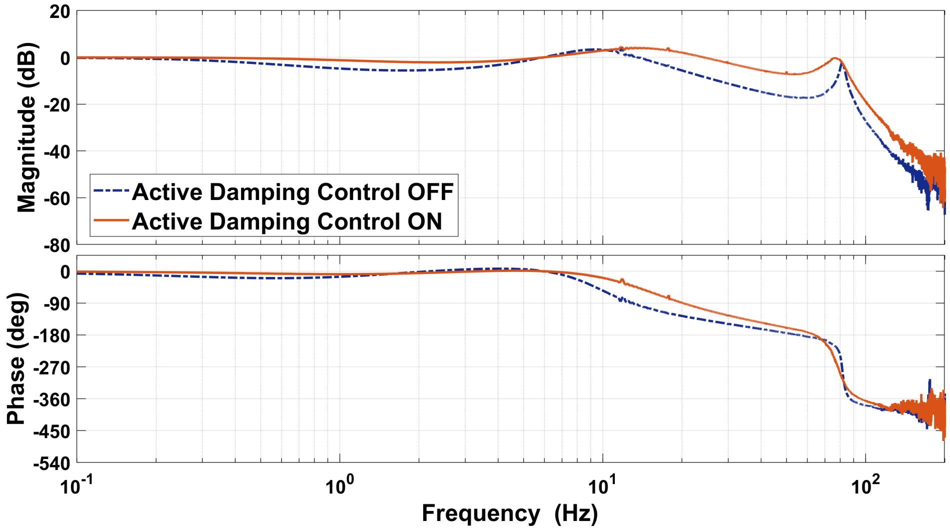

Fig. 18: Closed-Loop Experimental Complementary Sensitivity Frequency Response

E. *Tracking Performance*

The primary objective of a positioning stage is to accurately adhere to a predefined trajectory. To assess the impact of active damping control on the stage's motion performance, a finite step input is applied to the system.

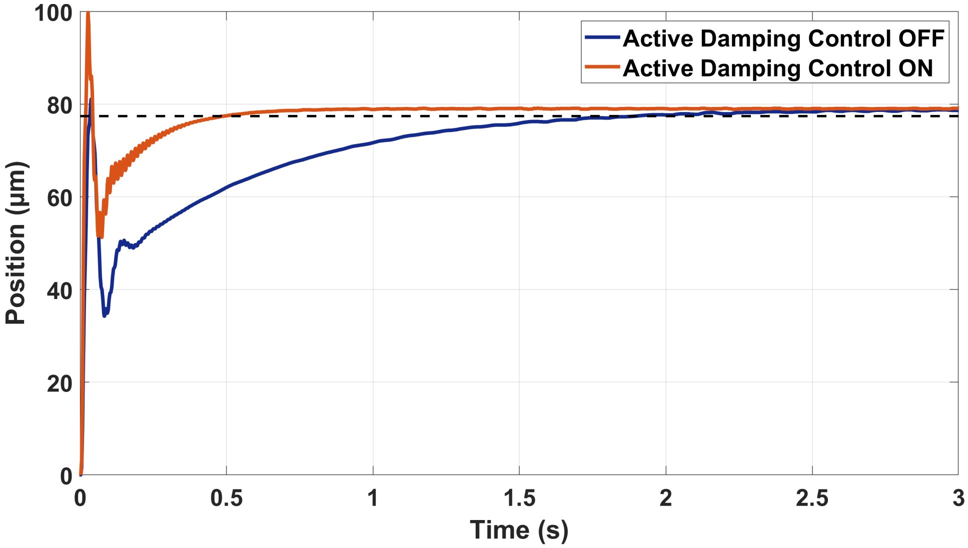

Fig. 19: Experimental Tracking Response to Step Reference

The step tracking performance, illustrated in Fig.19, clearly demonstrates that the integration of active damping control with a motion tracking controller effectively decreases the settling time by 74%. This improvement can be attributed to the utilization of a higher control bandwidth, made possible by the reduction of parasitic resonance peak while maintaining stability margins.

VI. CONCLUSIONS

In conclusion, the presented research introduces a novel overactuation-based strategy to enhance the disturbance rejection and motion-tracking performance of compliant positioning stages. The method involves utilizing lightweight piezoelectric actuator-sensor patches strategically bonded to flexures in a collocated configuration at locations of maximum strain to enable overactuation. By implementing active damping control through additional distributed piezoelectric transducers in a collocated configuration, the proposed method effectively dampens parasitic vibrations and external disturbances that affect the position accuracy of the end-effector, overcoming the limitations of traditional notch filters. Increasing the number of active actuators enhances the damping performance, resulting in greater suppression of the targeted resonance peak. By mitigating flexible dynamics, the proposed strategy allows for a higher control bandwidth, leading to improved closed-loop motion-tracking performance. A mathematical framework was developed to generalize the contributions of this work, and a numerical model in SPACAR was created to simulate the proposed method's performance. To validate the findings, an experimental setup was constructed using a dual-stage compliant positioning system as a proof-of-concept, and the numerical results were verified experimentally.

Moving forward, future research can focus on optimizing control strategies within the overactuation framework to further enhance system performance. Exploring different actuator-sensor configurations will expand the application of overactuation to diverse systems and industries. The scalability and adaptability of overactuated systems also present exciting prospects for further advancements in positioning system technology.

REFERENCES

[1] Ryu, Jae W., Dae-Gab Gweon, and Kee S. Moon. "Optimal design of a flexure hinge based XYϕ wafer stage." Precision engineering 21, no. 1 (1997): 18-28.

[2] Devasia, Santosh, Evangelos Eleftheriou, and SO Reza Moheimani. "A survey of control issues in nanopositioning." IEEE Transactions on Control Systems Technology 15, no. 5 (2007): 802-823.

[3] Yong, Y. K., SO Reza Moheimani, B. J Kenton, and K. K. Leang. "Invited review article: High-speed flexure-guided nanopositioning: Mechanical design and control issues." Review of scientific instruments 83, no. 12 (2012): 121101.

[4] Ku, Sang-Soon, Unnat Pinsopon, Sabri Cetinkunt, and Shin-ichi Nakajima. "Design, fabrication, and real-time neural network control of a three-degrees-of-freedom nanopositioner." IEEE/ASME transactions on mechatronics 5, no. 3 (2000): 273-280.

[5] Yi, Byung-Ju, Goo Bong Chung, Heung Yeol Na, Whee Kuk Kim, and Il Hong Suh. "Design and experiment of a 3-DOF parallel micromechanism utilizing flexure hinges." IEEE Transactions on robotics and automation 19, no. 4 (2003): 604-612.

[6] Wang, Fujun, Cunman Liang, Yanling Tian, Xingyu Zhao, and Dawei Zhang. "Design of a piezoelectric-actuated microgripper with a three-stage flexure-based amplification." IEEE/ASME Transactions on Mechatronics 20, no. 5 (2014): 2205-2213.

[7] Lu, Tien-Fu, Daniel C. Handley, Yuen Kuan Yong, and Craig Eales. "A three-DOF compliant micromotion stage with flexure hinges." Industrial robot: an international journal 31, no. 4 (2004): 355-361.

[8] Polit, Sebastian, and Jingyan Dong. "Development of a high-bandwidth XY nanopositioning stage for high-rate micro-/nanomanufacturing." IEEE/ASME Transactions on mechatronics 16, no. 4 (2010): 724-733.

[9] Gonda, S., T. Kurosawa, and Y. Tanimura. "Mechanical performances of a symmetrical, monolithic three-dimensional fine-motion stage for nanometrology." Measurement Science and Technology 10, no. 11 (1999): 986.

[10] Mazzeo, A. D., A. J. Stein, D. L. Trumper, and R. J. Hocken. "Atomic force microscope for accurate dimensional metrology." Precision engineering 33, no. 2 (2009): 135-149.

[11] Yong, Yuen Kuan, Anthony G. Fowler, Ali Mohammadi, and S. O. R. Moheimani. "Control of a MEMS nanopositioner for atomic force microscopy." IFAC Proceedings Volumes 46, no. 5 (2013): 375-382.

[12] Wang, Piyu, and Qingsong Xu. "Design of a flexure-based constant-force XY precision positioning stage." Mechanism and Machine Theory 108 (2017): 1-13.

[13] Xu, Qingsong. "Design and development of a compact flexure-based XY precision positioning system with centimeter range." IEEE Transactions on Industrial Electronics 61, no. 2 (2013): 893-903.

[14] Ding, Runze, Chenyang Ding, Yunlang Xu, Weike Liu, and Xiaofeng Yang. "An optimal actuator placement method for direct-drive stages to maximize control bandwidth." In IECON 2020 The 46th Annual Conference of the IEEE Industrial Electronics Society, pp. 556-561. IEEE, 2020.

[15] Eielsen, Arnfinn A., Marialena Vagia, J. Tommy Gravdahl, and Kristin Y. Pettersen. "Damping and tracking control schemes for nanopositioning." IEEE/ASME Transactions on Mechatronics 19, no. 2 (2013): 432-444.

[16] Gu, Guo-Ying, Li-Min Zhu, Chun-Yi Su, Han Ding, and Sergej Fatikow. "Modeling and control of piezo-actuated nanopositioning stages: A survey." IEEE Transactions on Automation Science and Engineering 13, no. 1 (2014): 313-332.

[17] Tao, Yidan, Linlin Li, Han-Xiong Li, and LiMin Zhu. "High-bandwidth tracking control of piezoactuated nanopositioning stages via active modal control." IEEE Transactions on Automation Science and Engineering 19, no. 4 (2021): 2998-3006.

[18] Fleming, Andrew J. "Nanopositioning system with force feedback for high-performance tracking and vibration control." IEEE/Asme Transactions on Mechatronics 15, no. 3 (2009): 433-447.

[19] Alkhatib, Rabih, and M. F. Golnaraghi. "Active structural vibration control: a review." Shock and Vibration Digest 35, no. 5 (2003): 367.

[20] Butterworth, Jeffrey A., Lucy Y. Pao, and Daniel Y. Abramovitch. ”Analysis and comparison of three discrete-time feedforward model-inverse control techniques for nonminimum-phase systems.” Mechatronics 22, no. 5 (2012): 577-587.

[21] Iwasaki, Makoto, Kenta Seki, and Yoshihiro Maeda. ”High-precision motion control techniques: A promising approach to improving motion performance.” IEEE Industrial Electronics Magazine 6, no. 1 (2012): 32-40.

[22] Steinbuch, Maarten, and Meindert L. Norg. ”Advanced motion control: An industrial perspective.” European Journal of Control 4, no. 4 (1998): 278-293.

[23] Aphale, Sumeet S., Andrew J. Fleming, and SO Reza Moheimani. ”Integral resonant control of collocated smart structures.” Smart materials and structures 16, no. 2 (2007): 439.

[24] Bhikkaji, B., and SO Reza Moheimani. ”Integral resonant control of a piezoelectric tube actuator for fast nanoscale positioning.” IEEE/ASME Transactions on mechatronics 13, no. 5 (2008): 530-537.

[25] Fleming, Andrew J., and Kam K. Leang. ”Integrated strain and force feedback for high-performance control of piezoelectric actuators.” Sensors and Actuators A: Physical 161, no. 1-2 (2010): 256-265.

[26] Yong, Yuen K., and Andrew J. Fleming. ”High-speed vertical positioning stage with integrated dual-sensor arrangement.” Sensors and Actuators A: Physical 248 (2016): 184-192.

[27] Li, Chun-Xia, Guo-Ying Gu, Mei-Ju Yang, and Li-Min Zhu. ”Positive position feedback based high-speed tracking control of piezo-actuated nanopositioning stages.” In Intelligent Robotics and Applications: 8th International Conference, ICIRA 2015, Portsmouth, UK, August 24-27, 2015, Proceedings, Part II 8, pp. 689-700. Springer International Publishing, 2015.

[28] Fanson, J. L., and T. K. Caughey. ”Positive position feedback control for large space structures.” AIAA journal 28, no. 4 (1990): 717-724.

[29] B. Bhikkaji, M. Ratnam, and S. O. R. Moheimani, “PVPF control of piezoelectric tube scanners,” Sens. Actuators A, Phys., vol. 135, no. 2, pp. 700–712, Jul. 2006.

[30] Li, Linlin, Chun-Xia Li, Guoying Gu, and Li-Min Zhu. ”Positive acceleration, velocity and position feedback based damping control approach for piezo-actuated nanopositioning stages.” Mechatronics 47 (2017): 97-104.

[31] Babarinde, Adedayo K., Li-Min Zhu, and Sumeet S. Aphale. ”Simultaneous design of positive acceleration velocity and position feedback based combined damping and tracking control scheme for nanopositioners.” In 2019 18th European Control Conference (ECC), pp. 608-613. IEEE, 2019.

[32] Babarinde, Adedayo K., Linlin Li, LiMin Zhu, and Sumeet S. Aphale. ”Experimental validation of the simultaneous damping and tracking controller design strategy for high-bandwidth nanopositioning–a PAVPF approach.” IET Control Theory & Applications 14, no. 20 (2020): 3506-3514.

[33] Moheimani, SO Reza, Benjamin JG Vautier, and Bharath Bhikkaji. ”Experimental implementation of extended multivariable PPF control on an active structure.” IEEE Transactions on Control Systems Technology 14, no. 3 (2006): 443-455.

[34] Orszulik, Ryan, and Jinjun Shan. ”Multi-mode adaptive positive position feedback: An experimental study.” In Proceedings of the 2011 American Control Conference, pp. 3315-3319. IEEE, 2011.

[35] Song, G., S. P. Schmidt, and B. N. Agrawal. ”Experimental robustness study of positive position feedback control for active vibration suppression.” Journal of guidance, control, and dynamics 25, no. 1 (2002): 179a-182.

[36] Warminski, Jerzy, Marcin Bochenski, Wojciech Jarzyna, Piotr Filipek, and Michal Augustyniak. ”Active suppression of nonlinear composite beam vibrations by selected control algorithms.” Communications in Nonlinear Science and Numerical Simulation 16, no. 5 (2011): 2237-2248.

[37] Ferrari, Giovanni, and Marco Amabili. ”Active vibration control of a sandwich plate by non-collocated positive position feedback.” Journal of Sound and Vibration 342 (2015): 44-56.

[38] Preumont, André. Vibration control of active structures: an introduction. Vol. 246. Springer, 2018.

[39] Schneiders, M. G. E., M. J. G. Van De Molengraft, and M. Steinbuch. ”Benefits of over-actuation in motion systems.” In Proceedings of the 2004 American control conference, vol. 1, pp. 505-510. IEEE, 2004.

[40] van Herpen, Robbert, Tom Oomen, Edward Kikken, Marc van de Wal, Wouter Aangenent, and Maarten Steinbuch. ”Exploiting additional actuators and sensors for nano-positioning robust motion control.” Mechatronics 24, no. 6 (2014): 619-631.

[41] Classens, Koen, W. P. M. H. Heemels, and Tom Oomen. ”A closed-loop perspective on fault detection for precision motion control: With application to an overactuated system.” In 2021 IEEE International Conference on Mechatronics (ICM), pp. 1-6. IEEE, 2021.

[42] Schneiders, M. G. E., M. J. G. Van De Molengraft, and M. Steinbuch. ”Modal framework for closed-loop analysis of over-actuated motion systems.” Hal Archives 53, no. 7 (2004).

[43] Schneiders, Maurice GE, M. J. G. Van De Molengraft, and Maarten Steinbuch. ”Introduction to an integrated design for motion systems using over-actuation.” In 2003 European Control Conference (ECC), pp. 3249-3254. IEEE, 2003.

[44] Galvan, Saudith Durango, Marcel Heertjes, and Rémy Dunand. ”Plant enhancements in motion systems by modal control.” In 2012 American Control Conference (ACC), pp. 5348-5353. IEEE, 2012.

[45] Seinhorst, B., M. Nijenhuis, and W. B. J. Hakvoort. ”Feasibility of Active Material Vibration Suppression in a Large Stroke Flexure Hinge.” IFAC-papersonline 55, no. 27 (2022): 166-171.

[46] Schmidt, R. Munnig, Georg Schitter, and Adrian Rankers. The design of high performance mechatronics-: high-Tech functionality by multidisciplinary system integration. Ios Press, 2020.

[47] Van Eijk, Jan. On the design of plate-spring mechanisms. Laboratory of Fine Mechanics, 1985.

[48] Moheimani, SO Reza, and Andrew J. Fleming. Piezoelectric transducers for vibration control and damping. Vol. 1. London: Springer, 2006.

[49] Bachmann, Florian, Andrea E. Bergamini, and Paolo Ermanni. ”Optimum piezoelectric patch positioning: A strain energy–based finite element approach.” Journal of intelligent material systems and structures 23, no. 14 (2012): 1575-1591.

[50] Dastjerdi, Ali Ahmadi, Niranjan Saikumar, and S. Hassan HosseinNia. ”Tuning guidelines for fractional order PID controllers: Rules of thumb.” Mechatronics 56 (2018): 26-36.

[51] Preumont, André. Vibration control of active structures: an introduction. Vol. 246. Springer, 2018.

[52] Fanson, J. L., and T. K. Caughey. ”Positive position feedback control for large space structures.” AIAA journal 28, no. 4 (1990): 717-724.
[53] Kwak, Moon-Kyu, Sang-Bo Han, and Seok Heo. ”The stability conditions, performance and design methodology for the positive position feedback controller.” Transactions of the Korean Society for Noise and Vibration Engineering 14, no. 3 (2004): 208-213.
[54] Kwak, Moon Kyu. Dynamic modeling and active vibration control of structures. Berlin/Heidelberg, Germany: Springer, 2022.
[55] Sethi, S., A. Striz, S. Sethi, and A. Striz. ”On using the Kreisselmeier-Steinhauser function in simultaneous analysis and design.” In 38th Structures, Structural Dynamics, and Materials Conference, p. 1289. 1997.
[56] Pietrzakowski, Marek. ”Active damping of beams by piezoelectric system: effects of bonding layer properties.” International Journal of Solids and Structures 38, no. 44-45 (2001): 7885-7897.
[57] Tinoco, Hector A., Alberto L. Serpa, and Angel M. Ramos. ”Numerical study of the effects of bonding layer properties on electrical signatures of piezoelectric sensors.” Mecánica Computacional 29, no. 86 (2010): 8391-8409.
[58] Han, L., X. D. Wang, and Y. Sun. ”The effect of bonding layer properties on the dynamic behaviour of surface-bonded piezoelectric sensors.” International Journal of Solids and Structures 45, no. 21 (2008): 5599-5612.

4 | Results and Discussion

This chapter consolidates the significant findings from the preceding chapter while offering supplementary perspectives and discussions associated with these results. It aims to provide deeper insights into the work, facilitating a comprehensive evaluation that can inspire future advancements in the field.

4.1 Impact of Additional Actuators

To experimentally demonstrate the impact of employing additional actuators, the damping performance is analyzed by observing the dampening of the parasitic resonance peak magnitude in the performance channel $F_{\text{act}} \mapsto x_2$. To achieve this, the outer open-loop system (PID controller inactive) is identified by applying an input signal to the Lorentz actuator and measuring the position output. The investigation of damping performance is carried out while varying the number of active piezoelectric actuator-sensor patch pairs (n). The results validate that activating additional feedback connections leads to a heightened damping effect on the parasitic resonance mode. Notably, when all loops are active, a substantial reduction of 7.2 dB is observed in the peak magnitude within the frequency domain, as depicted in

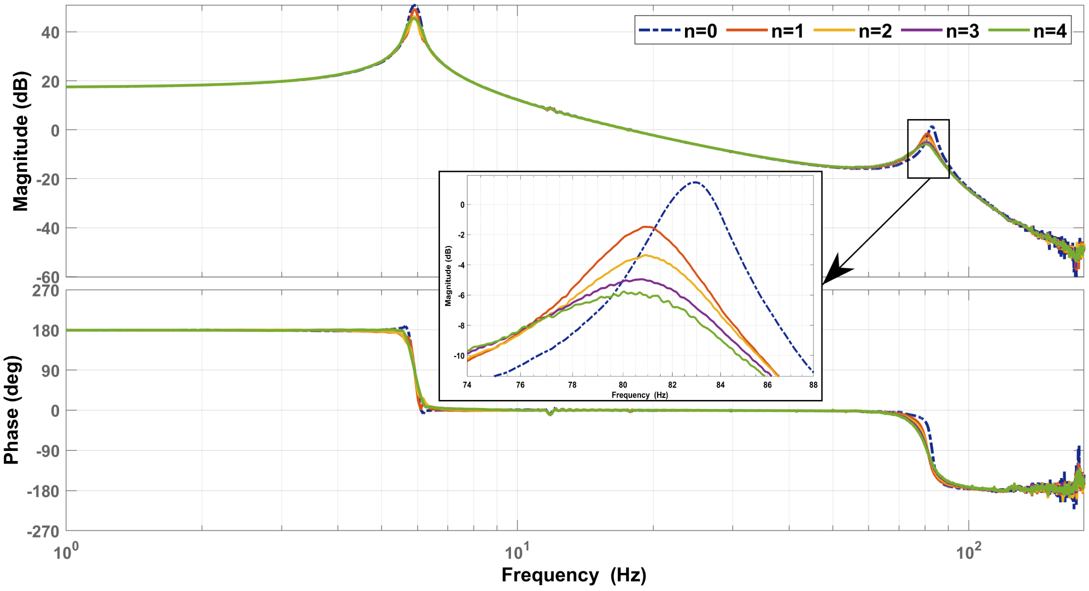

Figure 4.1: Experimental Illustration of Overactuation in Frequency Domain

Fig.4.1. Additionally, tuning the damping controller at a frequency higher than the resonance frequency results in a slight decrease in stiffness, as evidenced by a slightly lower closed-loop resonance frequency.

Fig.4.2 presents the damped peak magnitude as the number of active piezoelectric actuator patches is varied.

Number of Active Piezoelectric Actuators *(n)*	**Parasitic Resonance Peak Magnitude**
0	1.45 dB
1	-1.50 dB
2	-3.35 dB
3	-4.95 dB
4	-5.75 dB

Figure 4.2: Parasitic peak magnitude for different number of active piezoelectric actuators

To gain a more comprehensive understanding of the system's response to disturbances, an analysis in the time domain is conducted by applying a disturbance signal with a frequency of 82 Hz, corresponding to the parasitic resonance frequency, to the outer open-loop system and the resultant position output is measured. Consistent with the earlier findings, it is apparent from Fig.4.3 that activating more feedback loops leads to a decrease in the magnitude of fluctuations in the output position.

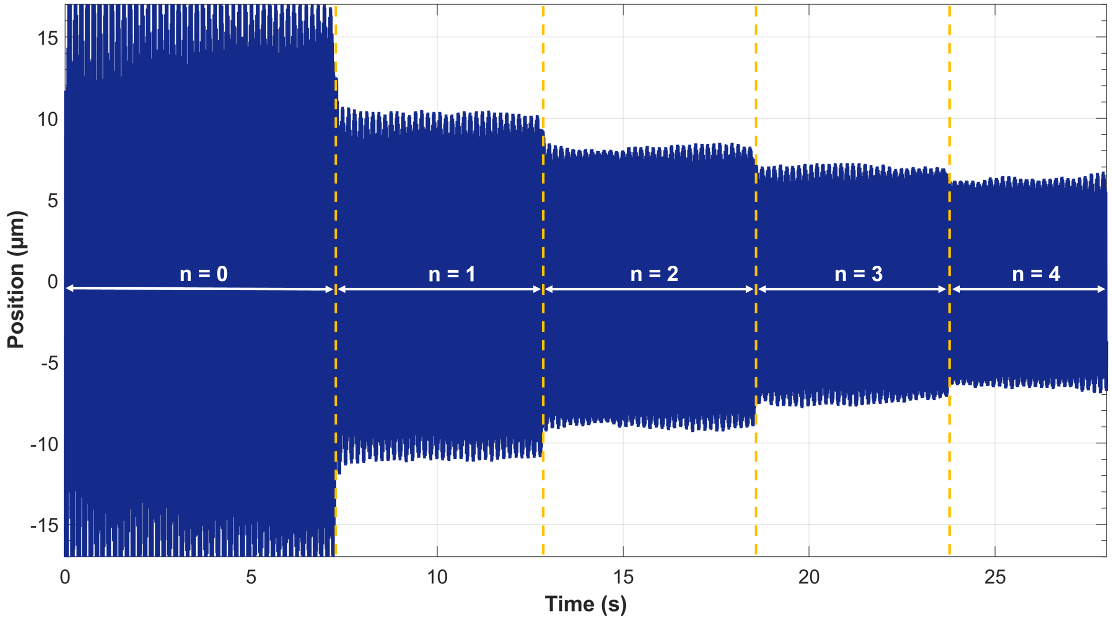

Figure 4.3: Experimental Illustration of Overactuation in Time Domain

The utilization of additional actuators intuitively implies an increase in the total energy consumption within the system. Fig.4.4 illustrates how the actuation voltages of the active piezoelectric patches vary based on the number of active patches. It is evident that when only one actuator patch is active, it is responsible for controlling and counteracting the vibrations induced by the excitation of the parasitic resonance mode on its own. Consequently, this demands more control action, leading to the observation that a single piezoelectric actuator requires the maximum operating voltage. However, as the number of active patches increases, it can be observed that the operating voltages of the already active patches decrease, and the newly active patch also consumes lesser energy. This can be analogously understood as the control action being distributed among the distributed actuators in the closed-loop system for a certain variation in the output position. Ideally, the operating voltages should be equal for all active actuators; however, in the experimental setup, each collocated piezoelectric patch pair has a slightly different frequency response, as illustrated in Appendix C. These variations can be attributed to the presence of a non-uniform and imperfect bonding layer between the piezoelectric transducer and the flexure in the physical setup. The numerical model does not account for this bonding layer, which has a significant impact on the electromechanical coupling coefficient, representing the efficiency of energy conversion between mechanical and electrical domains. As a consequence, the dynamics of the system are influenced, leading to differences in the identified frequency responses and achieved damping performance among the collocated channels [134–136]. Consequently, the controller tuned for each collocated channel has a different gain, leading to the observed difference in the operating voltages of these active actuators.

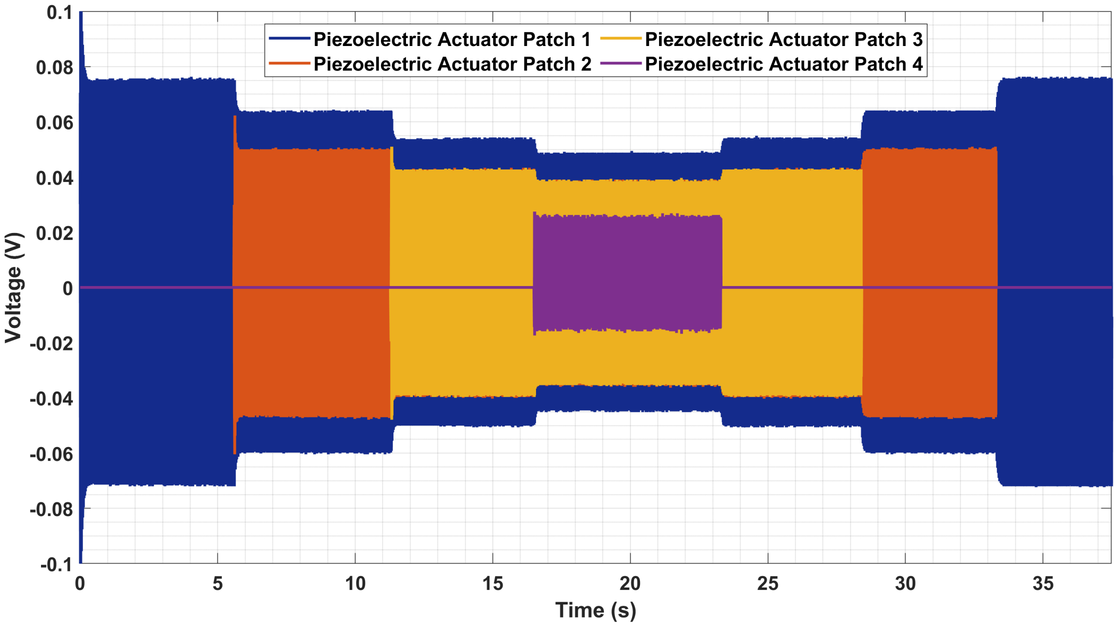

Figure 4.4: Actuation Voltage Signals of Active Piezoelectric Actuators

Furthermore, it is noted that some active patches exhibit sinusoidally varying operating voltage signals with certain offsets. This is attributed to the calibration offset value of the voltage amplifiers, which varies for each amplifier. During the experimental studies, the offset value was calibrated using only one voltage amplifier; however, it is necessary to perform individual calibrations for each amplifier utilized in the setup to eliminate these offsets effectively.

4.2 Closed-Loop Disturbance Rejection

To assess the influence of overactuation on the closed-loop disturbance rejection performance ($F_d \mapsto x_2$) through the use of active damping control for the parasitic flexible dynamics, the inner damping feedback loop is activated by implementing the tuned PPF controllers for each collocated channel, while the outer motion tracking loop is made active by implementing a PID controller based on the PID tuning guidelines presented in Chapter 3, which meets the required stability design requirements. The frequency response of the closed-loop process sensitivity is measured in two cases: without active damping control and with damping control, where all inner-feedback loops are active. As depicted in Fig.4.5, the peak height of the resonance is suppressed by approximately 6.5 dB, indicating a significant improvement in the system's ability to reject disturbances caused by external forces and an enhanced position accuracy of the end-effector platform.

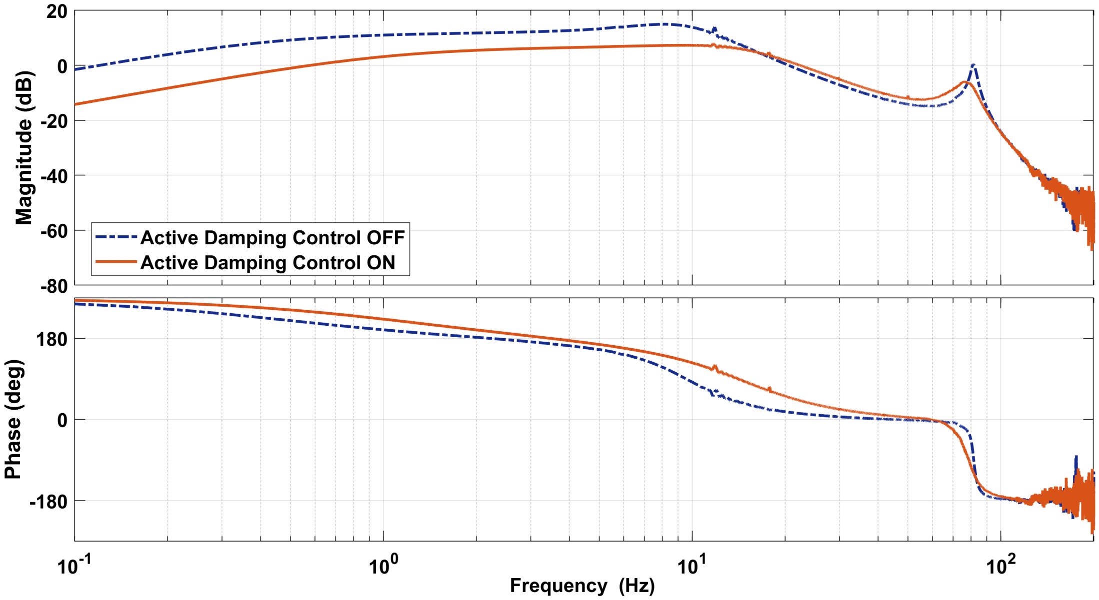

Figure 4.5: Closed-Loop Experimental Process Sensitivity Frequency Response

The low gain of the process sensitivity in the low-frequency regime (frequencies below the control bandwidth) when active damping control is implemented can be attributed to the higher gain of the PID controller tuned for this scenario. Additionally, a slightly higher gain is observed in the presented frequency response in the frequency range after the control bandwidth but before the parasitic resonance mode frequency. This higher gain is attributed to the spillover effect caused in the closed-loop collocated channel due to the high gain of the PPF controllers in that regime. These differences in gains are transmitted to the performance channel through the coupling terms in the MIMO system.

The impact of process disturbance rejection performance can also be observed in the time

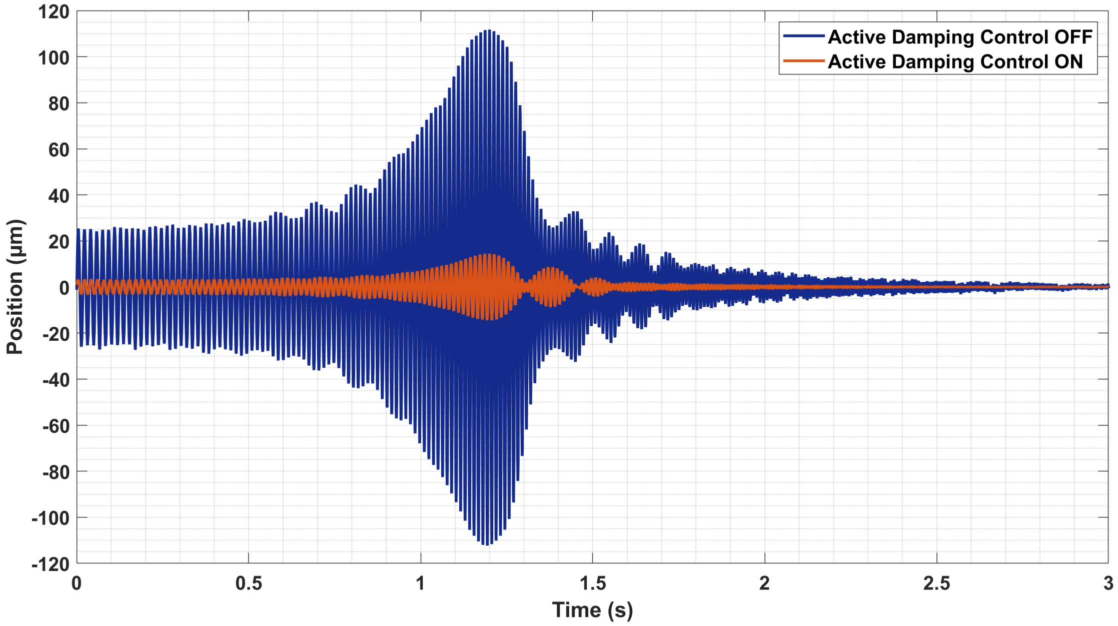

Figure 4.6: Influence of Process Disturbance on the Output Position in Closed-Loop System

domain, as depicted in Fig.4.6, with a focus on the frequency of the parasitic resonance mode. Notably, when active damping control is implemented, the fluctuations in the output position are significantly reduced, demonstrating the effectiveness of overactuation in mitigating disturbances.

4.3 Closed-Loop Motion Control

Through overactuation, the parasitic resonance mode is suppressed, enabling the utilization of higher control bandwidths to enhance motion control. The implementation of a controller with higher bandwidth is conducted in closed-loop experiments using active damping control. The results validate an increase in control bandwidth, represented by the crossover frequency at -3dB, which improves from 17Hz to 32Hz in the closed-loop complementary sensitivity function as depicted in Fig.4.7. This enhanced bandwidth, which is approximately 1.5 times wider, along with the reduction in vibrations, contributes to enhanced tracking performance of the end-effector platform.

The primary objective of a positioning stage is to accurately adhere to a predefined trajectory. To assess the impact of active vibration control on the stage's motion performance, a finite step input is applied to the system. The step tracking performance, illustrated in Fig.4.8, clearly demonstrates that the integration of active damping control with a motion tracking controller effectively decreases the settling time by 74%. This improvement can be attributed to the utilization of a higher control bandwidth, made possible by the reduction of parasitic resonance peak while maintaining stability margins.

Higher control bandwidths allow for higher gains in tuning the PID controller, leading to increased operating voltages of the Lorentz actuator responsible for position tracking, as

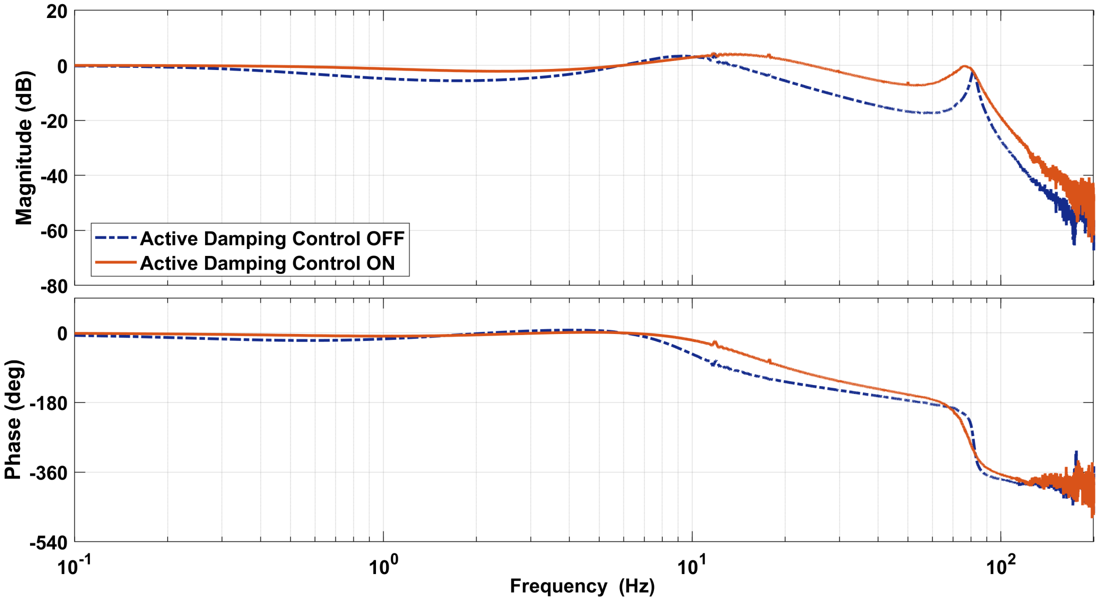

Figure 4.7: Closed-Loop Experimental Complementary Sensitivity Frequency Response

shown in Fig.4.9. The implementation of active damping control results in reduced settling time, but this comes at the cost of a higher initial overshoot. This sudden high spike in the operating voltage occurs as the step reference is inputted, and the actuator rapidly moves the end-effector platform to match the reference position. However, due to the finite stiffness and damping of the connecting flexures, a relative displacement between the two masses occurs, which necessitates a greater control action by the actuator. This can be observed by the

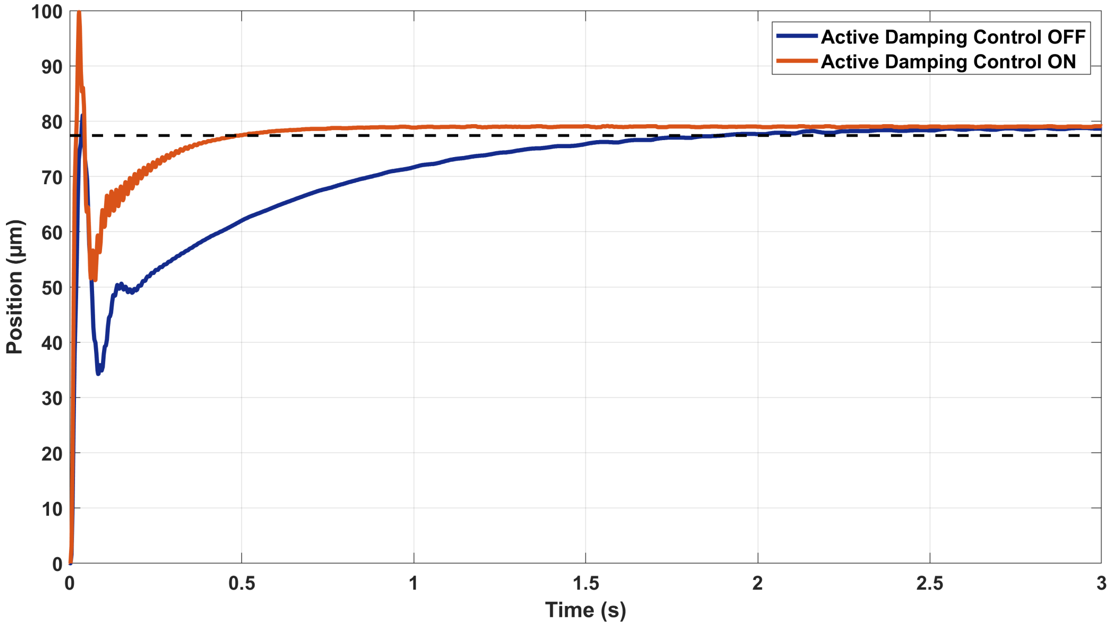

Figure 4.8: Tracking Response to Step Reference

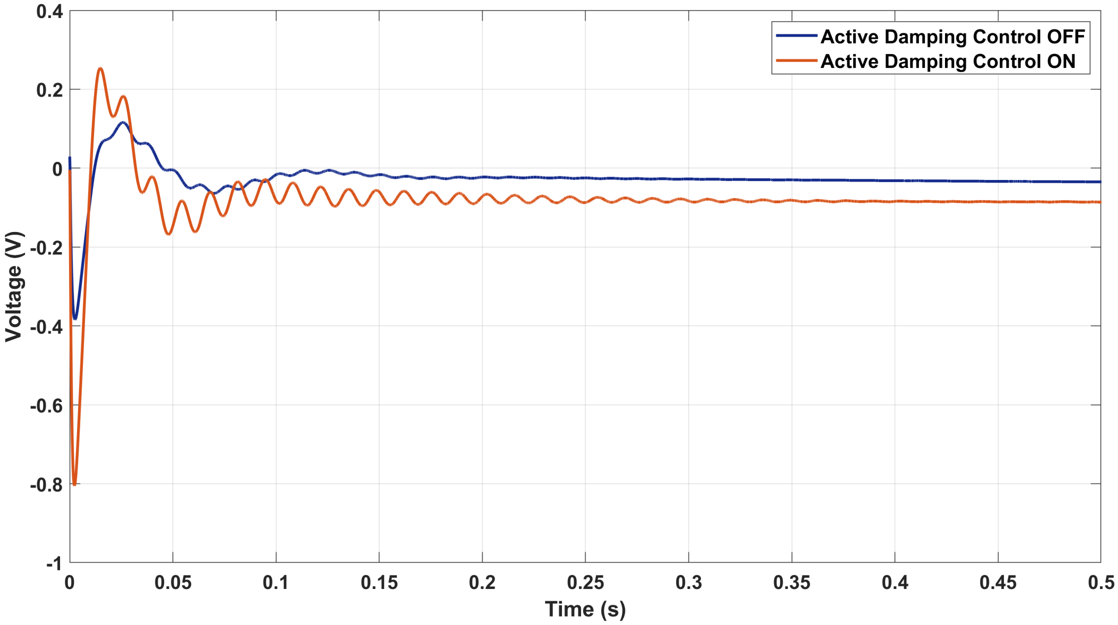

Figure 4.9: Actuation Voltage of the Lorentz Actuator for Reference Tracking

fluctuations in the transient response. Overall, the higher control bandwidth enhances the system's dynamic performance but introduces transient effects during rapid position changes.

Additionally, it is observed that in the steady state, the Lorentz actuator still utilizes a finite operating voltage. This occurrence is attributed to quantization noise or error generated during the conversion process of digital quadrature signals produced by the interferometer

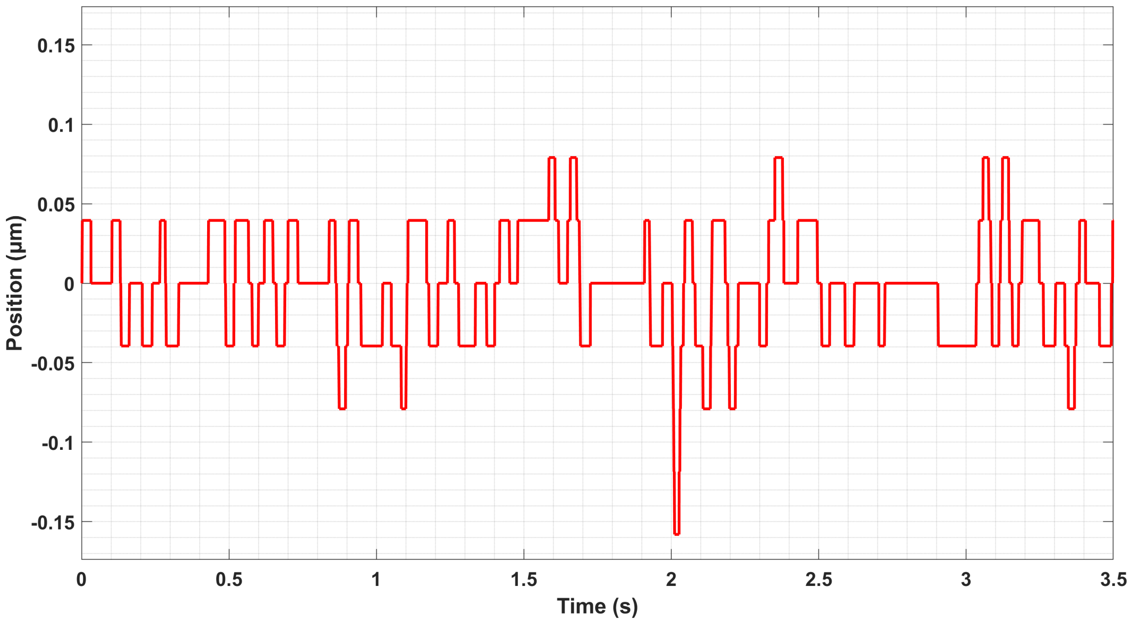

Figure 4.10: Illustration of Quantization Noise in Steady-State Tracking Performance

into analog signals in the compiled Field-Programmable Gate Array (FPGA). The finite resolution (39.5 nm in this experimental study) and clock rate of the input digital signals, as set in the FPGA program, along with the sampling rate employed for the output analog signals, cause the actual analog output to deviate from the ideal continuous waveform represented by the digital value. This difference between the ideal analog value and the actual analog output is known as quantization error or noise, which is depicted in Fig.4.10. While a higher interferometer resolution can potentially reduce this quantization noise, there is a trade-off involved, as explained in Appendix A.2.1.

4.4 Closed-Loop Sensitivity

The experimental setup employs a set of amplifiers for actuators and measurement sensors, each introducing small yet finite noise into the system. These noises can be caused by electronic interference, environmental conditions, or imperfections in their electronic board construction. In a closed-loop system, these individual noises are transmitted through the system and can impact the position output. The controllers use the feedback signal from the sensors to make control decisions, which are then sent to the actuators via these amplifiers. If these noises are significant, the controllers may act upon erroneous measurements, leading to suboptimal or unstable control performance. Therefore, in the context of this experimental setup, it is essential to consider the magnitudes of noise introduced by the different sensors and actuators, which are presented below (see Fig.4.11, 4.12, 4.13, 4.14).

The closed-loop sensitivity frequency response ($n \mapsto x_2$) is depicted in Fig.4.15. It is evident that when active damping control is implemented, the low-frequency sensitivity is low due to the higher gain in the respective PID controller tuned for this scenario. However, in the frequency range after the control bandwidth and up to the parasitic resonance mode frequency, the sensitivity is higher in this case. This is attributed to all four collocated piezoelectric actuator-sensor pairs being active through the implementation of PPF controllers, whose control action is amplified by the voltage amplifiers with a high gain value. As a result, the noise induced by these actuators and sensors is also amplified and transmitted to the performance channel due to the couplings in the MIMO system. To avoid destabilizing the

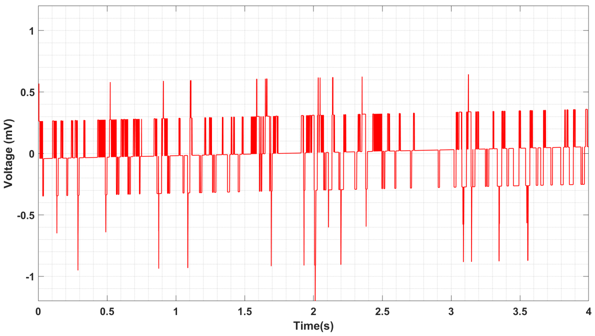

Figure 4.11: Sample of Noise Signal from Lorentz Actuator in series with Current Amplifier

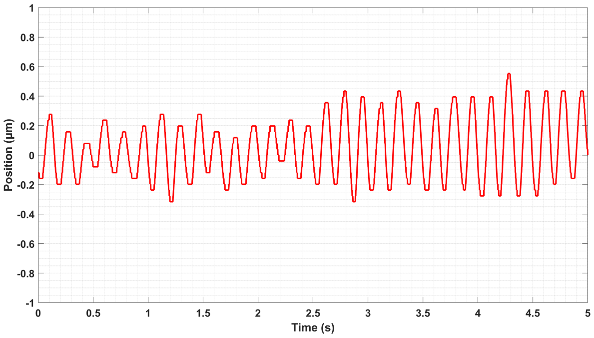

Figure 4.12: Sample of Noise Signal from Interferometer

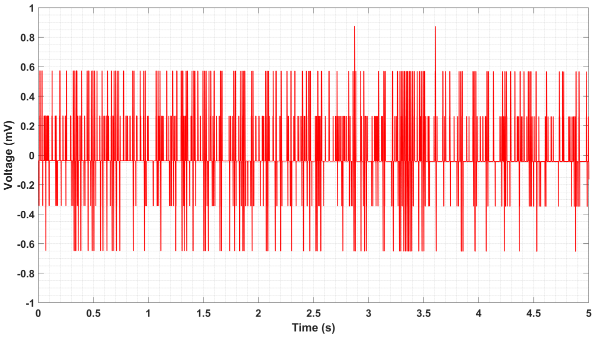

Figure 4.13: Sample of Noise Signal from Piezoelectric Actuator in series with Voltage Amplifier

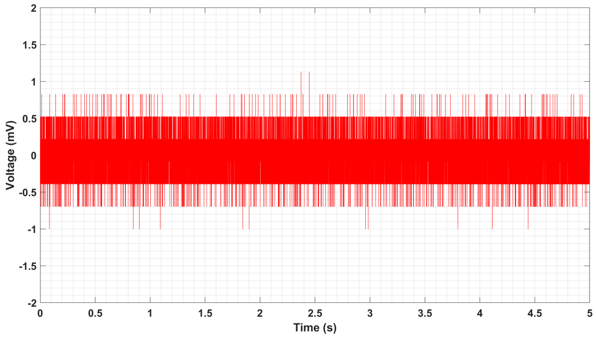

Figure 4.14: Sample of Noise Signal from Piezoelectric Sensor

closed-loop system due to noise amplification in this frequency range, the PPF controllers are tuned with reasonable gain values. However, at high frequencies, the effects of noise are attenuated by the roll-off characteristics of the low-pass filter in series with the PID controller and the second-order PPF controllers, resulting in the sensitivity being equal in either case at high frequencies.

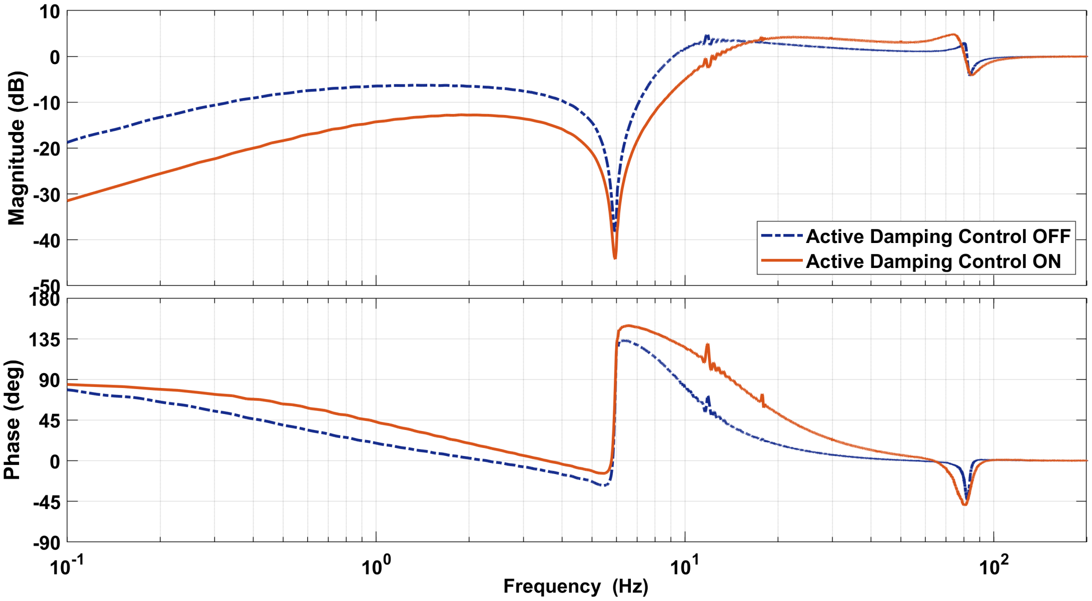

Figure 4.15: Closed-Loop Experimental Sensitivity Frequency Response

5 | Conclusions & Recommendations

5.1 Conclusions

The primary objective of this research was to address the research question formulated in Chapter 1. A novel overactuation-based strategy was proposed to enhance the disturbance rejection and motion-tracking performance of compliant positioning stages. This approach involves implementing active damping control through additional distributed piezoelectric transducers bonded to the flexures in a collocated configuration. A mathematical framework was developed to generalize the contributions of this work, and a numerical model in SPACAR was created to simulate the proposed method's performance. To validate the findings, an experimental setup was constructed using a dual-stage compliant motion system as a proof-of-concept, and the numerical results were verified experimentally.

The core concept of this work is to enable overactuation using lightweight piezoelectric actuator-sensor patches that have minimal impact on the system dynamics in their passive state. These patches allow for additional feedback connections to actively dampen the parasitic vibrations induced in the system, which affect the position accuracy of the end-effector. The patches are strategically bonded to the flexures at locations of maximum strain, corresponding to the parasitic vibration mode to be dampened. This ensures effective control and damping of the targeted mode. Moreover, the research demonstrates that increasing the number of active additional actuators enhances the damping performance, leading to greater suppression of the resonance peak targeted by the damping controllers.

The proposed overactuation-based method demonstrates significant improvement in closed-loop disturbance rejection performance, surpassing the limitations of traditional notch filters. It offers superior performance compared to systems using a single actuator for both motion control and active damping, as the latter may be constrained by controller stability conditions and actuator saturation. In contrast, the proposed approach allows multiple damping controllers in a decentralized setup, each individually tuned with relatively high gains. The combined control action is distributed among the multiple actuators, preventing saturation. Experimental validation shows that as the number of active patches increases, the operating voltages of individual patches decrease, indicating efficient control distribution.

Suppressing the flexible dynamics through the proposed overactuation-based strategy allows for a higher control bandwidth, meeting the desired stability margins. As a result, the closed-loop motion-tracking performance of the system is improved, enabling faster and more accurate tracking of input references. This is confirmed by a substantial reduction in settling time during step reference tracking. However, higher control bandwidths require increased control forces, leading to higher energy consumption in the system. Hence, there exists a trade-off between improved performance and increased energy consumption when considering higher control bandwidths in the system.

Implementing additional actuators and sensors in the system increases its sensitivity to noise, as the presence of these electronic components adds to the total noise in the system. The closed-loop sensitivity analysis demonstrates that the sensitivity is higher when active damping control is implemented. This is primarily due to the relatively high gains of the damping controllers and voltage amplifiers, which amplify the noise in the system. The higher gains amplify not only the control action but also the noise induced by the actuators and sensors, which is then transmitted through the system and affects the position output. This heightened sensitivity to noise is an important consideration when implementing active damping control, as it can impact the overall control performance and stability of the system. Careful design and tuning of the control system are essential to effectively manage noise and achieve the desired control objectives.

In summary, this research presents a significant contribution to the field of positioning systems by introducing a novel approach to address challenges related to flexure-based mechanisms integrated into micro/nano positioning systems. The proposed overactuation-based strategy with distributed piezoelectric transducers bonded to flexures in a collocated configuration enhances disturbance rejection and motion-tracking performance through active damping control. The mathematical framework, numerical model, and experimental validation provide a comprehensive understanding of the proposed method's effectiveness. This approach opens up exciting opportunities for further exploration and application, promising to expand the capabilities and reliability of high-precision positioning systems in various domains.

5.2 Recommendations

The proposed method indeed offers significant advantages; however, like any research, there is always room for further improvements and extensions. These recommendations are classified and presented as follows:

Improvements for Experimental Implementation

The sensitivity of the closed-loop system to noise is a notable challenge stemming from the presence of multiple actuators, amplifiers, and sensors. The noise induced in the system is further amplified by the high gains of the controller and amplifier, leading to potential degradation in the system's position accuracy and stability. This sensitivity poses difficulties in tuning the controller effectively. In the current setup, the use of PiezoDrive BD 300 voltage amplifiers [137], although cost-effective and providing a wide output voltage range ($\pm 300V$), is not the most suitable choice when considering the impact on the signal-to-noise ratio. As an alternative, high-voltage amplifiers from Piezomechanik GmbH [138], or Smart Materials [139]emerge as promising options. These amplifiers offer wider output voltage ranges and high accuracy throughout the voltage range. Implementing these high-quality amplifiers can help mitigate noise-induced issues, enhance the signal-to-noise ratio, and improve the overall closed-loop system performance, making controller tuning more manageable and precise.

The system identification process revealed noise distortions at relatively low frequencies, specifically around 200-1000 Hz. Although the current experimental study employed a sampling rate of 10 kHz, which satisfied the Nyquist theorem for capturing amplitude and frequency components up to 1000 Hz, it is evident that for systems with higher-order modes of concern, a higher sampling rate would be beneficial. To address this, using a higher sampling rate, such as 20 kHz or 50 kHz, would be recommended to accurately capture higher-frequency dynamics. However, this comes at the cost of increased computational effort and data storage, as more data samples would be recorded at each time instance. Upgrading system components, including input-output modules capable of handling higher data rates, may be necessary to accommodate the increased sampling rate. Alternatively, achieving better frequency response can be done by reducing the increased fractions for the input chirp signals during the identification process. This approach would also require more computation effort and time to obtain each measurement data set. Thus, a trade-off must be considered based on the specific requirements of the system and the level of accuracy needed for the frequency response measurements.

The high-pass behavior of the implemented piezoelectric transducers [140], caused by their low capacitance, introduces a phase lead in the identified collocated channel. This phase lead presents a challenge in tuning the PPF controllers to achieve desirable performance. To address this issue, incorporating charge amplifiers with well-calculated resistance and capacitance values can lower the corner frequency of the high-pass behavior in the frequency response while maintaining a high gain (inversely proportional to capacitance in the charge amplifier). This adjustment will facilitate more effective tuning of the PPF controllers and improve system performance. Furthermore, it is important to consider the hysteresis nonlinearity exhibited by piezoelectric transducers. Although this study did not evaluate hysteresis, it is recommended to do so in future investigations. Commonly employed solutions for addressing hysteresis include implementing charge-based control [61], such as charge amplifiers, or employing hysteresis compensators, which have been extensively studied in the literature [19]. By accounting for hysteresis, the performance of these transducers in the system can be improved, leading to better closed-loop performance overall.

After a certain number of operation cycles, a degradation in the performance of the piezoelectric transducers was noticed. The high displacements of the flexures during the system identification process and closed-loop disturbance rejection measurements subject the piezoelectric transducers to mechanical stresses and strains, which possibly lead to material fatigue and wear of the bonding layer over time. To improve the bonding and overall performance, it is recommended to use better bonding solutions, ensure careful manual execution to prevent air bubbles in the bonding layer, and allow sufficient curing time for the bond. Conducting this bonding process in contamination-free spaces can also enhance the reliability of the bonding. During the experimental study, it was noted that each collocated channel exhibited slightly different transfer functions despite being identical sub-systems. To address this, ensuring consistent and precise bonding is essential. Additionally, standard electrical wires were used and soldered to the contact points on the patches, which can be prone to breaking due to stretching or mishandling. To mitigate this issue, it is advised to use flexible PCB-based circuits, which offer greater durability and reliability in transmitting signals. Implementing these improvements will contribute to the long-term stability and repeatability of the experimental setup, enabling more reliable and consistent results in future studies.

Extensions to Current Study

In this study, PPF controllers were utilized for active damping in the inner feedback loop, offering advantages such as effective damping performance and direct utilization of position measurements to avoid numerical differentiation, which can amplify noise and attenuate high-frequency components due to its roll-off characteristics. However, it is crucial to comprehensively analyze other conventional controllers, such as integral resonance control (IRC), for active damping in nanopositioning systems under similar scenarios. Additionally, investigating optimal control techniques based on H_2 and H_∞ norms could be beneficial for maximizing damping performance [103, 141, 142].

Moreover, the use of high gains in PPF control, although enhancing damping and disturbance rejection performance, leads to amplified noise and spillover in the closed-loop system at frequencies below the parasitic resonance mode frequency. Consequently, while the closed-loop process sensitivity improves, there is a trade-off with degraded closed-loop sensitivity in this frequency range. In the closed-loop system, the output position accuracy is influenced by both disturbances and noise transmitting through the closed-loop system, contributing to position error [143]. To address this and optimize the tuning parameters for the damping controller, methodologies like Dynamic Error Budgeting (DEB) should be employed for synthesis [144]. DEB focuses on minimizing the overall error contribution, thereby identifying an optimal balance between disturbance rejection and noise amplification for improved performance.

The observed shifts in the parasitic resonance frequency in the closed-loop system due to the tuning parameters of the damping controller highlight the need for adaptive control strategies. By employing adaptive control techniques, the tuning parameters can be continuously adjusted in real-time based on the acquired data [50, 145, 146]. This approach ensures that the system maintains optimal performance even when operating conditions change, or uncertainties arise. Adaptive control can effectively counteract variations in the system dynamics and provide robust and stable performance, making it a promising avenue to explore for enhancing the overall performance of the positioning system.

Indeed, the proposed method calls for a comprehensive exploration and parameter study of actuator size in conjunction with patch placement. While larger actuator patches with wider and thicker active areas can generate higher actuation forces, it is essential to investigate whether smaller and more compact piezoelectric patches can also achieve comparable performance levels. Understanding the trade-offs between actuator size and performance is crucial for optimizing the design of the positioning system. Moreover, exploring various configurations that incorporate overactuation with a combination of bender patches and stack actuators holds promise. Investigating the benefits and limitations of different actuator combinations will provide valuable insights into tailoring the system design to specific application requirements.

Future Steps

Indeed, the proposed method has demonstrated its advantages on a prototype setup, serving as a proof of concept. However, its practical applicability and scalability to industrial systems, such as nanopositioners used in high-precision applications like wafer alignments, spectroscopy, and metrology, necessitate thorough investigation. Nanopositioning systems in industrial applications are often compact and require high precision, which poses unique challenges to the adaptability of the proposed method. To address these challenges, it is crucial to explore custom-made small and compact piezoelectric patches with higher flexibility to suit the specific requirements of nanopositioners. The market may not currently offer such tailored patches, making it necessary to develop specialized solutions.

Moreover, nanopositioning systems may exhibit geometric nonlinearities due to their compliance, resulting in relatively large deformations. In such cases, employing nonlinear damping feedback controllers has shown promise in the literature. These controllers can rapidly suppress large disturbances while maintaining low sensitivity to noise and avoiding nonlinear vibrations through the generation of nonlinear reacting forces [147, 148]. Additionally, the use of linear PID controllers for motion control in nanopositioning systems can lead to the waterbed effect, which can hinder performance. Integrating strategies like reset control, which has demonstrated superior performance in delivering precision [149–152], with active damping methods in an overactuated system presents exciting opportunities for further enhancing the performance of nanopositioners.

Bibliography

[1] J. W. Ryu, D.-G. Gweon, and K. S. Moon, "Optimal design of a flexure hinge based xyφ wafer stage," *Precision engineering*, vol. 21, no. 1, pp. 18–28, 1997.

[2] S. Devasia, E. Eleftheriou, and S. R. Moheimani, "A survey of control issues in nanopositioning," *IEEE Transactions on Control Systems Technology*, vol. 15, no. 5, pp. 802–823, 2007.

[3] Y. Yong, S. R. Moheimani, B. J. Kenton, and K. Leang, "Invited review article: High-speed flexure-guided nanopositioning: Mechanical design and control issues," *Review of scientific instruments*, vol. 83, no. 12, 2012.

[4] S.-S. Ku, U. Pinsopon, S. Cetinkunt, and S.-i. Nakajima, "Design, fabrication, and real-time neural network control of a three-degrees-of-freedom nanopositioner," *IEEE/ASME transactions on mechatronics*, vol. 5, no. 3, pp. 273–280, 2000.

[5] B.-J. Yi, G. B. Chung, H. Y. Na, W. K. Kim, and I. H. Suh, "Design and experiment of a 3-dof parallel micromechanism utilizing flexure hinges," *IEEE Transactions on robotics and automation*, vol. 19, no. 4, pp. 604–612, 2003.

[6] F. Wang, C. Liang, Y. Tian, X. Zhao, and D. Zhang, "Design of a piezoelectric-actuated microgripper with a three-stage flexure-based amplification," *IEEE/ASME Transactions on Mechatronics*, vol. 20, no. 5, pp. 2205–2213, 2014.

[7] T.-F. Lu, D. C. Handley, Y. Kuan Yong, and C. Eales, "A three-dof compliant micromotion stage with flexure hinges," *Industrial Robot: An International Journal*, vol. 31, no. 4, pp. 355–361, 2004.

[8] S. Polit and J. Dong, "Development of a high-bandwidth xy nanopositioning stage for high-rate micro-/nanomanufacturing," *IEEE/ASME Transactions on mechatronics*, vol. 16, no. 4, pp. 724–733, 2010.

[9] S. Gonda, T. Kurosawa, and Y. Tanimura, "Mechanical performances of a symmetrical, monolithic three-dimensional fine-motion stage for nanometrology," *Measurement Science and Technology*, vol. 10, no. 11, p. 986, 1999.

[10] A. Mazzeo, A. Stein, D. Trumper, and R. Hocken, "Atomic force microscope for accurate dimensional metrology," *Precision engineering*, vol. 33, no. 2, pp. 135–149, 2009.

[11] Y. Yong, A. G. Fowler, A. Mohammadi, and S. Moheimani, "Control of a mems nanopositioner for atomic force microscopy," *IFAC Proceedings Volumes*, vol. 46, no. 5, pp. 375–382, 2013.

[12] B. J. Kenton and K. K. Leang, "Design and control of a three-axis serial-kinematic high-bandwidth nanopositioner," *IEEE/ASME Transactions on Mechatronics*, vol. 17, no. 2, pp. 356–369, 2011.

[13] [Online]. Available: https://www.dynamic-structures.com/product/xsa-200c

[14] L. H. Larry, S. P. Magleby, and B. M. OLsen, "Handbook of compliant mechanisms," *John Wiley & Sons Ltd, Hoboken*, 2013.

[15] S. Awtar, "Fabrication, assembly and testing of a new xy flexure stage with substantially zero parasitic error motions."

[16] T. van der Graaf, "Active vibration control: using over-sensing and over-actuation," 2021.

[17] R. Ding, C. Ding, Y. Xu, W. Liu, and X. Yang, "An optimal actuator placement method for direct-drive stages to maximize control bandwidth," in *IECON 2020 The 46th Annual Conference of the IEEE Industrial Electronics Society*. IEEE, 2020, pp. 556–561.

[18] A. A. Eielsen, M. Vagia, J. T. Gravdahl, and K. Y. Pettersen, "Damping and tracking control schemes for nanopositioning," *IEEE/ASME Transactions on Mechatronics*, vol. 19, no. 2, pp. 432–444, 2013.

[19] G.-Y. Gu, L.-M. Zhu, C.-Y. Su, H. Ding, and S. Fatikow, "Modeling and control of piezo-actuated nanopositioning stages: A survey," *IEEE Transactions on Automation Science and Engineering*, vol. 13, no. 1, pp. 313–332, 2014.

[20] Y. Tao, L. Li, H.-X. Li, and L. Zhu, "High-bandwidth tracking control of piezoactuated nanopositioning stages via active modal control," *IEEE Transactions on Automation Science and Engineering*, vol. 19, no. 4, pp. 2998–3006, 2021.

[21] A. J. Fleming, "Nanopositioning system with force feedback for high-performance tracking and vibration control," *IEEE/Asme Transactions on Mechatronics*, vol. 15, no. 3, pp. 433–447, 2009.

[22] S. Awtar, A. H. Slocum, and E. Sevincer, "Characteristics of beam-based flexure modules," 2007.

[23] "2 leaf springs in parallel," Feb 2022. [Online]. Available: https://www.jpe-innovations.com/precision-point/2-leaf-springs-parallel/

[24] J. Dong, D. Mukhopadhyay, and P. M. Ferreira, "Design, fabrication and testing of a silicon-on-insulator (soi) mems parallel kinematics xy stage," *Journal of micromechanics and microengineering*, vol. 17, no. 6, p. 1154, 2007.

[25] J. Dong and P. M. Ferreira, "Electrostatically actuated cantilever with soi-mems parallel kinematic *xy* stage," *Journal of Microelectromechanical Systems*, vol. 18, no. 3, pp. 641–651, 2009.

[26] D. Mukhopadhyay, J. Dong, E. Pengwang, and P. Ferreira, "A soi-mems-based 3-dof planar parallel-kinematics nanopositioning stage," *Sensors and Actuators A: Physical*, vol. 147, no. 1, pp. 340–351, 2008.

[27] Q. Yao, J. Dong, and P. M. Ferreira, "Design, analysis, fabrication and testing of a parallel-kinematic micropositioning xy stage," *International Journal of Machine Tools and Manufacture*, vol. 47, no. 6, pp. 946–961, 2007.

[28] ——, "A novel parallel-kinematics mechanisms for integrated, multi-axis nanopositioning: Part 1. kinematics and design for fabrication," *Precision Engineering*, vol. 32, no. 1, pp. 7–19, 2008.

[29] S. Awtar and A. H. Slocum, "Constraint-based design of parallel kinematic xy flexure mechanisms," 2007.

[30] Y. Li and Q. Xu, "Design and analysis of a totally decoupled flexure-based xy parallel micromanipulator," *IEEE transactions on robotics*, vol. 25, no. 3, pp. 645–657, 2009.

[31] M. Steinbuch, T. Oomen, and H. Vermeulen, "Motion control, mechatronics design, and moore's law," *IEEJ Journal of Industry Applications*, vol. 11, no. 2, pp. 245–255, 2022.

[32] W. C. Messner, "Classical control revisited: Variations on a theme," in *2008 10th IEEE International Workshop on Advanced Motion Control*. IEEE, 2008, pp. 15–20.

[33] A. A. Dastjerdi, N. Saikumar, and S. H. HosseinNia, "Tuning guidelines for fractional order pid controllers: Rules of thumb," *Mechatronics*, vol. 56, pp. 26–36, 2018.

[34] M. Iwasaki, K. Seki, and Y. Maeda, "High-precision motion control techniques: A promising approach to improving motion performance," *IEEE Industrial Electronics Magazine*, vol. 6, no. 1, pp. 32–40, 2012.

[35] M. Steinbuch and M. L. Norg, "Advanced motion control: An industrial perspective," *European Journal of Control*, vol. 4, no. 4, pp. 278–293, 1998.

[36] Z. Liu, F. Luo, and M. Rashid, “Robust high speed and high precision linear motor direct-drive xy-table motion system,” *IEE Proceedings-Control Theory and Applications*, vol. 151, no. 2, pp. 166–173, 2004.

[37] R. Alkhatib and M. Golnaraghi, “Active structural vibration control: a review,” *Shock and Vibration Digest*, vol. 35, no. 5, p. 367, 2003.

[38] J. A. Butterworth, L. Y. Pao, and D. Y. Abramovitch, “Analysis and comparison of three discrete-time feedforward model-inverse control techniques for nonminimum-phase systems,” *Mechatronics*, vol. 22, no. 5, pp. 577–587, 2012.

[39] S. S. Aphale, A. J. Fleming, and S. R. Moheimani, “Integral resonant control of collocated smart structures,” *Smart materials and structures*, vol. 16, no. 2, p. 439, 2007.

[40] B. Bhikkaji and S. R. Moheimani, “Integral resonant control of a piezoelectric tube actuator for fast nanoscale positioning,” *IEEE/ASME Transactions on mechatronics*, vol. 13, no. 5, pp. 530–537, 2008.

[41] A. J. Fleming and K. K. Leang, “Integrated strain and force feedback for high-performance control of piezoelectric actuators,” *Sensors and Actuators A: Physical*, vol. 161, no. 1-2, pp. 256–265, 2010.

[42] Y. K. Yong and A. J. Fleming, “High-speed vertical positioning stage with integrated dual-sensor arrangement,” *Sensors and Actuators A: Physical*, vol. 248, pp. 184–192, 2016.

[43] C.-X. Li, G.-Y. Gu, M.-J. Yang, and L.-M. Zhu, “Positive position feedback based high-speed tracking control of piezo-actuated nanopositioning stages,” in *Intelligent Robotics and Applications: 8th International Conference, ICIRA 2015, Portsmouth, UK, August 24-27, 2015, Proceedings, Part II 8*. Springer, 2015, pp. 689–700.

[44] J. Fanson and T. Caughey, “Positive position feedback control for large space structures,” *AIAA journal*, vol. 28, no. 4, pp. 717–724, 1990.

[45] B. Bhikkaji, M. Ratnam, and S. R. Moheimani, “Pvpf control of piezoelectric tube scanners,” *Sensors and Actuators A: Physical*, vol. 135, no. 2, pp. 700–712, 2007.

[46] L. Li, C.-X. Li, G. Gu, and L.-M. Zhu, “Positive acceleration, velocity and position feedback based damping control approach for piezo-actuated nanopositioning stages,” *Mechatronics*, vol. 47, pp. 97–104, 2017.

[47] A. K. Babarinde, L.-M. Zhu, and S. S. Aphale, “Simultaneous design of positive acceleration velocity and position feedback based combined damping and tracking control scheme for nanopositioners,” in *2019 18th European Control Conference (ECC)*. IEEE, 2019, pp. 608–613.

[48] A. K. Babarinde, L. Li, L. Zhu, and S. S. Aphale, “Experimental validation of the simultaneous damping and tracking controller design strategy for high-bandwidth nanopositioning–a pavpf approach,” *IET Control Theory & Applications*, vol. 14, no. 20, pp. 3506–3514, 2020.

[49] S. R. Moheimani, B. J. Vautier, and B. Bhikkaji, “Experimental implementation of extended multivariable ppf control on an active structure,” *IEEE Transactions on Control Systems Technology*, vol. 14, no. 3, pp. 443–455, 2006.

[50] R. Orszulik and J. Shan, “Multi-mode adaptive positive position feedback: An experimental study,” in *Proceedings of the 2011 American Control Conference*. IEEE, 2011, pp. 3315–3319.

[51] G. Song, S. Schmidt, and B. Agrawal, “Experimental robustness study of positive position feedback control for active vibration suppression,” *Journal of guidance, control, and dynamics*, vol. 25, no. 1, pp. 179a–182, 2002.

[52] J. Warminski, M. Bochenski, W. Jarzyna, P. Filipek, and M. Augustyniak, “Active suppression of nonlinear composite beam vibrations by selected control algorithms,” *Communications in Nonlinear Science and Numerical Simulation*, vol. 16, no. 5, pp. 2237–2248, 2011.

[53] G. Ferrari and M. Amabili, “Active vibration control of a sandwich plate by non-collocated positive position feedback,” *Journal of Sound and Vibration*, vol. 342, pp. 44–56, 2015.

[54] A. Preumont, *Vibration control of active structures: an introduction*. Springer, 2018, vol. 246.

[55] K. Classens, W. Heemels, and T. Oomen, “A closed-loop perspective on fault detection for precision motion control: With application to an overactuated system,” in *2021 IEEE International Conference on Mechatronics (ICM)*. IEEE, 2021, pp. 1–6.

[56] M. Schneiders, M. Van De Molengraft, and M. Steinbuch, “Benefits of over-actuation in motion systems,” in *Proceedings of the 2004 American control conference*, vol. 1. IEEE, 2004, pp. 505–510.

[57] R. van Herpen, T. Oomen, E. Kikken, M. van de Wal, W. Aangenent, and M. Steinbuch, “Exploiting additional actuators and sensors for nano-positioning robust motion control,” *Mechatronics*, vol. 24, no. 6, pp. 619–631, 2014.

[58] M. Schneiders, M. Van De Molengraft, and M. Steinbuch, “Modal framework for closed-loop analysis of over-actuated motion systems,” *Hal Archives*, vol. 53, no. 7, 2004.

[59] M. G. Schneiders, M. Van De Molengraft, and M. Steinbuch, “Introduction to an integrated design for motion systems using over-actuation,” in *2003 European Control Conference (ECC)*. IEEE, 2003, pp. 3249–3254.

[60] S. D. Galvan, M. Heertjes, and R. Dunand, “Plant enhancements in motion systems by modal control,” in *2012 American Control Conference (ACC)*. IEEE, 2012, pp. 5348–5353.

[61] S. R. Moheimani and A. J. Fleming, *Piezoelectric transducers for vibration control and damping*. Springer, 2006, vol. 1.

[62] H. Hani Ihab Mohammad AlHasni, “Adaptive multimodal damping of flexible structures,” 2021.

[63] J. Holterman, “Vibration control of high-precision machines with active structural elements,” 2002.

[64] P. Avitabile, “Experimental modal analysis,” *Sound and vibration*, vol. 35, no. 1, pp. 20–31, 2001.

[65] S.-M. Kim and J.-E. Oh, “A modal filter approach to non-collocated vibration control of structures,” *Journal of Sound and Vibration*, vol. 332, no. 9, pp. 2207–2221, 2013.

[66] S. Pathak, D. Piron, A. Paknejad, C. Collette, and A. Deraemaeker, “On transmission zeros of piezoelectric structures,” *Journal of Intelligent Material Systems and Structures*, vol. 33, no. 12, pp. 1538–1561, 2022.

[67] M. J. Balas, “Active control of flexible systems,” *Journal of Optimization theory and Applications*, vol. 25, no. 3, pp. 415–436, 1978.

[68] M. Balas, “Feedback control of flexible systems,” *IEEE Transactions on Automatic Control*, vol. 23, no. 4, pp. 673–679, 1978.

[69] V. Buskes, “Distributed vibration control for robotic cantilever beams: Study of optimal control architectures for robotic metamaterials with relative measurements,” 2022.

[70] S. J. Elliott, “Active control of structural vibration,” in *IUTAM Symposium on Vibration Control of Nonlinear Mechanisms and Structures*. Springer, 2005, pp. 1–19.

[71] R. L. Clark and D. E. Cox, “Multi-variable structural acoustic control with static compensation,” *The Journal of the Acoustical Society of America*, vol. 102, no. 5, pp. 2747–2756, 1997.

[72] R. L. Clark and K. D. Frampton, “Aeroelastic structural acoustic control,” *The Journal of the Acoustical Society of America*, vol. 105, no. 2, pp. 743–754, 1999.

[73] C. C. Fuller, S. J. Elliott, and P. A. Nelson, *Active control of vibration*. Academic press, 1996.

[74] A. Preumont, A. François, P. De Man, and V. Piefort, “Spatial filters in structural control,” *Journal of sound and vibration*, vol. 265, no. 1, pp. 61–79, 2003.

[75] M. G. Soto and H. Adeli, “Multi-agent replicator controller for sustainable vibration control of smart structures,” *Journal of Vibroengineering*, vol. 19, no. 6, pp. 4300–4322, 2017.

[76] J. N. Callen, “Distributed control for unmanned vehicles,” *IEEE Concurrency*, vol. 6, no. 2, pp. 16–20, 1998.

[77] E. Omidi and S. N. Mahmoodi, "Consensus positive position feedback control for vibration attenuation of smart structures," *Smart Materials and Structures*, vol. 24, no. 4, p. 045016, 2015.

[78] ——, "Vibration suppression of distributed parameter flexible structures by integral consensus control," *Journal of Sound and Vibration*, vol. 364, pp. 1–13, 2016.

[79] Y. Cheng, "Distributed leader-follower control for large-scale systems," 2015.

[80] M. Blanke, M. Kinnaert, J. Lunze, M. Staroswiecki, and J. Schröder, *Diagnosis and fault-tolerant control*. Springer, 2006, vol. 2.

[81] W. P. Engels, O. N. Baumann, S. J. Elliott, and R. Fraanje, "Centralized and decentralized control of structural vibration and sound radiation," *The journal of the Acoustical Society of America*, vol. 119, no. 3, pp. 1487–1495, 2006.

[82] M. J. Balas, "Direct velocity feedback control of large space structures," *Journal of guidance and control*, vol. 2, no. 3, pp. 252–253, 1979.

[83] L. Marinangeli, F. Alijani, and S. H. HosseinNia, "Fractional-order positive position feedback compensator for active vibration control of a smart composite plate," *Journal of Sound and Vibration*, vol. 412, pp. 1–16, 2018.

[84] C. Goh and T. Caughey, "On the stability problem caused by finite actuator dynamics in the collocated control of large space structures," *International Journal of Control*, vol. 41, no. 3, pp. 787–802, 1985.

[85] M. Muruganandam Mallur, "A comparative study on distributed active damping of flexible systems," 2020.

[86] M. Namavar, A. J. Fleming, M. Aleyaasin, K. Nakkeeran, and S. S. Aphale, "An analytical approach to integral resonant control of second-order systems," *IEEE/ASME Transactions on Mechatronics*, vol. 19, no. 2, pp. 651–659, 2013.

[87] S. S. Aphale, A. J. Fleming, and S. Moheimani, "A second-order controller for resonance damping and tracking control of nanopositioning systems," in *Proc. of the International Conference on Adaptive Structures and Technologies, Ascona, Switzerland*, 2008.

[88] E. Pereira, S. S. Aphale, V. Feliu, and S. R. Moheimani, "Integral resonant control for vibration damping and precise tip-positioning of a single-link flexible manipulator," *IEEE/ASME Transactions on Mechatronics*, vol. 16, no. 2, pp. 232–240, 2010.

[89] A. Al-Mamun, E. Keikha, C. S. Bhatia, and T. H. Lee, "Integral resonant control for suppression of resonance in piezoelectric micro-actuator used in precision servomechanism," *Mechatronics*, vol. 23, no. 1, pp. 1–9, 2013.

[90] İ. F. Lüleci, "Active vibration control of beam and plates by using piezoelectric patch actuators," Master's thesis, Middle East Technical University, 2013.

[91] C. J. Goh, "Analysis and control of quasi distributed parameter systems," Ph.D. dissertation, California Institute of Technology, 1983.

[92] J. L. Fanson, "An experimental investigation of vibration suppression in large space structures using positive position feedback," Ph.D. dissertation, California Institute of Technology, 1987.

[93] M. McEver and D. Leo, "Adaptive low-authority control algorithms for precision space structures," in *Space Technology Conference and Exposition*, 1999, p. 4585.

[94] M. I. Friswell and D. J. Inman, "The relationship between positive position feedback and output feedback controllers," *Smart Materials and Structures*, vol. 8, no. 3, p. 285, 1999.

[95] S. Poh and A. Baz, "Active control of a flexible structure using a modal positive position feedback controller," *Journal of Intelligent Material Systems and Structures*, vol. 1, no. 3, pp. 273–288, 1990.

[96] A. Baz, S. Poh, and J. Fedor, "Independent modal space control with positive position feedback," 1992.

[97] A. Baz and J.-T. HONG, “Adaptive control of flexible structures using modal positive position feedback,” *International journal of adaptive control and signal processing*, vol. 11, no. 3, pp. 231–253, 1997.

[98] K.-H. Rew, J.-H. Han, and I. Lee, “Multi-modal vibration control using adaptive positive position feedback,” *Journal of intelligent material systems and structures*, vol. 13, no. 1, pp. 13–22, 2002.

[99] J. Shan, H.-T. Liu, and D. Sun, “Slewing and vibration control of a single-link flexible manipulator by positive position feedback (ppf),” *Mechatronics*, vol. 15, no. 4, pp. 487–503, 2005.

[100] S. N. Mahmoodi and M. Ahmadian, “Active vibration control with modified positive position feedback,” 2009.

[101] E. Omidi and S. Nima Mahmoodi, “Multimode modified positive position feedback to control a collocated structure,” *Journal of Dynamic Systems, Measurement, and Control*, vol. 137, no. 5, p. 051003, 2015.

[102] G. Ferrari, M. Capriotti, M. Amabili, and R. Garziera, “Active vibration control of a composite sandwich plate,” in *ASME International Mechanical Engineering Congress and Exposition*, vol. 46483. American Society of Mechanical Engineers, 2014, p. V04BT04A075.

[103] A. Paknejad, G. Zhao, M. Osée, A. Deraemaeker, F. Robert, and C. Collette, “A novel design of positive position feedback controller based on maximum damping and h 2 optimization,” *Journal of Vibration and Control*, vol. 26, no. 15-16, pp. 1155–1164, 2020.

[104] G. Barać, “Multimode damping with activated metamaterials: Hexagonal patterned flexure with integrated piezo elements for active damping,” 2020.

[105] J. Curie and P. Curie, “Développement par compression de l’électricité polaire dans les cristaux hémièdres à faces inclinées,” *Bulletin de minéralogie*, vol. 3, no. 4, pp. 90–93, 1880.

[106] J. Holterman and W. Groen, *An Introduction to piezoelectric materials and applications.* Stichting Applied Piezo, 2013.

[107] P. Ge and M. Jouaneh, “Tracking control of a piezoceramic actuator,” *IEEE Transactions on control systems technology*, vol. 4, no. 3, pp. 209–216, 1996.

[108] I. Mayergoyz, “The classical preisach model of hysteresis,” in *Mathematical models of hysteresis.* Springer, 1991, pp. 1–63.

[109] R. H. Comstock, “Charge control of piezoelectric actuators to reduce hysteresis effects,” Apr. 21 1981, uS Patent 4,263,527.

[110] C. Newcomb and I. Flinn, “Improving the linearity of piezoelectric ceramic actuators,” *Electronics Letters*, vol. 11, no. 18, pp. 442–444, 1982.

[111] M. Goldfarb and N. Celanovic, “A lumped parameter electromechanical model for describing the nonlinear behavior of piezoelectric actuators,” 1997.

[112] E. F. Crawley, “Intelligent structures for aerospace-a technology overview and assessment,” *AIAA journal*, vol. 32, no. 8, pp. 1689–1699, 1994.

[113] J. Bruch Jr, J. Sloss, S. Adali, and I. Sadek, “Optimal piezo-actuator locations/lengths and applied voltage for shape control of beams,” *Smart Materials and Structures*, vol. 9, no. 2, p. 205, 2000.

[114] V. M. F. Correia, M. A. A. Gomes, A. Suleman, C. M. M. Soares, and C. A. M. Soares, “Modelling and design of adaptive composite structures,” *Computer Methods in Applied Mechanics and Engineering*, vol. 185, no. 2-4, pp. 325–346, 2000.

[115] V. M. F. Correia, C. M. M. Soares, and C. A. M. Soares, “Refined models for the optimal design of adaptive structures using simulated annealing,” *Composite Structures*, vol. 54, no. 2-3, pp. 161–167, 2001.

[116] J. M. S. Moita, V. M. F. Correia, P. G. Martins, C. M. M. Soares, and C. A. M. Soares, “Optimal design in vibration control of adaptive structures using a simulated annealing algorithm,” *Composite Structures*, vol. 75, no. 1-4, pp. 79–87, 2006.

[117] M. Sunar, S. Hyder, and B. Yilbas, “Robust design of piezoelectric actuators for structural control,” *Computer methods in applied mechanics and engineering*, vol. 190, no. 46-47, pp. 6257–6270, 2001.

[118] R. Barboni, A. Mannini, E. Fantini, and P. Gaudenzi, “Optimal placement of pzt actuators for the control of beam dynamics,” *Smart Materials and Structures*, vol. 9, no. 1, p. 110, 2000.

[119] F. Yang, R. Sedaghati, D. Younesian, and E. Esmailzadeh, “Optimal placement of active bars in smart structures,” in *IEEE International Conference Mechatronics and Automation, 2005*, vol. 1. IEEE, 2005, pp. 1–6.

[120] Q. Wang and C. M. Wang, “Optimal placement and size of piezoelectric patches on beams from the controllability perspective,” *Smart Materials and Structures*, vol. 9, no. 4, p. 558, 2000.

[121] A. Hać and L. Liu, “Sensor and actuator location in motion control of flexible structures,” *Journal of sound and vibration*, vol. 167, no. 2, pp. 239–261, 1993.

[122] Z.-c. Qiu, X.-m. Zhang, H.-x. Wu, and H.-h. Zhang, “Optimal placement and active vibration control for piezoelectric smart flexible cantilever plate,” *Journal of sound and Vibration*, vol. 301, no. 3-5, pp. 521–543, 2007.

[123] I. Bruant and L. Proslier, “Improved active control of a functionally graded material beam with piezoelectric patches,” *Journal of Vibration and Control*, vol. 21, no. 10, pp. 2059–2080, 2015.

[124] A. H. Daraji, J. M. Hale, and J. Ye, “New methodology for optimal placement of piezoelectric sensor/actuator pairs for active vibration control of flexible structures,” *Journal of Vibration and Acoustics*, vol. 140, no. 1, 2018.

[125] N. D. Zorić, A. M. Simonović, Z. S. Mitrović, and S. N. Stupar, “Optimal vibration control of smart composite beams with optimal size and location of piezoelectric sensing and actuation,” *Journal of Intelligent Material Systems and Structures*, vol. 24, no. 4, pp. 499–526, 2013.

[126] T. Seigler, A. H. Ghasemi, and A. Salehian, “Distributed actuation requirements of piezoelectric structures under servoconstraints,” *Journal of intelligent material systems and structures*, vol. 22, no. 11, pp. 1227–1238, 2011.

[127] K. R. Kumar and S. Narayanan, “Active vibration control of beams with optimal placement of piezoelectric sensor/actuator pairs,” *Smart Materials and Structures*, vol. 17, no. 5, p. 055008, 2008.

[128] S. Vidoli and F. Dell’Isola, “Vibration control in plates by uniformly distributed pzt actuators interconnected via electric networks,” *European Journal of Mechanics-A/Solids*, vol. 20, no. 3, pp. 435–456, 2001.

[129] D. Sun, L. Tong, and D. Wang, “Vibration control of plates using discretely distributed piezoelectric quasi-modal actuators/sensors,” *AIAA journal*, vol. 39, no. 9, pp. 1766–1772, 2001.

[130] R. Jamshidi and A. Jafari, “Conical shell vibration control with distributed piezoelectric sensor and actuator layer,” *Composite Structures*, vol. 256, p. 113107, 2021.

[131] J. Qiu and J. Tani, “Vibration control of a cylindrical shell using distributed piezoelectric sensors and actuators,” *Journal of Intelligent Material Systems and Structures*, vol. 6, no. 4, pp. 474–481, 1995.

[132] J. Makarovic, M. Schneiders, A. van der Wielen, E. Lomonova, M. van de Molengraft, R. van Druten, J. Compter, M. Steinbuch, and P. Schellekens, “Integrated design of a lightweight positioning system,” in *7th International Conference on Motion and Vibration Control.* Citeseer, 2004.

[133] T. Oomen and M. Steinbuch, “Model-based control for high-tech mechatronic systems,” in *Mechatronics and Robotics.* CRC Press, 2020, pp. 51–80.

[134] M. Pietrzakowski, “Active damping of beams by piezoelectric system: effects of bonding layer properties,” *International Journal of Solids and Structures*, vol. 38, no. 44-45, pp. 7885–7897, 2001.

[135] H. A. Tinoco, A. L. Serpa, and A. M. Ramos, “Numerical study of the effects of bonding layer properties on electrical signatures of piezoelectric sensors,” *Mecánica Computacional*, vol. 29, no. 86, pp. 8391–8409, 2010.

[136] L. Han, X. Wang, and Y. Sun, "The effect of bonding layer properties on the dynamic behaviour of surface-bonded piezoelectric sensors," *International Journal of Solids and Structures*, vol. 45, no. 21, pp. 5599–5612, 2008.

[137] Piezodrive bd300 dual channel drivers for piezo bender actuators. [Online]. Available: https://www.piezodrive.com/wp-content/uploads/2021/01/BD300-V5-Datasheet-R6.pdf

[138] Piezomechanik gmbh analogue high power amplifier le150. [Online]. Available: https://www.piezomechanik.com/fileadmin/content_files/products/electronics/electronics-2-analogue-amplifier-le150-100.pdf

[139] Smart material eel1500-1. [Online]. Available: https://www.smart-material.com/media/Manuals/EEL1500-1-V1-WEB2021.pdf

[140] S. Kon and R. Horowitz, "A high-resolution mems piezoelectric strain sensor for structural vibration detection," *IEEE Sensors Journal*, vol. 8, no. 12, pp. 2027–2035, 2008.

[141] E. Omidi and N. Mahmoodi, "Hybrid positive feedback control for active vibration attenuation of flexible structures," *IEEE/ASME Transactions on Mechatronics*, vol. 20, no. 4, pp. 1790–1797, 2014.

[142] G. Zhao, A. Paknejad, G. Raze, G. Kerschen, and C. Collette, "H optimization of positive position feedback control for mitigation of nonlinear vibrations," in *ISMA 2018-28th international conference on Noise and Vibration Engineering*. KU Leuven, Leuven, Belgium, 2018.

[143] C. Verhoog, "Optimal active damping performance in presence of disturbance and electronic noise sources," 2023.

[144] W. Monkhorst, "Dynamic error budgeting: A design approach," 2004.

[145] M. K. Kwak, S. Heo, and G.-J. Jin, "Adaptive positive-position feedback controller design for the vibration suppression of smart structures," in *Smart Structures and Materials 2002: Modeling, Signal Processing, and Control*, vol. 4693. SPIE, 2002, pp. 246–255.

[146] S. Nima Mahmoodi, M. Ahmadian, and D. J. Inman, "Adaptive modified positive position feedback for active vibration control of structures," *Journal of Intelligent Material Systems and Structures*, vol. 21, no. 6, pp. 571–580, 2010.

[147] M. Vagia, A. A. Eielsen, J. T. Gravdahl, and K. Y. Pettersen, "Design of a nonlinear damping control scheme for nanopositioning," in *2013 IEEE/ASME International Conference on Advanced Intelligent Mechatronics*. IEEE, 2013, pp. 94–99.

[148] G. Zhao, A. Paknejad, G. Raze, A. Deraemaeker, G. Kerschen, and C. Collette, "Nonlinear positive position feedback control for mitigation of nonlinear vibrations," *Mechanical systems and signal processing*, vol. 132, pp. 457–470, 2019.

[149] J. C. Clegg, "A nonlinear integrator for servomechanisms," *Transactions of the American Institute of Electrical Engineers, Part II: Applications and Industry*, vol. 77, no. 1, pp. 41–42, 1958.

[150] N. Karbasizadeh and S. H. HosseinNia, "Continuous reset element: Transient and steady-state analysis for precision motion systems," *Control Engineering Practice*, vol. 126, p. 105232, 2022.

[151] J. Zheng, Y. Guo, M. Fu, Y. Wang, and L. Xie, "Improved reset control design for a pzt positioning stage," in *2007 IEEE international conference on control applications*. IEEE, 2007, pp. 1272–1277.

[152] H. Li, C. Du, and Y. Wang, "Optimal reset control for a dual-stage actuator system in hdds," *IEEE/ASME Transactions on Mechatronics*, vol. 16, no. 3, pp. 480–488, 2011.

A | Experimental Setup

In this appendix chapter, additional information and detailed descriptions of the components used in the experimental setup are provided.

A.1 System Components

Figure A.1 illustrates the complete system setup in the Mechatronics Lab at the Department of Precision and Microsystems Engineering, showcasing the major components of the system.

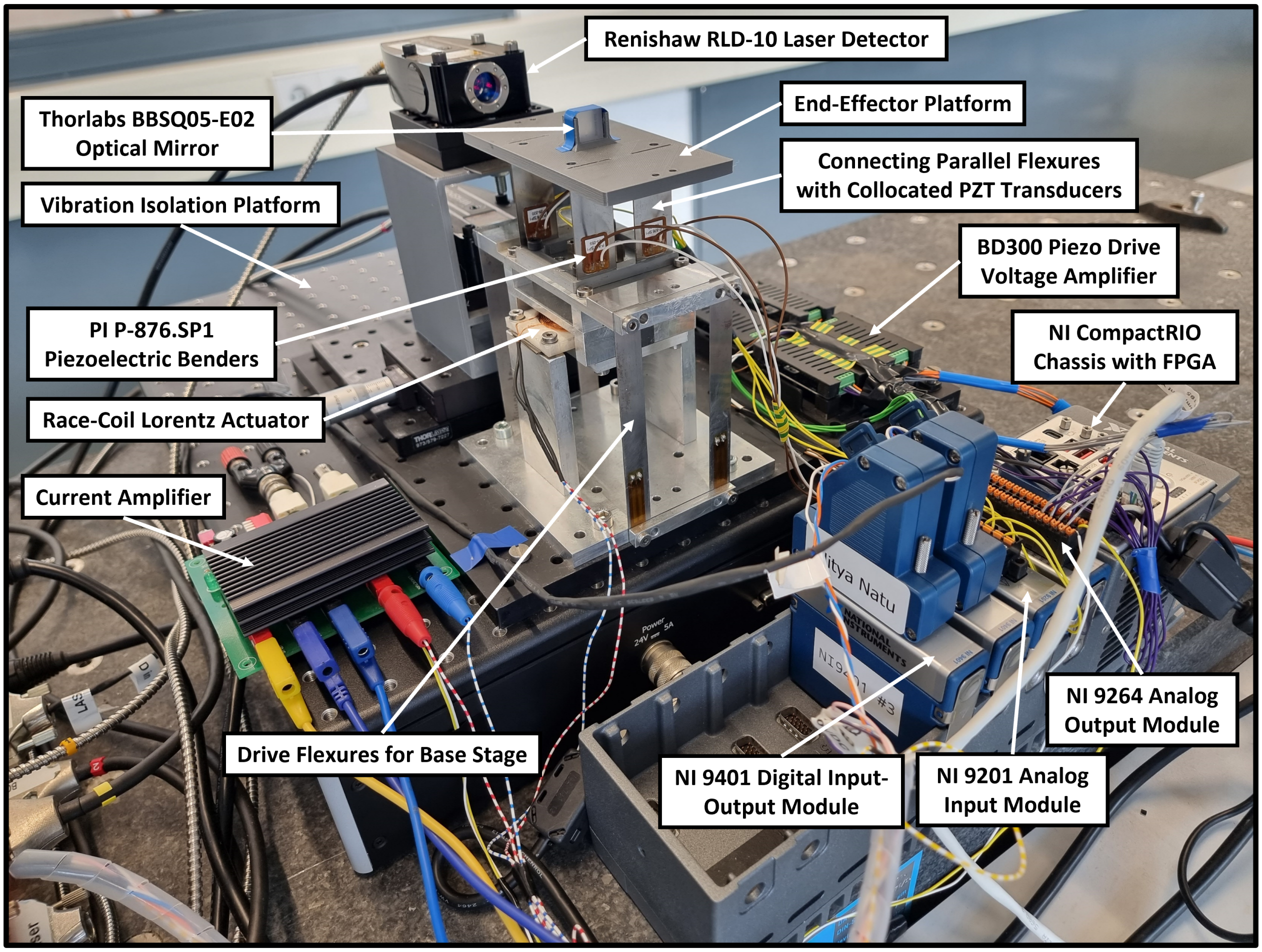

Figure A.1: Experimental Setup

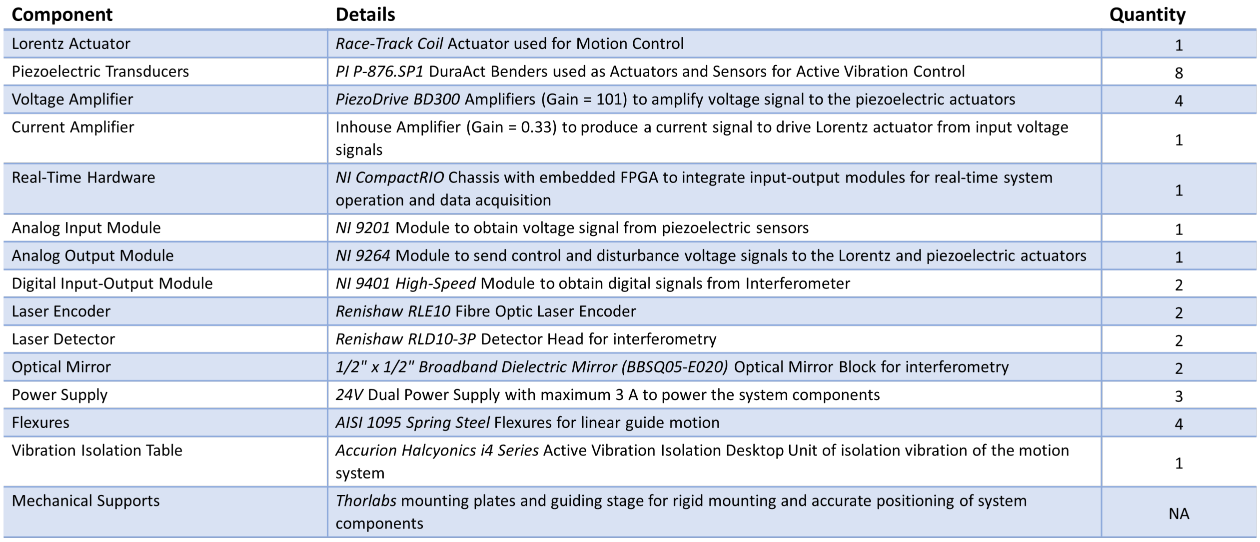

Component	Details	Quantity
Lorentz Actuator	*Race-Track Coil* Actuator used for Motion Control	1
Piezoelectric Transducers	*PI P-876.SP1* DuraAct Benders used as Actuators and Sensors for Active Vibration Control	8
Voltage Amplifier	*PiezoDrive BD300* Amplifiers (Gain = 101) to amplify voltage signal to the piezoelectric actuators	4
Current Amplifier	Inhouse Amplifier (Gain = 0.33) to produce a current signal to drive Lorentz actuator from input voltage signals	1
Real-Time Hardware	*NI CompactRIO* Chassis with embedded FPGA to integrate input-output modules for real-time system operation and data acquisition	1
Analog Input Module	*NI 9201* Module to obtain voltage signal from piezoelectric sensors	1
Analog Output Module	*NI 9264* Module to send control and disturbance voltage signals to the Lorentz and piezoelectric actuators	1
Digital Input-Output Module	*NI 9401 High-Speed* Module to obtain digital signals from Interferometer	2
Laser Encoder	*Renishaw RLE10* Fibre Optic Laser Encoder	2
Laser Detector	*Renishaw RLD10-3P* Detector Head for interferometry	2
Optical Mirror	*1/2" x 1/2" Broadband Dielectric Mirror (BBSQ05-E020)* Optical Mirror Block for interferometry	2
Power Supply	*24V* Dual Power Supply with maximum 3 A to power the system components	3
Flexures	*AISI 1095 Spring Steel* Flexures for linear guide motion	4
Vibration Isolation Table	*Accurion Halcyonics i4 Series* Active Vibration Isolation Desktop Unit of isolation vibration of the motion system	1
Mechanical Supports	*Thorlabs* mounting plates and guiding stage for rigid mounting and accurate positioning of system components	NA

Figure A.2: List of components used in the Experimental Setup

A.2 Actuation and Sensing

In this section, the functionality and implementation of various sensors and actuators used in the experimental setup will be discussed. The following information will be provided, including details on how to connect and operate them effectively.

A.2.1 Interferometer

In order to measure the positions of the system masses, two RENISHAW RLE10 fiber optic laser cable encoders are utilized. These encoders are paired with individual RLD10-3P laser heads, each equipped with a 633 nm wavelength (λ) Helium-neon laser. The laser heads operate using a double pass plane mirror configuration. This configuration involves the laser emitting and reflecting off an optical mirror that is mounted on both the top and base masses of the system. To serve as the optical mirror, a 1/2" x 1/2" Broadband Dielectric Mirror (BBSQ05-E020) from Thorlabs is employed. This mirror has a wavelength range of 400 - 750 nm and is capable of reflecting the laser beam accurately.

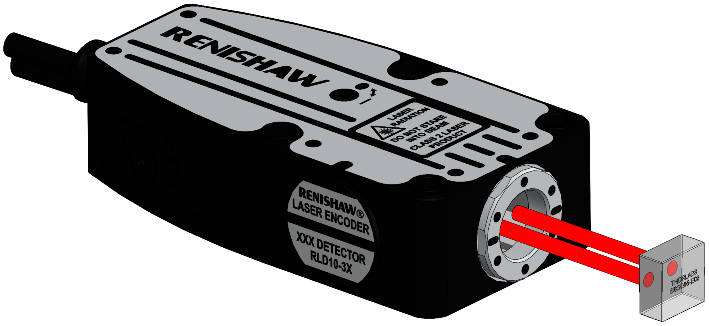

Figure A.3: Illustration of double pass plane mirror configuration of laser head

To minimize the influence of parasitic translations and rotations, arising from the finite displacements of the compliant flexures, on the measurement accuracy, the optical mirror is placed vertically inline and as close as possible to the center of mass of the top moving mass, while for the base mass, the mirror is placed to measure the position in line with the actuation forces and the center of mass.

The laser module and encoder are interconnected using both a fiber optic cable and an electronic cable, which is connected to the detector port of the encoder. The interferometer generates an analog sinusoidal output signal with a $\lambda/4$ period (equal to 158 nm). This analog signal is internally converted to a digital RS422 quadrature signal with a resolution of 39.5 nm. This digital signal represents the measurement resolution of the system. The digital output is then transmitted to the LabVIEW Host user interface through the NI High-speed Digital Input Output (DIO) module. To establish this connection, the 'Fine A Quad', 'Fine B Quad', and '0 V DC' signal lines are routed from the controller port of the encoder to the NI 9924 connector block, which is subsequently linked to the DIO module.

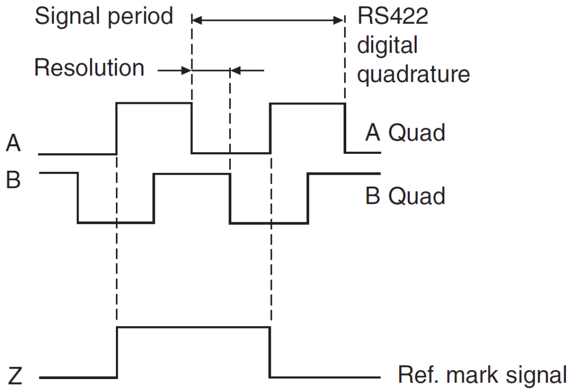

Figure A.4: Illustration of a Digital Quadrature Signal

To ensure the interferometer operates smoothly without triggering overspeed errors during rapid movement of the masses, it is set to its maximum update rate of 20 MHz by enabling Switch 8. This configuration helps maintain the integrity of the system when the masses are moving at relatively high speeds. Consequently, it is necessary to keep the resolution of the interferometer at a small value.

Moreover, to prevent overspeed errors caused by the velocity of the axis, the fine quadrature output is completely disabled. Despite this, a resolution of 39.5nm is still achieved, which is considered sufficient for accurate measurements. This approach ensures that even with a high update rate for the controller input bandwidth, segments of incoming pulses are not missed, thereby preserving the feedback integrity. By implementing these measures, the interferometer can handle fast movements of the masses without encountering overspeed errors, while maintaining a satisfactory resolution. This approach also safeguards against any loss of feedback integrity due to missed pulse segments, particularly when a high update rate for the controller input bandwidth is utilized.

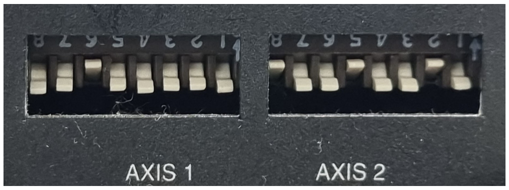

Figure A.5: Switch Configuration of the RLE10 Laser Encoder

A general schematic depicting the connections involved in setting up the interferometer setup is shown in Fig.A.6

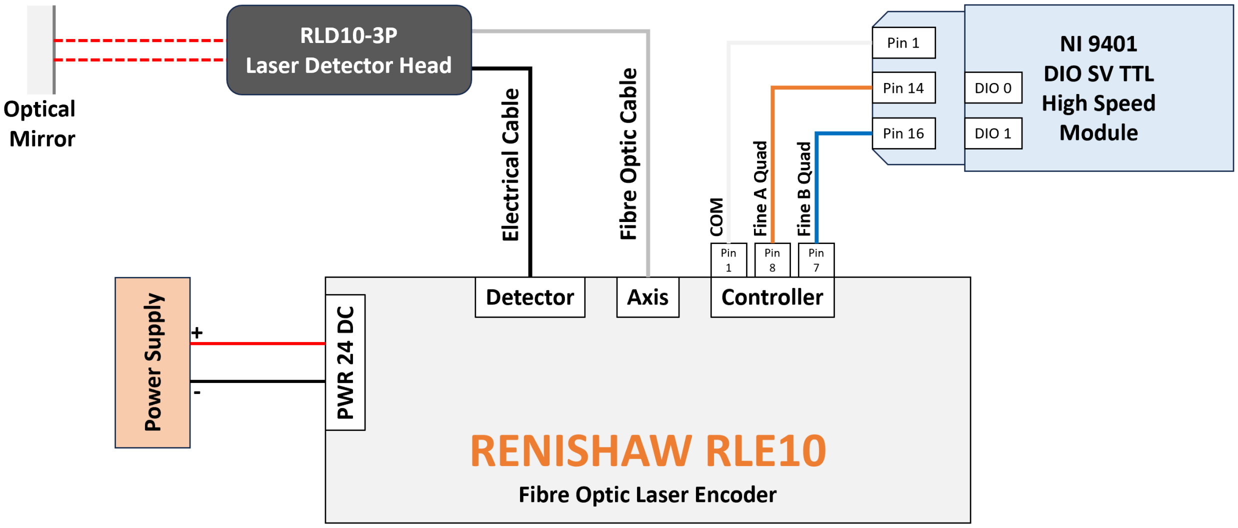

Figure A.6: Schematic of Interferometer Connections

A.2.2 Lorentz Race Track Coil Actuator

In this experimental setup, a Lorentz Race Coil Actuator, previously implemented in the Mechatronics Lab, is employed to actuate and control the position of the base mass. This actuator operates based on the principle of Lorentz force, which arises from the interaction between a coil-shaped current-carrying wire and the magnetic field produced by permanent magnets. The resulting force is directly proportional to the current flowing through the coil and can be expressed as:

$$F = l_w * I \times B \tag{A.1}$$

Here, F represents the resulting force, l_w is the total length of the current-carrying wire exposed to the magnetic field, I denotes the current, and B represents the magnetic flux density.

To avoid wiring between the stator and the mover, the coil is connected to the stator while the permanent magnets are attached to the mover. To ensure a stroke of 10 mm, the actuator incorporates an over-hung configuration in its design. This configuration evenly distributes the position-dependent force gain throughout the entire stroke. The coil design employs an orthocyclic winding technique, which achieves a high fill factor and consequently a high force density.

For detailed information regarding the static properties of the Lorentz actuator, refer to Table A.7.

Actuator specification	**Value**
Resistance R	2.1 Ω
Inductance L	580 μH
No. of windings	140
Coil dimensions	38 × 60 × 2 mm
Magnet dimensions	20 × 6 × 3 mm
Magnet remanent flux density B_r	1.43 T
Average flux density in air gap B_g	0.85 T
Motor constant	1.61 N/A

Figure A.7: Specifications of the Lorentz Actuator

Current Amplifier

In the experimental setup, a current amplifier is employed to convert the low-voltage control signal output into the required electrical current output for driving the Lorentz actuator. Since the actuator's force is controlled and based on the principle of Lorentz force, which is directly proportional to the current, a current feedback circuit is utilized within the amplifier. The race is driven by a current amplifier featuring a TI-OPA548 high-current operational amplifier.

The operational amplifier exhibits linear behavior, as demonstrated in Fig.A.8, and can deliver bidirectional current to generate bidirectional force. The inductive load of the coil acts as a low-pass filter, causing a decrease in current output at higher frequencies. By employing current feedback, the output current remains independent of the frequency-dependent impedance of the actuator. The decrease in currents at high frequencies is compensated by applying a higher output voltage.

Fig.A.9 presents a simplified schematic of the amplifier, illustrating its external connections. The output current of the operational amplifier passes through a feedback resistor R_3, generating a feedback voltage that is fed back into the op-amp. The op-amp is powered by a dual $\pm 10V$ power supply with a $2A$ limit. The control signal utilized is generated by two analog outputs from the NI 9264 Analog Output Module.

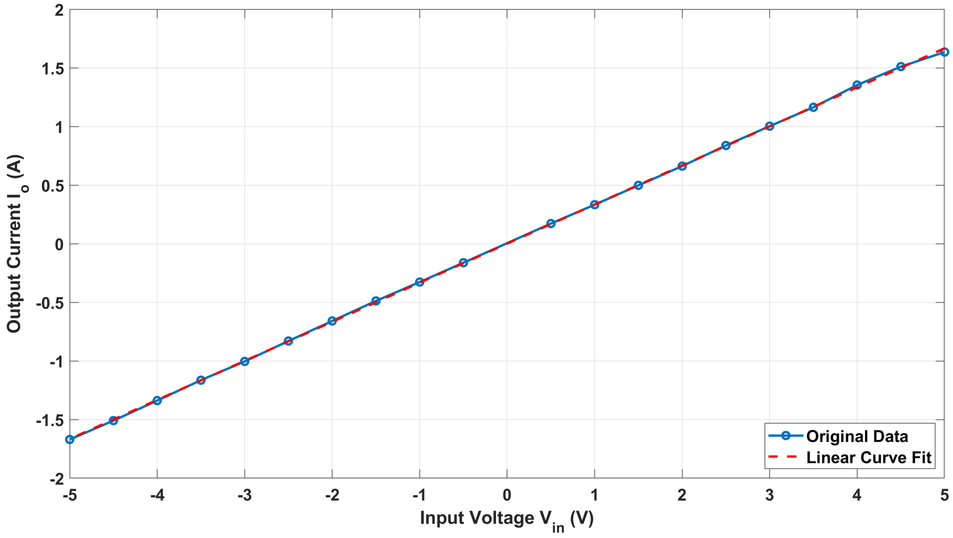

Figure A.8: Linear Behaviour of Current Amplifier

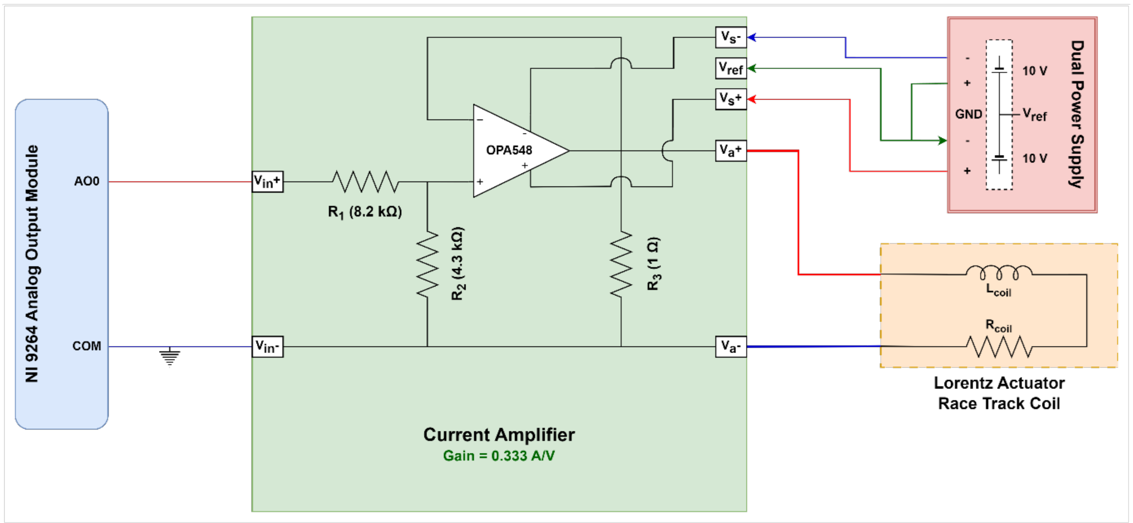

Figure A.9: Schematic of the Current Amplifier Connections

The amplifier gain for this configuration, represented by the output current I_o per unit input voltage V_{in}, can be calculated by

$$\frac{I_o}{V_{\text{in}}} = \frac{R_2}{(R_1 + R_2)} \frac{1}{R_3} \tag{A.2}$$

By appropriately selecting resistances R_1 and R_2 to achieve the desired amplifier gain.

For the specific amplifier used, the measured linear input-output relationship is given by the equation provided,

$$I_o = 0.333 * V_{\text{in}} + 0.00095 \tag{A.3}$$

where the static gain is 0.344 A/V and the offset is 0.95 mA. The amplifier maintains a constant gain with zero phase shift up to its cutoff frequency of approximately 10 kHz, which is sufficient for controlling this system.

A.2.3 Piezoelectric Transducers

In order to achieve active vibration control, the compact P-876.A12 DuraAct patch transducers manufactured by Physik Instrumente (PI) are employed as both actuators and sensors. These transducers are positioned in a collocated configuration on opposite sides of the flexure.

The P-876.A12 DuraAct transducers have the capability to operate at voltages up to 400V, which is well-suited for the intended application. These transducers possess a laminated structure composed of a piezoceramic plate, electrodes, and polymer materials. The polymer coating serves a dual purpose as both electrical insulation and mechanical preload, allowing the transducer to be flexible and capable of bending. To ensure secure attachment, these patches are bonded to the surface of the flexure using epoxy. Additionally, they offer solderable contact points, facilitating electrical connections as required.

Fig.A.10 summarizes the specifications of the patch transducers.

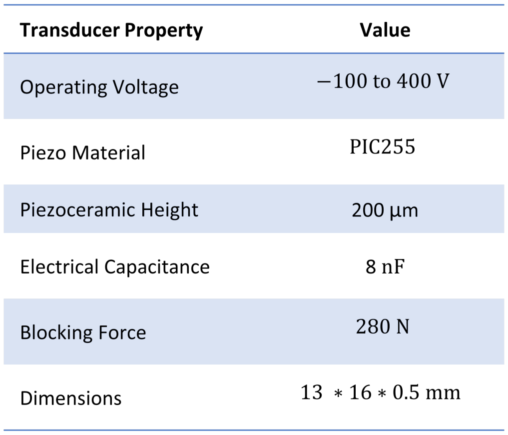

Transducer Property	Value
Operating Voltage	−100 to 400 V
Piezo Material	PIC255
Piezoceramic Height	200 µm
Electrical Capacitance	8 nF
Blocking Force	280 N
Dimensions	13 ∗ 16 ∗ 0.5 mm

Figure A.10: Specifications of the Piezoelectric Bender Transducers

Voltage Amplifiers

The setup utilizes PiezoDrive BD-300 Amplifiers to generate the necessary high voltages for driving the piezoelectric actuators. The amplifiers receive input signals from the NI Analog Output Modules, which have a voltage range of 0-3V. These input signals are then amplified by a factor gain K, allowing the output voltage to range from -300V to +300V. The amplifiers only accept positive voltages and produce a pure sinusoidal output signal in a differential manner using a two-wire configuration with an inverted op-amp setup, as depicted in Fig.A.11. The inverting mode is activated by a small toggle switch located on the rear side of the amplifier board.

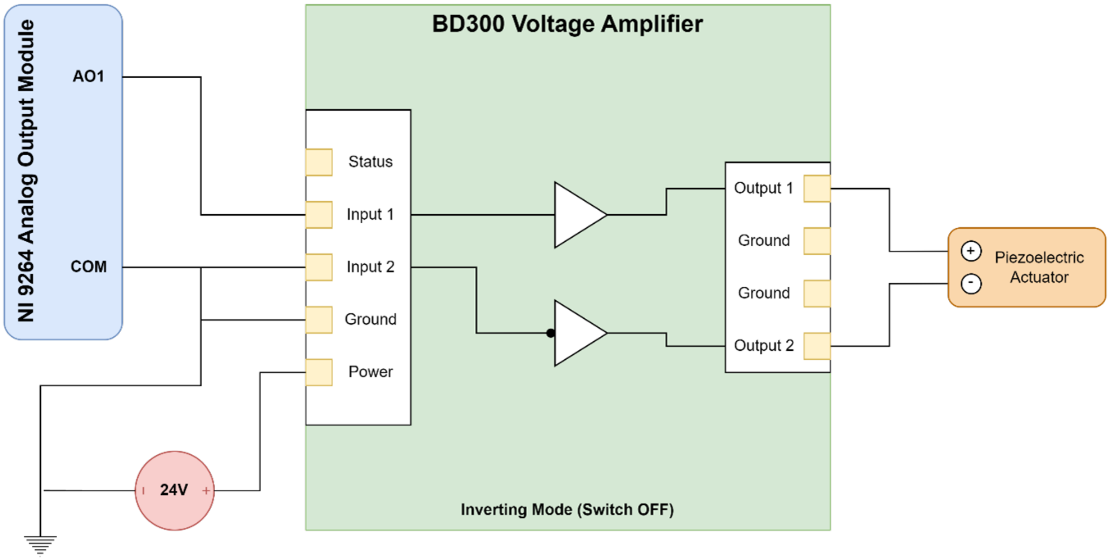

Figure A.11: Schematic of the Voltage Amplifier Connections

The relationship between the output load voltage and the input voltage is described by:

$$V_{\text{load}} = V_1 - V_2 = 2 \cdot K \cdot (V_{\text{in}} - 1.5) \tag{A.4}$$

Therefore, a 1.5V input voltage results in a zero-output voltage. To generate a sinusoidal signal with an output voltage averaging 0V, a LabView program adjusts the offset value in terms of bits corresponding to 1.5V when operating the amplifiers. In this specific experimental setup, 16-bit modules were employed, requiring an offset value of 4915. This value is determined by the linear relationship between the output range of the NI analog output module (-10V to +10V) and the input voltage range of the voltage amplifier. However, in practical scenarios, the offset value needs to be calibrated for each amplifier to account for slight variations, a process facilitated by oscilloscopes. In the current case, where output voltages up to 30V are utilized for actuation, an offset value of 4600 is employed.

The specifications of the amplifier are shown in Fig.A.12

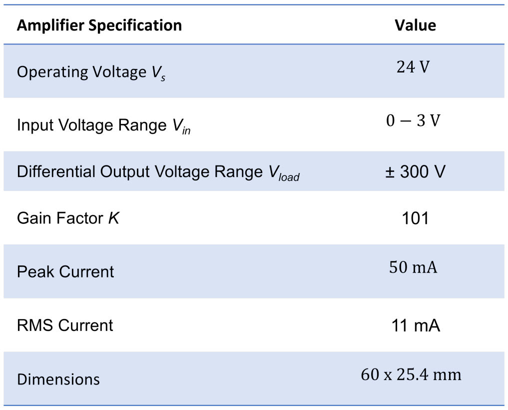

Amplifier Specification	**Value**
Operating Voltage V_s	24 V
Input Voltage Range V_{in}	0 – 3 V
Differential Output Voltage Range V_{load}	± 300 V
Gain Factor K	101
Peak Current	50 mA
RMS Current	11 mA
Dimensions	60 x 25.4 mm

Figure A.12: Specifications of the Voltage Amplifier

B | LabVIEW Project

In this thesis, the LabVIEW (Laboratory Virtual Instrument Engineering Workbench) program provided by National Instruments (NI) has been utilized for the implementation of real-time control and data acquisition of the system measurements. LabVIEW's graphical programming approach simplifies application development by connecting graphical icons, enhancing comprehension of complex systems. It seamlessly integrates with diverse hardware devices, enabling efficient communication and control. Real-time and FPGA (Field Programmable Gate Array) capabilities facilitate high-performance system development and hardware acceleration. Integration with MATLAB combines graphical programming with powerful data analysis, while an extensive library of pre-built tools saves time and effort.

The setup incorporates NI CompactRIO chassis and modules, which provide a flexible hardware configuration, real-time performance, FPGA integration, seamless LabVIEW programming, extensive I/O capabilities, and seamless integration with the LabVIEW ecosystem. These features and advantages make the NI CompactRIO platform well-suited for precise control, monitoring, and data acquisition tasks in the experimental setup.

In this appendix chapter, a comprehensive overview of the various LabVIEW files is provided, along with user instructions. Additionally, a procedure is presented for the implementation of digital controllers designed in MATLAB using LabVIEW. Furthermore, detailed instructions are provided for the post-processing of the measurement data obtained from the experimental setup.

B.1 Project Structure and Input-Output Modules

Fig.B.1 presents a general project schematic and hierarchy of the LabVIEW project employed in this thesis for real-time control implementation and measurement data acquisition. The NI CompactRIO chassis, specifically the *NI-cRIO-9039-01C9917A* model, is utilized as the hardware platform. The chassis is integrated with four modules, including:

- Module 1: NI 9264 Analog Output (AO) Module - responsible for sending voltage signals to the Lorentz Actuator and Piezoelectric Actuator Patches.
- Module 2: NI 9201 Analog Input (AI) Module - used for receiving voltage signals from the Piezoelectric Sensor Patches.

- Modules 3 & 4: NI 9401 High-Speed Digital Input-Output (DIO) Module - responsible for receiving digital quadrature signals from the Interferometers.

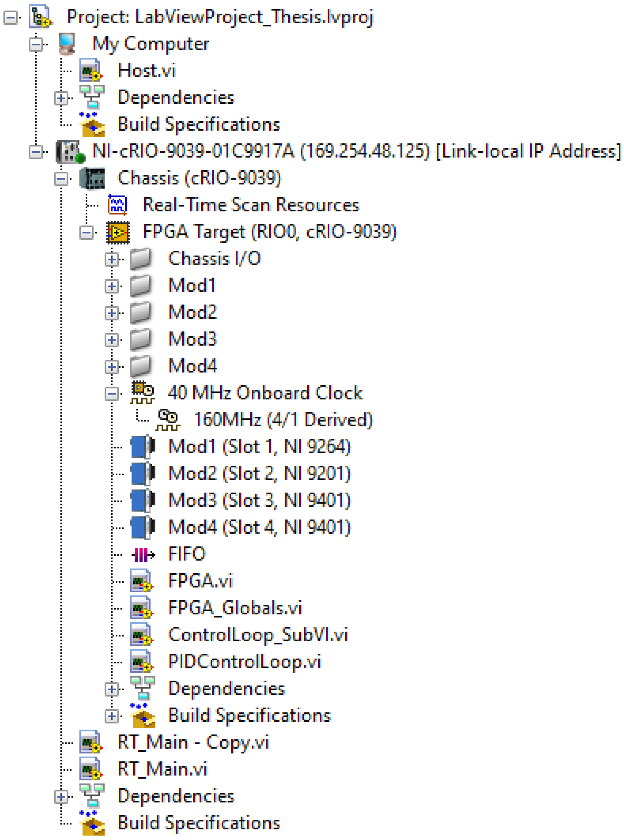

- Project: LabViewProject_Thesis.lvproj
  - My Computer
    - Host.vi
    - Dependencies
    - Build Specifications
  - NI-cRIO-9039-01C9917A (169.254.48.125) [Link-local IP Address]
    - Chassis (cRIO-9039)
      - Real-Time Scan Resources
      - FPGA Target (RIO0, cRIO-9039)
        - Chassis I/O
        - Mod1
        - Mod2
        - Mod3
        - Mod4
        - 40 MHz Onboard Clock
          - 160MHz (4/1 Derived)
        - Mod1 (Slot 1, NI 9264)
        - Mod2 (Slot 2, NI 9201)
        - Mod3 (Slot 3, NI 9401)
        - Mod4 (Slot 4, NI 9401)
        - FIFO
        - FPGA.vi
        - FPGA_Globals.vi
        - ControlLoop_SubVI.vi
        - PIDControlLoop.vi
        - Dependencies
        - Build Specifications
    - RT_Main - Copy.vi
    - RT_Main.vi
    - Dependencies
    - Build Specifications

Figure B.1: LabVIEW Project Structure

The LabVIEW project files are structured to utilize the default 40 MHz onboard clock for all timed loops involved in data generation and acquisition. Additionally, a higher clock speed of 160 MHz is derived specifically for acquiring data from the high-speed DIO module.

The LabVIEW project consists primarily of three significant Virtual Instrument (VI) files: FPGA.vi, RT_Main.vi, and Host.vi.

The **FPGA.vi** file incorporates the complete signal generation and control algorithm, which runs on the CompactRIO Chassis integrated with the FPGA and is compiled using the Xilinx compiler. When modifications are made to this file, recompilation is necessary, which typically takes an average of 15-30 minutes. Consequently, it is essential for the user to strategically plan changes to this file to minimize recompilation time.

The **RT_Main.vi** file serves as an interface between the user's laptop and the CompactRIO. The project utilizes a global variable file called 'FPGA_Globals.vi' to facilitate the use of common variables across different files in the project. This enables the user to conveniently modify any variable that needs manual adjustment through the RT_Main.vi. It is highly recommended to include all variables that require modification during each measurement in this file.

Lastly, the **Host.vi** runs on the user's operating system and is responsible for collecting and visually presenting all the measurement data. The saved data is subsequently imported into MATLAB for further data processing and analysis.

A general workflow of the LabVIEW implementation is depicted in Figure B.2.

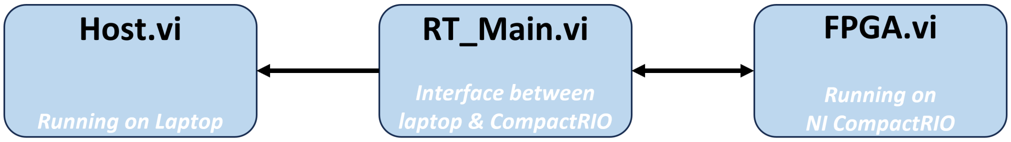

Figure B.2: General workflow of LabVIEW implementation.

The user is advised to follow the recommended order of running files to ensure accurate data processing and acquisition.

1. Open the LabVIEW project file with the '.lvproj' extension.
2. Connect the NI CompactRIO chassis to LabVIEW.
3. Open and run the FPGA.vi.
4. Open the Front Panel of RT_Main.vi and set the experiment parameters.
5. Open the Host.vi file and specify the directory to save the measurement data.
6. Run RT_Main.vi.
7. Run Host.vi and enable data logging.

B.2 FPGA.VI

B.2.1 Sinusoidal Input Signal Generation

For system identification purposes and to introduce process and output disturbances in the closed-loop system measurements, a sinusoidal chirp signal is generated and sent to the Lorentz Actuator and Piezoelectric Actuators. This functionality is implemented using the graphical code depicted in Fig.B.3.

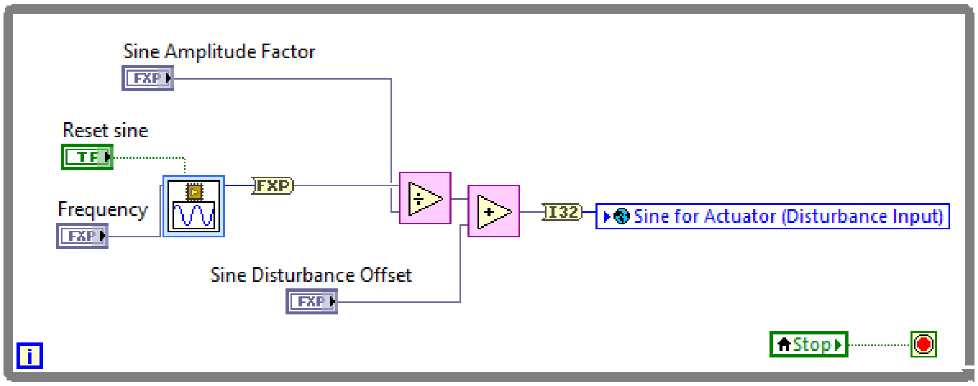

Figure B.3: LabVIEW Graphical Code to generate Sinusoidal Chirp Signals

Depending on whether the signal is directed to the Lorentz actuator or the piezoelectric actuators, different values of *Sine Disturbance Offset* are employed. These values are specified in bits. To set a desired offset of, for example, 1.5 V, the corresponding bit value needs to be inputted. The relationship between bits and output voltage can be determined by considering that the output module has 16 bits and an analog output range of ±10 V. With a bidirectional output voltage, there are $2^{15} = 32768$ bits in each direction (positive and negative). Subtracting one-bit accounts for an unsigned bit representing 0 V, resulting in 32767 bits to represent voltages in the range of 0-10 V. Thus, for a desired voltage offset of 1.5 V, the corresponding bit value will be $32767 * (1.5/10) = 4915$ bits.

The *Amplitude Factor* parameter scales the amplitude of the generated sinusoidal signal. A factor of 100 is used for signals sent to the Lorentz Actuator, while a factor of 40 is used for the piezoelectric actuators. The upper and lower limits of the sinusoid are set in bits to ensure component protection in case of any issues. The frequency of the chirp signal is in a fixed-point value, and the desired frequency value in Hz should be inputted accordingly. When the Boolean *Reset Sine* is set to true, the chirp signal is reset to its original frequency value.

B.2.2 Piezoelectric Sensor Data

To acquire the piezoelectric sensor data from the NI 9201 Analog Input module, the graphical code presented in Fig.B.4 is utilized. Each sensor patch has two wires corresponding to the positive and negative terminals. To avoid ground loops, the code takes the difference between the voltages of the two wires as the sensor measurement.

In addition, the Boolean switch *Home Analog* button, when set to true, is used to calculate the mean of the sensor measurement for a fixed number of data samples. This approach helps reduce background noise and data offset from the sensor, thereby improving the quality of the measurement.

The entire data measurement process is implemented within a timed while loop, ensuring that each data sample is recorded at a fixed time interval. A preset data logging period is

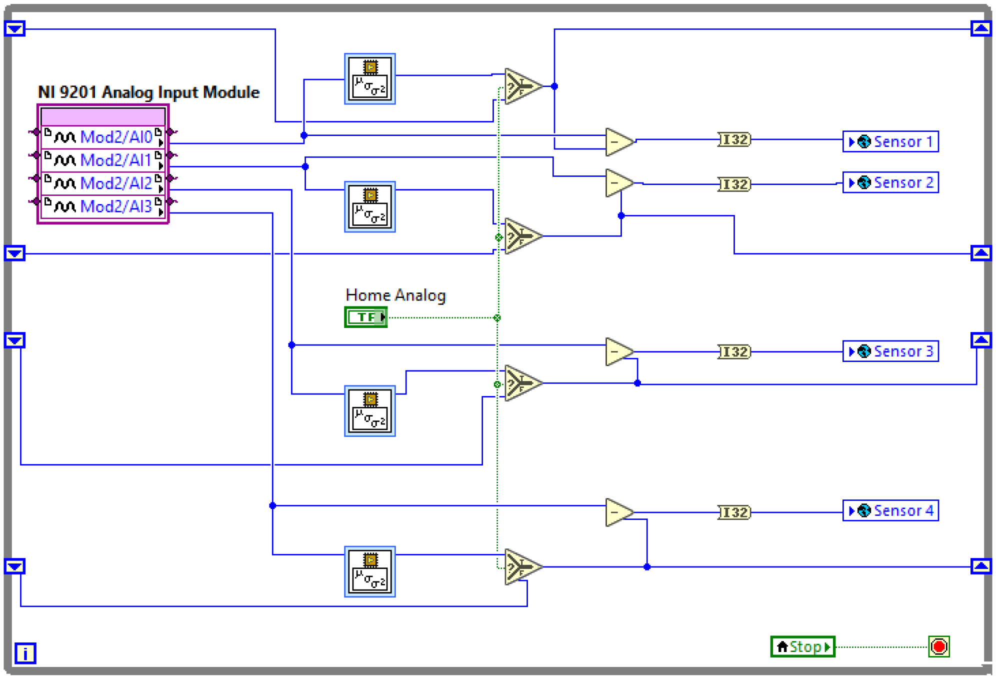

Figure B.4: LabVIEW block diagram for acquiring data from Piezoelectric Sensors

employed to control the sampling rate and maintain a consistent time interval between data points.

B.2.3 Interferometer Data

The digital quadrature signals, specifically the *Fine A Quadrature* and *Fine B Quadrature*, serve as inputs to the NI 9401 DIO Module. To convert these digital quadrature signals into analog signals, a graphical code, as presented in Fig.B.5, is employed.

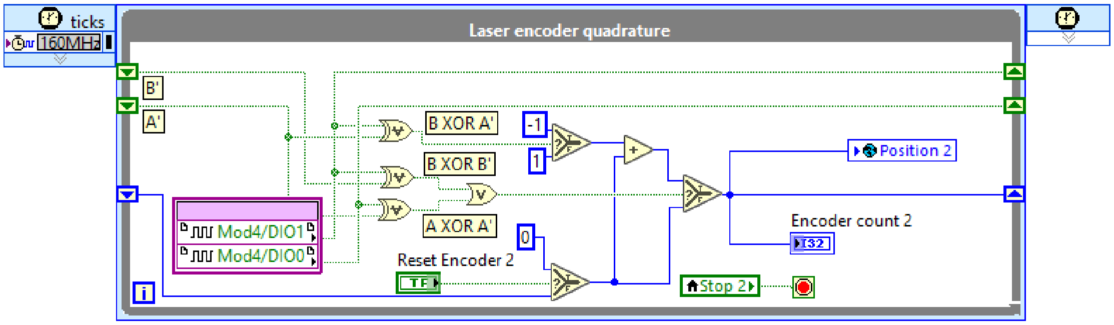

Figure B.5: LabVIEW block diagram for acquiring data from Interferometer

The output obtained from this conversion represents the encoder count, also referred to as the *Position* for ease of interpretation. However, for actual position measurement, the data needs to be multiplied by the resolution of the laser interferometer, which is 39.5 nm. This multiplication accounts for the physical displacement corresponding to the measured count value. To ensure accurate data collection from the interferometer, the entire loop operates at a faster-derived clock rate of 160 MHz. This higher clock rate enables precise sampling and measurement of the digital quadrature signals, providing accurate position information.

B.2.4 Active Vibration Control Loop

For the purpose of active vibration control using the PPF controller, a subVI code is developed and implemented for each collocated piezoelectric actuator-sensor pair. The loop algorithm for the control process is presented in Fig.B.6.

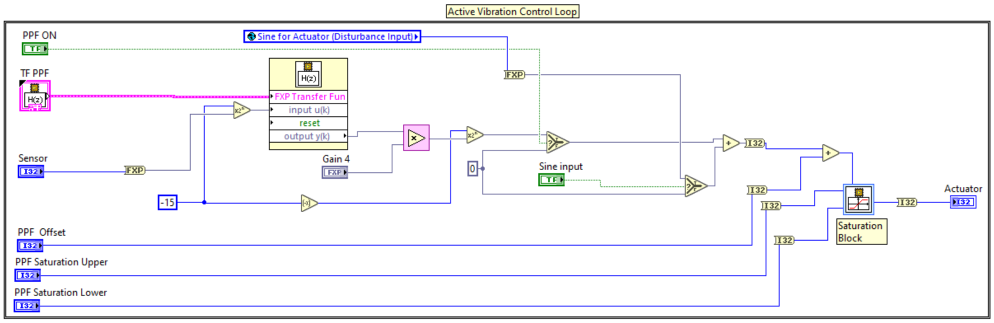

Figure B.6: LabVIEW block diagram for Active Vibration Control Loop

The input to this control loop is the sensor data, which is transmitted through a digitally implemented PPF controller. Based on the controller output, a corresponding actuator voltage is generated. The vibration control loop is only active when the Boolean variable *PPF ON* is set to true. To ensure accurate controller implementation, the integer sensor data is initially converted into a fixed-point representation. This conversion allows for precise calculations within the controller. The loop also provides the option to introduce a disturbance input when the Boolean variable *Sine input* is activated.

Finally, the processed data is converted back to its integer representation to be sent to the NI 9264 Analog Output module. Considering that voltage amplifiers with a positive operational voltage range of 0-3V are employed, a calibrated value of 4600 is set as the *PPF offset*. This value corresponds to the output of the amplifier when it is adjusted to produce a 1.5 V signal for a 0 V input. For safety reasons and to prevent excessive extension or contraction of the actuator patch, saturation limits are implemented using the *PPF Saturation upper* and *PPF Saturation lower* parameters. These limits are applied using a saturation block within the control loop.

B.2.5 Motion Control Loop

For motion control utilizing a tamed-PID controller, a graphical code is implemented as shown in Fig.B.7. The basic operation of this loop is similar to the previously described Active Vibration Control loop. However, there are some differences in the algorithm to accommodate the requirements of motion control.

In this loop, the input is the interferometer data, which is transmitted through the digital PID controller and then output to the Lorentz actuator. A step reference signal is introduced in the *Step Up* parameter, with a step value corresponding to the desired amplitude of the

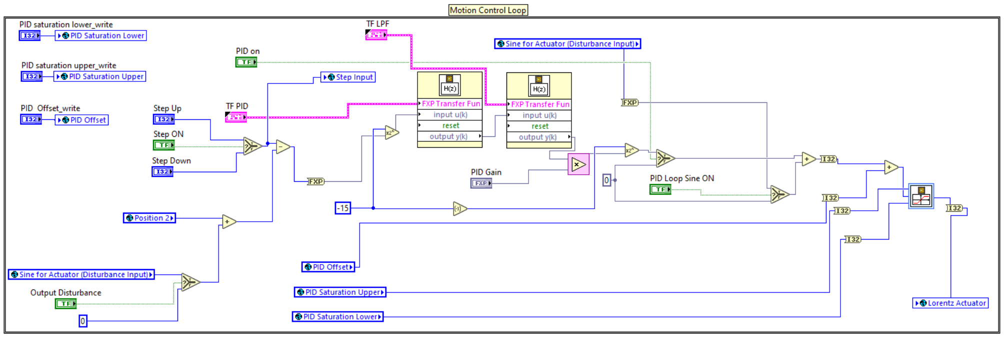

Figure B.7: LabVIEW block diagram for Motion Control Loop

signal. The *Step Down* parameter is usually set to 0. This step reference signal is used for motion tracking and can be activated by setting the *Step ON* Boolean to true.

Additionally, the loop allows for the introduction of process disturbances and output disturbances. The process disturbance is implemented as a sinusoidal signal by setting the *PID Loop Sine ON* Boolean to true. Similarly, the output disturbance can be added by enabling the *Output Disturbance* Boolean. To ensure the system operates within safe limits, saturation limits are provided to prevent excessive motion of the system masses and to avoid overheating of the race track coil actuator. These saturation limits restrict the control output within a predefined range.

B.2.6 Measurement Data to FIFO

In LabVIEW, to acquire real-time data of input and output signals, the signals are written to a First-In, First-Out (FIFO) Write function, as presented in Fig.B.8. The FIFO acts as a data structure, facilitating efficient data transfer and synchronization within the LabVIEW program. The signals are stored in the onboard FIFO memory and can be later accessed and saved in a measurement file. This process is typically implemented within a case structure, utilizing a timed loop for precise timing. Additionally, within the code, the actuator signals are sent to the NI 9264 Analog Output Module for the purpose of actuation. In the described LabVIEW code, the data is converted into an I16 (16-bit integer) representation. This conversion is necessary because the configured data type of the Analog Output (AO) Module is I16.

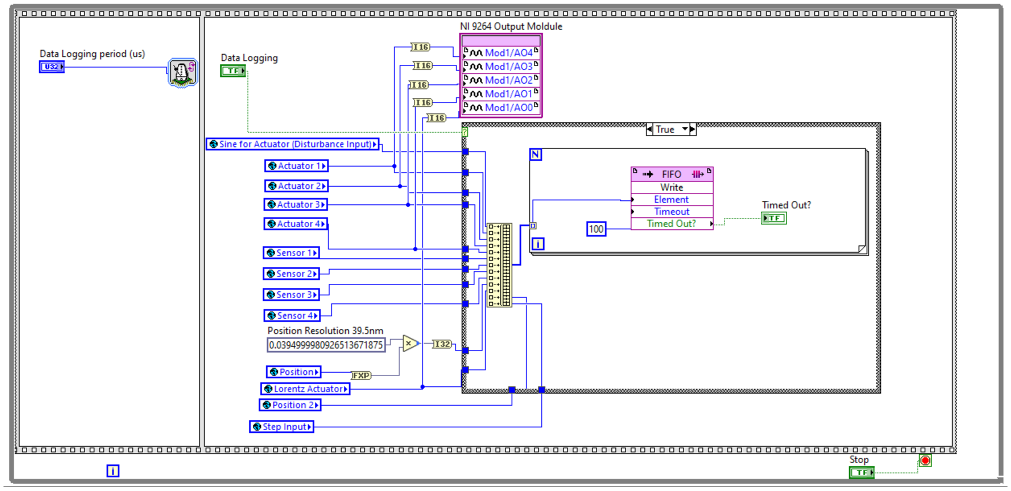

Figure B.8: LabVIEW block diagram for writing measurement data to FIFO

B.3 RT_Main.VI

The front panel depicted in Fig.B.9 showcases the user interface of the RT_Main.vi file. It provides the functionality to manually control actuators, input signals, and configure essential parameters for the effective utilization of the FPGA.vi file.

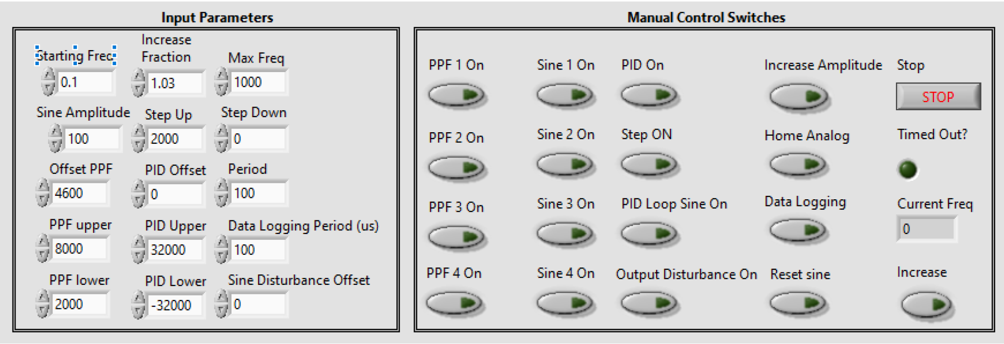
Input Parameters

Starting Freq: 0.1
Increase Fraction: 1.03
Max Freq: 1000
Sine Amplitude: 100
Step Up: 2000
Step Down: 0
Offset PPF: 4600
PID Offset: 0
Period: 100
PPF upper: 8000
PID Upper: 32000
Data Logging Period (us): 100
PPF lower: 2000
PID Lower: -32000
Sine Disturbance Offset: 0

Manual Control Switches

Timed Out?: ●
Current Freq: 0

Figure B.9: Front Panel of the RT_Main.vi File in LabVIEW

The following parameters can be found on the Front Panel, accompanied by brief explanations to guide users in selecting them to perform specific actions:

- **Starting Freq:** Represents the starting frequency of the chirp signal, which is a sinusoid with increasing frequency.
- **Increase Fraction:** Defines the multiplication factor applied to the current frequency at each step of the chirp signal generation.
- **Max Freq:** Sets the maximum frequency limit for the chirp disturbance signal.
- **Increase:** Enables or disables the increase of the current frequency to initiate the chirp signal.
- **Sine Amplitude:** Controls the scaling factor for the desired magnitude of the sinusoidal signal.

- **Increase Amplitude:** Activates or deactivates the increase of the amplitude for the chirp signal.
- **Data Logging:** Determines whether data is logged to the Host.vi file.
- **Reset sine:** Sets the Boolean value to true if the sinusoidal signal needs to be reset and not sent to the actuators.
- **PPF N On:** Enables or disables the PPF controller for the N^{th} piezoelectric sensor-actuator channel.
- **Sine N On:** Activates or deactivates the introduction of a disturbance in the N^{th} piezoelectric sensor-actuator channel.
- **PID On:** Enables or disables the motion control loop.
- **Step On:** Activates or deactivates the step reference signal with the desired amplitude specified in *Step Up*.
- **Step Up:** Sets the desired amplitude for the step reference signal.
- **PID Loop Sine On:** Enables or disables the introduction of a process disturbance input in the motion control loop.
- **Output Disturbance On:** Activates or deactivates the introduction of an output disturbance input in the motion control loop.
- **Offset PPF:** Determines the offset value in bits for the collocated piezoelectric channels.
- **PPF upper:** Sets the upper saturation value in bits for the collocated piezoelectric channels.
- **PPF lower:** Sets the lower saturation value in bits for the collocated piezoelectric channels.
- **PID Offset:** Specifies the offset value in bits for the performance channel.
- **PID Upper:** Establishes the upper saturation value in bits for the performance channel.
- **PID Lower:** Determines the lower saturation value in bits for the performance channel.
- **Data Logging Period (μs):** Sets the data logging period in microseconds (μs), which determines the sampling frequency of the experiments.

B.3.1 Discrete Controller Implementation using MATLAB

The tuned discrete controllers are implemented by assigning their respective numerator and denominator coefficients to arrays, following a specific order as depicted in Fig.B.10. It is important to note that the coefficients are arranged from left to right, representing the lowest to the highest power coefficients. To avoid any errors, it is crucial to consider this order while executing the MATLAB code, as outlined in the steps below:

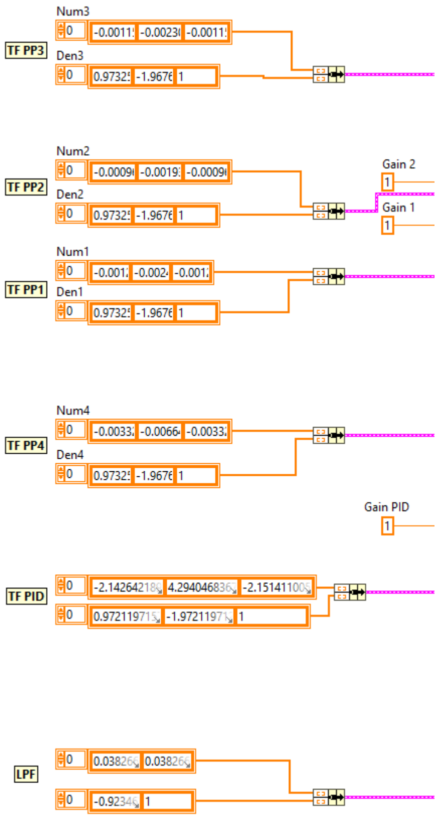

Figure B.10: LabVIEW block diagram to input Discrete Transfer Coefficients in RT_MaIN.vi File

```
%% Discrete PPF Controller Design
load PlantV1.mat % Load MIMO Data

%% Collocated Channel Controllers

% Controller Tuning Parameters
g = 0.7; % Controller Gain
eta = 0.3; % Controller Damping
W = 120*2*pi; % Controller Corner Frequency (Hz)

% PPF for Collocated Channel 1
data = H(2,2); % Load Channel 1 Data
k=1/abs(freqresp(data,150*2*pi)); % Steady State Gain
sign = -1; % Controller Sign for Positive Feedback Loop
PPF1 = sign*tf(1*k*g,[1/W^2 2*eta/W 1]); % Continuous time Transfer Function

% PPF for Collocated Channel 2
data = H(3,3); % Load Channel 2 Data
k=1/abs(freqresp(data,150*2*pi)); % Steady State Gain
sign = -1; % Controller Sign for Positive Feedback Loop
PPF2 = sign*tf(1*k*g,[1/W^2 2*eta/W 1]); % Continuous time Transfer Function

```

```matlab
% PPF for Collocated Channel 3
data = H(4,4); % Load Channel 3 Data
k=1/abs(freqresp(data,150*2*pi)); % Steady State Gain
sign = -1; % Controller Sign for Positive Feedback Loop
PPF3 = sign*tf(1*k*g,[1/W^2 2*eta/W 1]); % Continuous time Transfer Function

% PPF for Collocated Channel 4
data = H(5,5); % Load Channel 4 Data
k=1/abs(freqresp(data,150*2*pi)); % Steady State Gain
sign = -1; % Controller Sign for Positive Feedback Loop
PPF4 = sign*tf(1*k*g,[1/W^2 2*eta/W 1]); % Continuous time Transfer Function

%% Discrete Transfer Function Coefficients
ts = 1e-4; %Sampling Time

PPFd1 = c2d(PPF1,ts,'tustin'); % Discretized PPF for Channel 1
numd1 = flip(vpa(cell2mat(PPFd1.Numerator),20)); % Flipped Discretized Numerator Coefficients for LabVIEW Implementation
dend1 = flip(vpa(cell2mat(PPFd1.Denominator),20)); % Flipped Discretized Denominator Coefficients for LabVIEW Implementation

PPFd2 = c2d(PPF2,ts,'tustin'); % Discretized PPF for Channel 2
numd2 = flip(vpa(cell2mat(PPFd2.Numerator),20));
dend2 = flip(vpa(cell2mat(PPFd2.Denominator),20));

PPFd3 = c2d(PPF3,ts,'tustin'); % Discretized PPF for Channel 3
numd3 = flip(vpa(cell2mat(PPFd3.Numerator),20));
dend3 = flip(vpa(cell2mat(PPFd3.Denominator),20));

PPFd4 = c2d(PPF4,ts,'tustin'); % Discretized PPF for Channel 4
numd4 = flip(vpa(cell2mat(PPFd4.Numerator),20));
dend4 = flip(vpa(cell2mat(PPFd4.Denominator),20));
```

Listing B.1: MATLAB implementation of Discrete PPF Controller

```matlab
%% Discrete PID Controller Design
load G11tfest.mat % Load Undamped Performance Channel Data
load DampPlant_PPF1234_gp7dp3w120_tfest.mat % Load Damped Performance Channel Data

%% Continuous Time PID Controller
wc = 15*2*pi; % Bandwidth (Hz)
wi = wc/10; % Integrator Frequency (Hz)
wd = wc/3; % % Differentiator Frequency (Hz)
wt = 3*wc; % Taming Frequency (Hz)
kp = (0.33)*1/abs(evalfr(DampPlant_PPF1234_gp7dp3w120_tfest,1i*wc)); % Proportional Gain for Damped Performance Channel Data

s = tf('s'); % Initiate Transfer Function variable
sign = -1; % Set controller sign for negative feedback loop

PID = -1*kp*(1+wi/(s+0.001))*(((s/wd)+1)/((s/wt)+1)); % Continuous-Time Transfer Function
```

```
LPF = (1/((s/5000*2*pi)+1)); % Low-Pass Filter (in series with PID Controller)

C = series(PID,LPF); % Combined Tamed-PID with Low-Pass Filter

L = DampPlant_PPF1234_gp7dp3w120_tfest*C;% Open-Loop Transfer Function
isstable(L) % Evaluate Stability
[GM,PM] = margin(L); % Evaluate Stability Margins for Design Requirements

%% Discrete Time PID Controller
ts = 1e-4; %Sampling Time
CdPID = c2d(PID,ts,'tustin'); % Discretized PID Controller using Tustin method
PIDnumd = flip(vpa(cell2mat(CdPID.Numerator),20)); % Flipped Discretized Numerator Coefficients for LabVIEW Implementation
PIDdend = flip(vpa(cell2mat(CdPID.Denominator),20)); % Flipped Discretized Denominator Coefficients for LabVIEW Implementation

%% Discrete Time Low-Pass Filter
CdLPF = c2d(LPF,ts,'tustin'); % Discretized Low-Pass Filter using Tustin method
LPFnumd = flip(vpa(cell2mat(CdLPF.Numerator),20)); % Flipped Discretized Numerator Coefficients for LabVIEW Implementation
LPFdend = flip(vpa(cell2mat(CdLPF.Denominator),20)); % Flipped Discretized Denominator Coefficients for LabVIEW Implementation
```

Listing B.2: MATLAB implementation of Discrete PID Controller

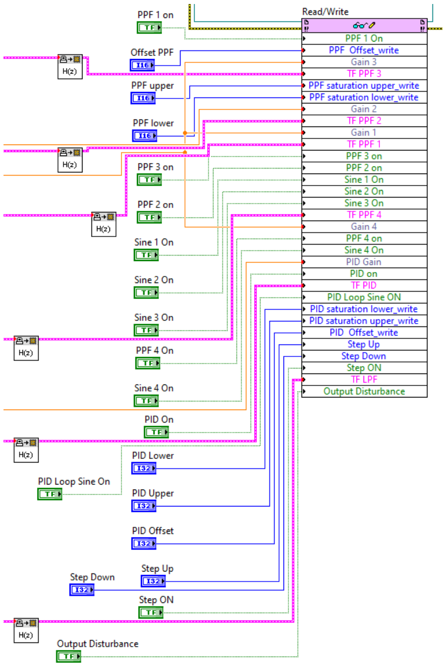

Figure B.11: LabVIEW block diagram to Read and Write manual parameters set by the user in RT_Main.vi File

All the parameters mentioned above, including the transfer functions of the controllers, are passed to the Read/Write function, as shown in Fig.B.11. This allows them to be transmitted to the FPGA.vi when the RT_Main.vi file is executed.

B.4 Host.VI

The Host.vi file serves as an observation and storage tool for data obtained from the experimental setup. Its front panel, as presented in Fig.B.12, includes multiple waveform charts that provide real-time visualizations of sensor measurements and signals sent to the actuators. These waveform charts offer a convenient means to monitor and analyze the data during experimentation. Additionally, the Host.vi file facilitates data storage, allowing users to save the acquired data for further analysis and post-processing.

Figure B.12: Front Panel of the Host.vi File in LabVIEW

In the block diagram of the Host.vi file, the data is read from the FIFO Read function, which contains the data obtained from the FPGA file. The incoming FIFO data is clustered into an array and subsequently saved to a measurement file. This process can be observed in the depicted Fig.B.13.

To ensure proper data acquisition, an *Invoke Method* is implemented in the Host.vi file. This method utilizes the Clean and Run functions to clear the local FIFO memory each time the Host.vi file is executed again. By performing this action, the previous data in the FIFO memory is cleared, allowing for a clean start and accurate data acquisition during each run of the Host.vi file.

Within the *Write To Measurement File* block, various attributes of the measurement file can be defined, including the filename, folder location, and file format. Experimentation with different options revealed that employing the LVM file extension resulted in the fastest data

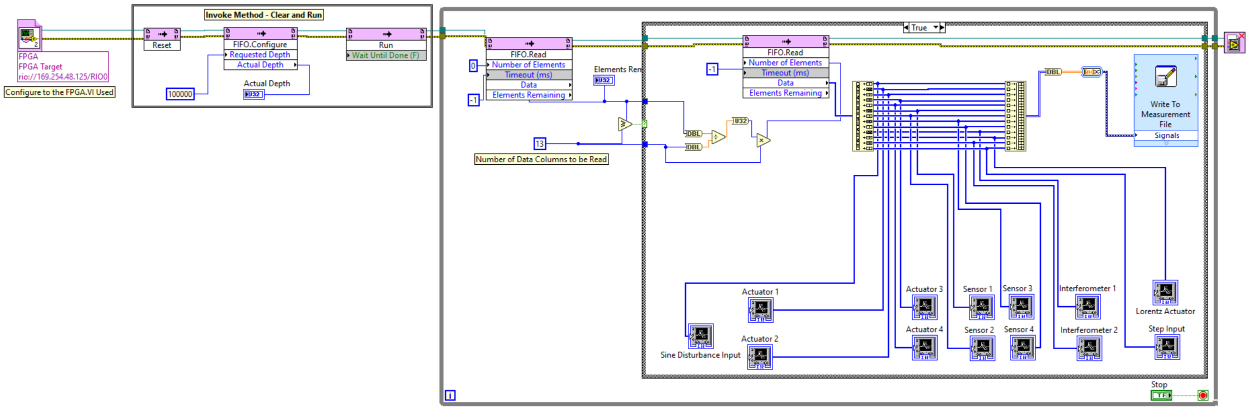

Figure B.13: LabVIEW block diagram of Host.vi File to present and save measurement data

processing within Matlab. Fig.B.14 below illustrates the configuration settings within the 'Write To Measurement File' block.

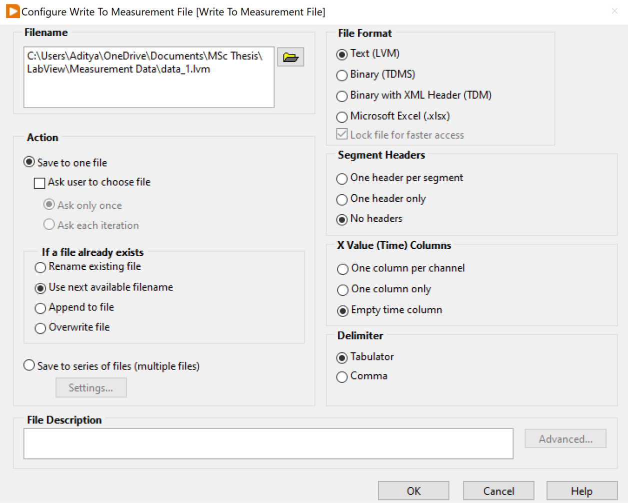
Configure Write To Measurement File [Write To Measurement File]

Filename

C:\Users\Aditya\OneDrive\Documents\MSc Thesis\LabView\Measurement Data\data_1.lvm

Action

● Save to one file

☐ Ask user to choose file

● Ask only once

○ Ask each iteration

If a file already exists

○ Rename existing file

● Use next available filename

○ Append to file

○ Overwrite file

○ Save to series of files (multiple files)

Settings...

File Format

● Text (LVM)

○ Binary (TDMS)

○ Binary with XML Header (TDM)

○ Microsoft Excel (.xlsx)

☑ Lock file for faster access

Segment Headers

○ One header per segment

○ One header only

● No headers

X Value (Time) Columns

○ One column per channel

○ One column only

● Empty time column

Delimiter

● Tabulator

○ Comma

File Description

Advanced...

OK Cancel Help

Figure B.14: Configuration Settings for *Write To Measurement File* in Host.vi File

B.5 Post-Processing of Data in MATLAB

To import the data acquired from the LabVIEW experimental setup into MATLAB for post-processing, the following outlined steps based on the settings specified in Fig.B.14 are involved:

1. Open MATLAB and go to the MATLAB Home tab.
2. From the MATLAB Home tab, select "Import Data."
3. Navigate to the directory where the measurement file is saved.
4. Select the measurement file from the specified directory.
5. In the Import Menu that appears, choose "Column vectors" as the Output Type.

6. In the Import Menu, select "Tab" as the Column Delimiter. This ensures that MATLAB correctly separates the columns based on tab spacing in the data file.
7. If desired, you can change the variable names for the imported data. This step allows you to assign more meaningful names to the variables based on their content.
8. Finally, click on the "Import" button to import the data into MATLAB. The imported data will be stored as variables in the MATLAB workspace, using the specified variable names (or default names if not changed).

Fig.B.15 displays a sample measurement data file.

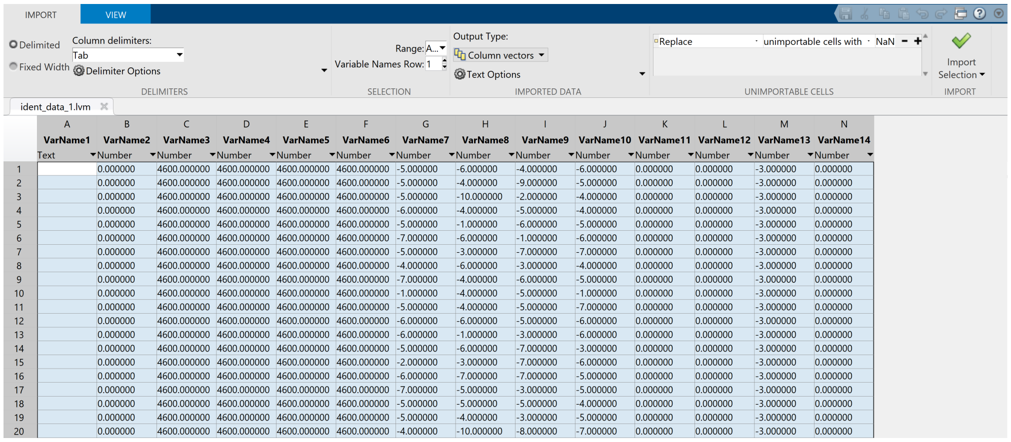

○ Delimited
○ Fixed Width
Column delimiters: Tab
Range: A...
Variable Names Row: 1
Output Type: Column vectors
Replace unimportable cells with NaN

	A	B	C	D	E	F	G	H	I	J	K	L	M	N
	VarName1	VarName2	VarName3	VarName4	VarName5	VarName6	VarName7	VarName8	VarName9	VarName10	VarName11	VarName12	VarName13	VarName14
	Text	Number	Number	Number	Number	Number	Number	Number	Number	Number	Number	Number	Number	Number
1		0.000000	4600.000000	4600.000000	4600.000000	4600.000000	-5.000000	-6.000000	-4.000000	-6.000000	0.000000	0.000000	-3.000000	0.000000
2		0.000000	4600.000000	4600.000000	4600.000000	4600.000000	-5.000000	-4.000000	-9.000000	-5.000000	0.000000	0.000000	-3.000000	0.000000
3		0.000000	4600.000000	4600.000000	4600.000000	4600.000000	-5.000000	-10.000000	-2.000000	-4.000000	0.000000	0.000000	-3.000000	0.000000
4		0.000000	4600.000000	4600.000000	4600.000000	4600.000000	-6.000000	-4.000000	-5.000000	-4.000000	0.000000	0.000000	-3.000000	0.000000
5		0.000000	4600.000000	4600.000000	4600.000000	4600.000000	-5.000000	-1.000000	-6.000000	-5.000000	0.000000	0.000000	-3.000000	0.000000
6		0.000000	4600.000000	4600.000000	4600.000000	4600.000000	-7.000000	-6.000000	-1.000000	-6.000000	0.000000	0.000000	-3.000000	0.000000
7		0.000000	4600.000000	4600.000000	4600.000000	4600.000000	-5.000000	-3.000000	-7.000000	-7.000000	0.000000	0.000000	-3.000000	0.000000
8		0.000000	4600.000000	4600.000000	4600.000000	4600.000000	-4.000000	-6.000000	-3.000000	-4.000000	0.000000	0.000000	-3.000000	0.000000
9		0.000000	4600.000000	4600.000000	4600.000000	4600.000000	-7.000000	-4.000000	-6.000000	-5.000000	0.000000	0.000000	-3.000000	0.000000
10		0.000000	4600.000000	4600.000000	4600.000000	4600.000000	-1.000000	-4.000000	-5.000000	-1.000000	0.000000	0.000000	-3.000000	0.000000
11		0.000000	4600.000000	4600.000000	4600.000000	4600.000000	-5.000000	-4.000000	-5.000000	-7.000000	0.000000	0.000000	-3.000000	0.000000
12		0.000000	4600.000000	4600.000000	4600.000000	4600.000000	-6.000000	-6.000000	-5.000000	-6.000000	0.000000	0.000000	-3.000000	0.000000
13		0.000000	4600.000000	4600.000000	4600.000000	4600.000000	-6.000000	-1.000000	-3.000000	-6.000000	0.000000	0.000000	-3.000000	0.000000
14		0.000000	4600.000000	4600.000000	4600.000000	4600.000000	-5.000000	-6.000000	-7.000000	-3.000000	0.000000	0.000000	-3.000000	0.000000
15		0.000000	4600.000000	4600.000000	4600.000000	4600.000000	-2.000000	-3.000000	-7.000000	-6.000000	0.000000	0.000000	-3.000000	0.000000
16		0.000000	4600.000000	4600.000000	4600.000000	4600.000000	-6.000000	-7.000000	-7.000000	-5.000000	0.000000	0.000000	-3.000000	0.000000
17		0.000000	4600.000000	4600.000000	4600.000000	4600.000000	-7.000000	-5.000000	-3.000000	-5.000000	0.000000	0.000000	-3.000000	0.000000
18		0.000000	4600.000000	4600.000000	4600.000000	4600.000000	-5.000000	-5.000000	-5.000000	-4.000000	0.000000	0.000000	-3.000000	0.000000
19		0.000000	4600.000000	4600.000000	4600.000000	4600.000000	-5.000000	-4.000000	-3.000000	-5.000000	0.000000	0.000000	-3.000000	0.000000
20		0.000000	4600.000000	4600.000000	4600.000000	4600.000000	-4.000000	-10.000000	-8.000000	-7.000000	0.000000	0.000000	-3.000000	0.000000

Figure B.15: Sample of an imported Measurement File in MATLAB

After importing the data into MATLAB, you can utilize it to plot transfer functions and analyze the system response. To achieve this, you need to convert the imported data into Frequency Response Data (FRD) format. The code snippet below demonstrates how to plot the transfer function between two input-output variables:

```matlab
%% SISO Frequency Response

Fs = 1e4; % Sampling Time (Hz)
Input = double(InputData); % InputData is variable name of the input data vector
Output = double(OutputData); % OutputData is variable name of the output data vector

L = length(Input); % Length of Data vectors
wind = hann(L/10); % Hanning Window of length L/10

% Transfer Function Estimate
[Gest,f] = tfestimate(Input,Output,wind,[],[],Fs);

% FRD Data
Gfrd = frd(Gest,2*pi*f,1/Fs);

% Plot Identified Transfer Function
figure(); bode(Gfrd); grid on
```

Listing B.3: MATLAB Code for SISO Transfer Function Estimate

C | System Identification

This appendix chapter outlines the procedure employed for identifying the Multiple-Input Multiple-Output (MIMO) system. It includes a concise depiction and interpretation of the collocated and performance channels, as well as the MATLAB codes required to implement digital controllers in LabView and process the measurement data.

C.1 Identification Process

To determine the dynamics of the MIMO system, predefined input signals are applied to the respective actuators within the system, and the corresponding time-domain data is measured using onboard sensors. The input signals used are sinusoidal chirp signals with frequencies ranging from 0.1 to 1000 Hz. The maximum frequency measured is set to one-tenth of the sampling frequency, in accordance with the Nyquist theorem, to effectively capture both frequency and amplitude components. The amplitudes of the voltage signal inputs are carefully selected to ensure a small yet detectable response. An example of such an input signal is depicted in Fig.C.1.

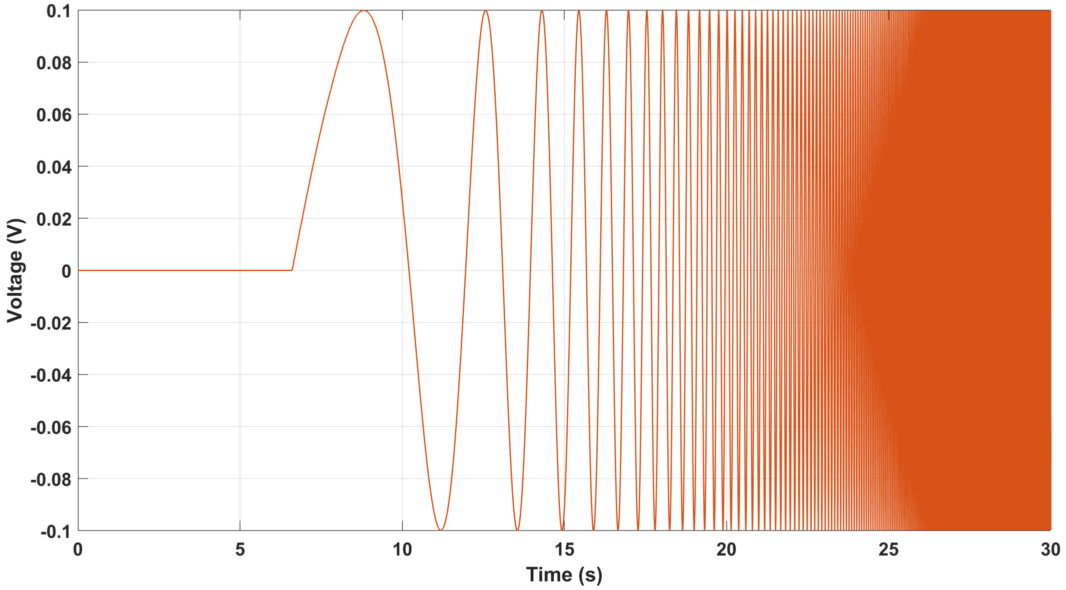

Figure C.1: Sample Sinusoidal Chirp Input Signal used for System Identification

Following the measurement of the system's time data response with known inputs, the frequency response of the system is estimated using the *tfestimate* function from the System Identification Toolbox in MATLAB. The general MATLAB code structure for estimating the frequency response of a single-input single-output channel is provided below. Please note that the above code structure is for a single-input single-output (SISO) channel. This is adapted for the multiple-input multiple-output (MIMO) system by considering the appropriate input signals and output data for each channel.

All the frequency responses presented below are estimated without the use of windowing. However, in practical scenarios, and for enhanced clarity, a *hanning* window is commonly employed to obtain a less noisy response.

C.2 MIMO Identified System

The identified $5 * 5$ MIMO system is presented in Fig.C.2

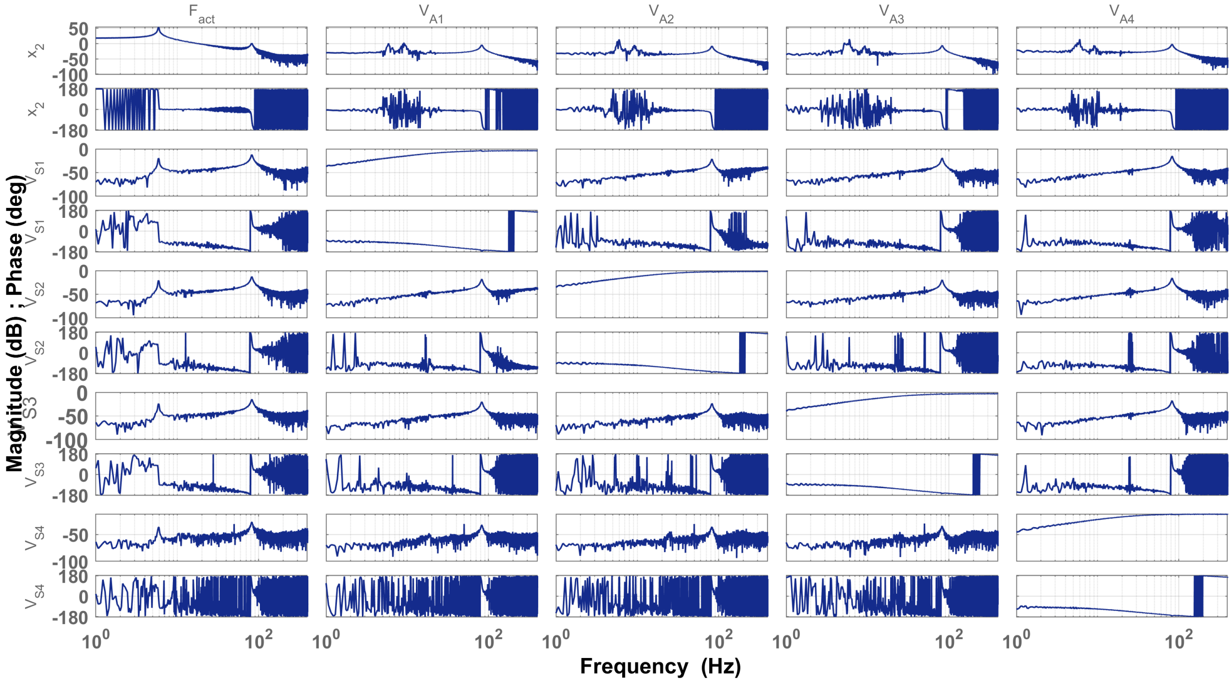

Figure C.2: Frequency Response of 5*5 MIMO System Identified

```
%% MIMO System Identification

% Load complete data for 5*5 MIMO System
load Col1.mat % Time Data of all sensors and Lorentz Actuator
load Col2.mat % Time Data of all sensors and PZT Actuator 1
load Col3.mat % Time Data of all sensors and PZT Actuator 2
load Col4.mat % Time Data of all sensors and PZT Actuator 3
load Col5.mat % Time Data of all sensors and PZT Actuator 4

Fs = 1e4; % Sampling Frequency (Hz)
```

```
%% Transfer Function Estimate (No Windowing)

% MIMO 1st Column Frequency Response
[Hresp(1,1,:),freq] = tfestimate(Act,Int2a,[],[],[],Fs);
[Hresp(2,1,:),freq] = tfestimate(Act,S1a,[],[],[],Fs);
[Hresp(3,1,:),freq] = tfestimate(Act,S2a,[],[],[],Fs);
[Hresp(4,1,:),freq] = tfestimate(Act,S3a,[],[],[],Fs);
[Hresp(5,1,:),freq] = tfestimate(Act,S4a,[],[],[],Fs);

% MIMO 2nd Column Frequency Response
[Hresp(1,2,:),freq] = tfestimate(A1,Int2b,[],[],[],Fs);
[Hresp(2,2,:),freq] = tfestimate(A1,S1b,[],[],[],Fs);
[Hresp(3,2,:),freq] = tfestimate(A1,S2b,[],[],[],Fs);
[Hresp(4,2,:),freq] = tfestimate(A1,S3b,[],[],[],Fs);
[Hresp(5,2,:),freq] = tfestimate(A1,S4b,[],[],[],Fs);

% MIMO 3rd Column Frequency Response
[Hresp(1,3,:),freq] = tfestimate(A2,Int2c,[],[],[],Fs);
[Hresp(2,3,:),freq] = tfestimate(A2,S1c,[],[],[],Fs);
[Hresp(3,3,:),freq] = tfestimate(A2,S2c,[],[],[],Fs);
[Hresp(4,3,:),freq] = tfestimate(A2,S3c,[],[],[],Fs);
[Hresp(5,3,:),freq] = tfestimate(A2,S4c,[],[],[],Fs);

% MIMO 4th Column Frequency Response
[Hresp(1,4,:),freq] = tfestimate(A3,Int2d,[],[],[],Fs);
[Hresp(2,4,:),freq] = tfestimate(A3,S1d,[],[],[],Fs);
[Hresp(3,4,:),freq] = tfestimate(A3,S2d,[],[],[],Fs);
[Hresp(4,4,:),freq] = tfestimate(A3,S3d,[],[],[],Fs);
[Hresp(5,4,:),freq] = tfestimate(A3,S4d,[],[],[],Fs);

% MIMO 5th Column Frequency Response
[Hresp(1,5,:),freq] = tfestimate(A4,Int2e,[],[],[],Fs);
[Hresp(2,5,:),freq] = tfestimate(A4,S1e,[],[],[],Fs);
[Hresp(3,5,:),freq] = tfestimate(A4,S2e,[],[],[],Fs);
[Hresp(4,5,:),freq] = tfestimate(A4,S3e,[],[],[],Fs);
[Hresp(5,5,:),freq] = tfestimate(A4,S4e,[],[],[],Fs);

%% Create FRD model

H = frd(Hresp,2*pi*freq,1/Fs); % 5*5 MIMO Frequecny Response Data

%% Plot FRD model

% Bode Plot Options
opts = bodeoptions('cstprefs');
opts.FreqUnits = 'Hz';
opts.XLim= [1 1e3];
opts.PhaseVisible = 'on';
opts.Grid = 'on';
opts.PhaseWrapping = 'off';

figure(); bode(H,opts)  % 5*5 MIMO Frequecny Response
```

Listing C.1: MATLAB Code for MIMO System Identification

C.3 Collocated Channel

Fig.C.3 illustrates the frequency response of the collocated channels originating from each of the four collocated piezoelectric actuators to the sensor patch. It is evident that the gains of each channel vary. This discrepancy can be attributed to the electro-mechanical coupling between the piezoelectric patch and the flexure, which arises from variations in the bond layer resulting from the manual bonding process.

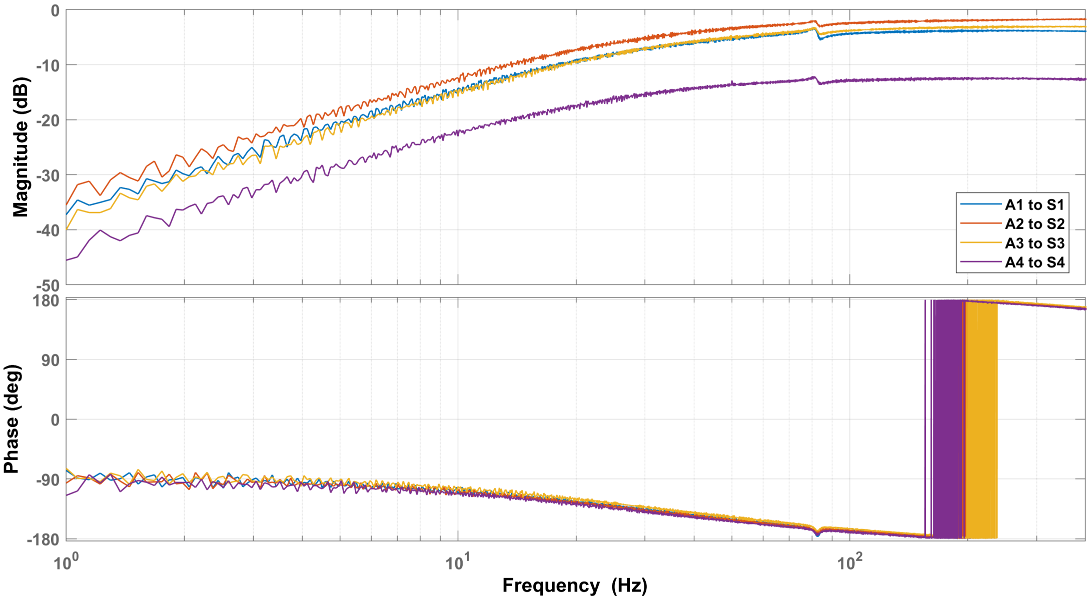

Figure C.3: Frequency Response of Identified Collocated Piezoelectric Actuator to Sensor Channels

Fig.C.4 depicts a magnified view of one of the collocated channels. It is evident that the frequency response exhibits a pole-zero pattern, which aligns with the expected behavior from the literature. This characteristic pole-zero pattern arises due to the collocated configuration of the piezoelectric actuator and sensor, confirming the theoretical predictions.

C.4 Performance Channel

Fig.C.5 displays the performance channel extending from the Lorentz actuator to the interferometer ($F_{act} \mapsto x_2$). It is noticeable that the resonance peak frequencies for the first two relevant modes align with those computed in the analytical model. Minor deviations can be attributed to the absence of the electro-mechanical coupling factor in the SPACAR model. It is important to note that the gains in this frequency response exhibit significant variation compared to the analytical model due to the inclusion of actuator and amplifier dynamics in this particular frequency response.

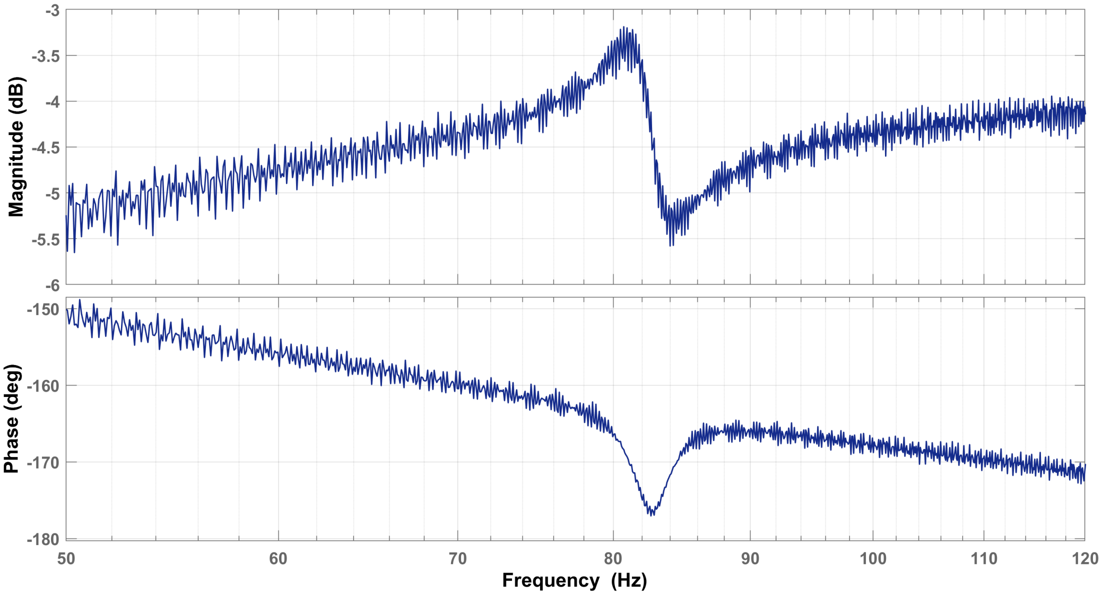

Figure C.4: Zoomed Frequency Response of Identified Collocated Channel depicting Pole-Zero Interlacing

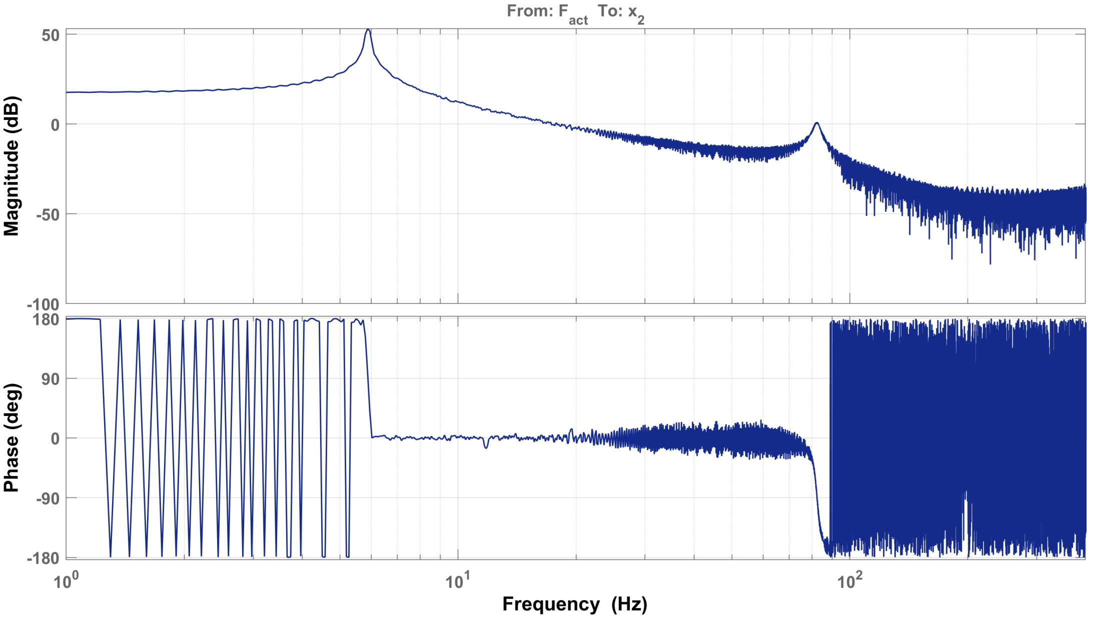

Figure C.5: Frequency Response of Identified Performance Channel $F_{act} \mapsto x_2$

C.5 Windowing for Transfer Function Estimate

Based on the system identification plots presented above, it is apparent that the estimation becomes increasingly noisy and distorted as the frequencies being analyzed become higher. This distortion is attributed to spectral leakage, a phenomenon observed when analyzing signals of limited duration in the frequency domain. Spectral leakage causes energy from a specific frequency component to spread into neighboring frequency bins, resulting in the emergence of extra spectral components or sidelobes surrounding the intended frequency components of interest. Consequently, these sidelobes can obscure or distort the desired frequency response, resulting in the presence of noise or spurious peaks within the estimated spectrum. To mitigate this issue, the application of windowing during the transfer function estimation process can considerably minimize the impact of spectral leakage.

Fig.C.6 illustrates the frequency response estimation of the performance channel using different windowing lengths. In the system identification process, sinusoidal inputs were employed, making the use of *hann* windows ideal since they are well-suited for such signals with similar characteristics. It is evident that when a single window of the input signal length is used, there is a considerable amount of high-frequency distortion. This distortion is primarily caused by the noise being perceived as a linear dynamic in this particular case. Conversely, as the number of window lengths increases, the distortion is significantly reduced, resulting in a more accurate frequency response. With a higher number of windows, even the third resonance peak around 180 Hz frequency becomes clearly visible. However, it is important to note that the magnitude of the frequency response in the low-frequency range is also affected in an undesired manner. Therefore, it is crucial to strike a balance by selecting an appropriate window length during the identification of each channel's frequency response.

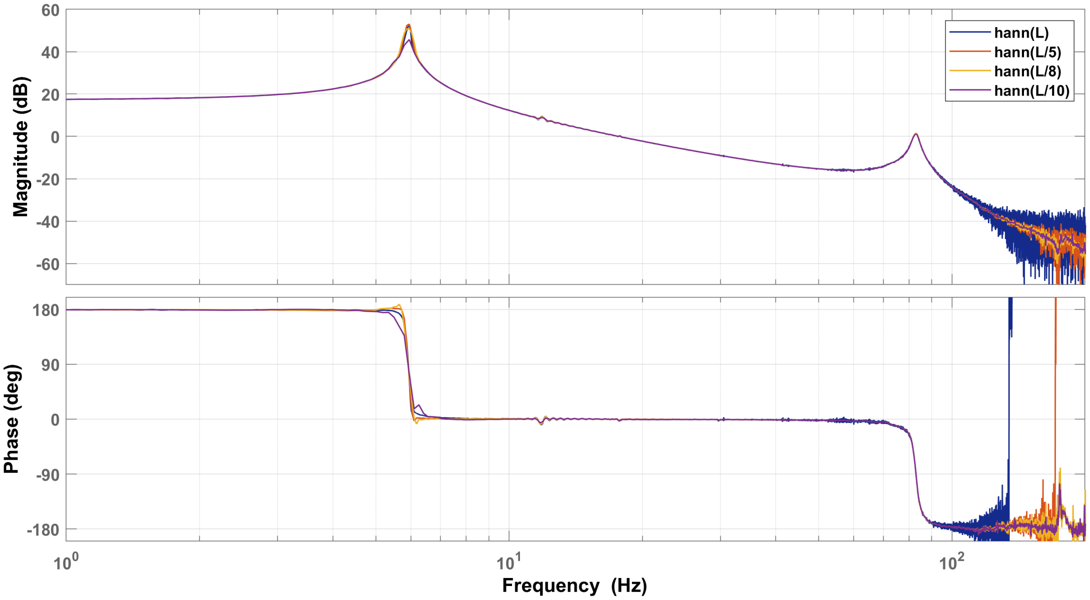

Figure C.6: Illustration of influence of Window Length on Transfer Function Estimate

D | Practical Work

This appendix chapter provides an outline of the practical work involved in constructing the experimental setup. The setup entails the manufacturing of various parts and their subsequent assembly using specific manual processes. The chapter offers instructions and guidance on recreating this setup or constructing setups of a similar nature. It is important to note that these recommendations are based solely on the author's personal experience.

D.1 Flexure incorporating bonded Piezoelectric Transducers

The flexures, with dimensions selected based on system dynamics calculations, are designed in SolidWorks software and manufactured using the Laser-cut manufacturing process. To initiate the manufacturing process, the manufacturing unit must be provided with a DXF file displaying the projected view of the flexures, as illustrated in Fig.D.1. After manufacturing, it is essential to thoroughly clean the flexure pieces using acetone and ethanol.

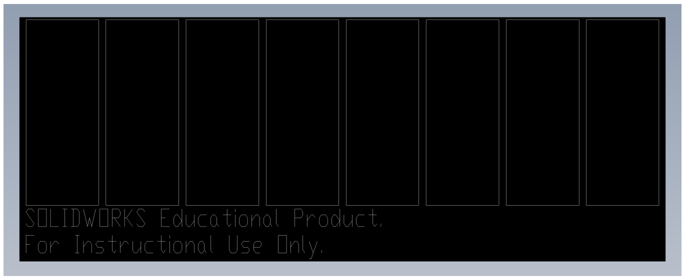

Figure D.1: Sample DXF File for Lasercut Manufacturing of Flexures

To construct the motion system featuring flexures with bonded piezoelectric transducers arranged in a collocated configuration, it is necessary to determine the precise location of these transducers on both sides of each flexure. To achieve this, a mask was designed and printed on a paper sheet to outline the placement of the piezoelectric transducers. While ensuring robustness, a thin mask can be manufactured using 3D Printing. However, this approach presents challenges during the removal process after gluing. Once the paper mask is cut out, it must be accurately positioned on the spring steel flexure using high-quality tape. It is important to note that this is a highly manual process that requires careful execution to achieve nearly perfect placement. The mask includes slots for the piezoelectric placement, with dimensions incorporating a tolerance of up to +0.1 mm to accommodate gluing variations and allow for manual adjustment, considering the specified patch dimension tolerance of ±0.5 mm as per the data sheet. Fig.D.2 illustrates the cut-out mask securely taped onto the flexure.

Figure D.2: Masking on Flexure for Piezoelectric Patch Placement

In order to avoid any interference from the paper during the gluing process, pencil markings are made along the contour of the slots on the flexures. Subsequently, the paper mask is removed. Once this procedure is repeated for all four flexures, the gluing process can commence. For this purpose, the *Double Bubble Loctite* epoxy adhesive is utilized (refer to Fig.D.3). The epoxy consists of two components: Part A, which is the resin, and Part B, the hardener. These components need to be mixed in a 1:1 ratio, resulting in a clear to pale yellow mixture. The epoxy adhesive has a working life of approximately three minutes. Therefore, it is advised to take a small portion of each component at a time and focus on carefully gluing one piezoelectric transducer at a time.

Figure D.3: Loctite Epoxy Set

The mixture of the epoxy adhesive is prepared on a palette using the provided wooden stick that comes with the epoxy pack. Care must be taken to gently and meticulously apply the mixture into the marked slot on the flexure, ensuring that the epoxy remains within the marked contour. Additionally, a layer of epoxy should be applied to the bonding side of the piezoelectric transducer. It is important to ensure that there are no unfilled gaps and that the epoxy layer is uniformly distributed. Once prepared, the piezoelectric transducer should be carefully placed onto the marked slot, preferably utilizing a tool such as tweezers. Any excess epoxy that emerges from the four edges of the patch can be promptly cleaned using a cloth dampened with ethanol.

After properly placing the piezoelectric transducer, a heavy weight should be placed on top of the transducer patch. It is recommended to insert a layer of thick paper towel between the weight and the patch to prevent any potential damage. The weights should be left in place for approximately 20-30 minutes. The epoxy adhesive requires approximately 24 hours to fully cure; therefore, after removing the weights, the flexures with the bonded patches should be left undisturbed for the designated curing time. These steps must be repeated for each patch that needs to be bonded. Fig.D.4 illustrates the final product of the flexures with collocated piezoelectric patches.

Figure D.4: Flexures with bonded Piezoelectric Transducers

D.2 Wiring Connections for Piezoelectric Transducers

In order to connect the piezoelectric transducers to the system, electrical wiring connections are required. For this purpose, reasonably thin electrical wires are used to solder them to the soldering contacts on the patches. From the author's experience, too-thin wires tend to break easily in case of any accidental stretch while handling or assembling the setup, while too-thick wires add significant weight to the setup, affecting the system dynamics. Thus, a balance has to be maintained while selecting the thickness of the wires.

In order to distinguish the wires for the positive and negative terminals of both piezoelectric actuators and sensors, a color scheme is adopted, as shown in Fig.D.5.

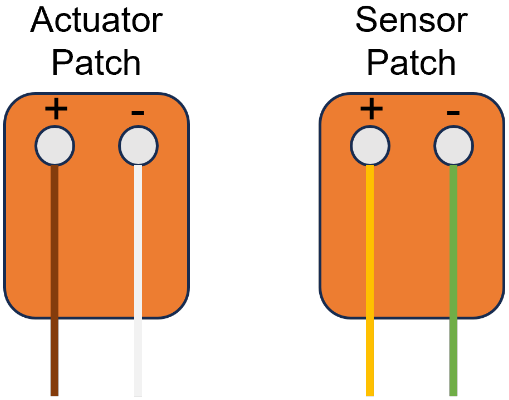

Figure D.5: Color Coding Scheme for Electrical Connections

To establish electrical connections for the piezoelectric transducers, wires of the required length (approximately 45-50 cm) are cut from wire spools available in the laboratory. The ends of the wires are then stripped using a wire stripper tool, removing only a small length necessary for the soldering process. Prior to soldering, it is strongly recommended to clean the contact area using a cloth and acetone to eliminate any unwanted particles and epoxy residue from the gluing process.

Once prepared, the wires are soldered to the soldering contacts on the patches using a soldering iron set at around 350° Celsius, along with tin and flux. It is important to achieve a well-formed dome-shaped solder joint. After soldering all the wires, the soldered contacts should be coated with epoxy to provide electrical insulation. Refer to Fig.D.6 for the desired end product achieved by accurately following these steps.

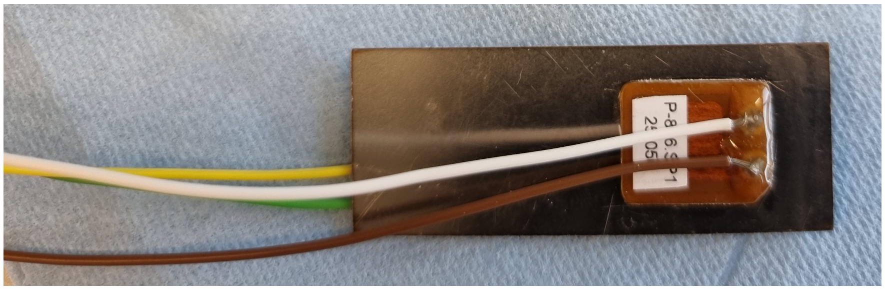

Figure D.6: Piezoelectric Transducers with Soldered Wire Connections